ADDITIVE MANUFACTURING OF FUNCTIONAL CONSTRUCTS UNDER PROCESS UNCERTAINTY

A Dissertation

Presented to the Faculty of the Graduate School

of Cornell University

in Partial Fulfillment of the Requirements for the Degree of

Doctor of Philosophy

by

Daniel Lawrence Cohen

May 2010

ADDITIVE MANUFACTURING OF FUNCTIONAL CONSTRUCTS UNDER

UNCERTAINTY

Daniel Lawrence Cohen, Ph.D.

Cornell University 2010

In recent years, development of novel material-sets has enabled additive

manufacturing (AM) to transform from being used purely for model-making

applications, to production of functional constructs. What was once only a rapid

prototyping technology is now being used to print functional components, including

batteries, actuators, transistors, and for tissue engineering applications, living tissue

(Chapter 1). Associated with these new printing inks, however, is a drastic increase in

the complexity of AM materials, and consequently, in the process uncertainty related

to deposition of these materials. New applications enabled by functional printing

capabilities, in particular *in situ* AM, also have associated process uncertainties,

including situational and environmental uncertainties. That is, uncertainty in the shape

of the substrate and in environmental parameters, such as temperature and humidity.

As additive manufacturing makes the transition from a prototyping technology to more

of a functional-object fabrication platform, these new associated process uncertainties

must be addressed to yield sufficient geometric fidelity. Existing control schemes

largely relied upon open-loop control and did not handle uncertainty through control

algorithms, but instead avoided them by limiting their material-sets, printing on

trivially shaped substrates, and restricting environmental conditions. A few techniques

used geometric feedback to handle materials uncertainty, but these techniques did so

on a process-parameter-level, and did not monitor/manipulate on the whole-part level.

As a result, these techniques could not detect high-level errors such as whole-part deformation. The technique proposed herein, Greedy Geometric Feedback (GGF), closes the loop on the whole-part level and therefore can detect/correct types of errors that were previously un-addressable. Simulations and physical experiments were employed to validate and study the GGF algorithm. Not only was GGF effective at handling materials uncertainties, but it also has potential for situational and environmental uncertainties. Additional work focused on situational uncertainty and alternative control schemes were developed that effectively handled this type of uncertainty with less computational and data collection overhead. A novel difference-based planning approach was employed to explore *in situ* AM repair of osteochondral defects, and repair/adaptation of a four-legged robot. These proof-of-concept prints are the only known examples of generalized *in situ* AM, to date, in which the AM system was not provided *a priori* hard-coded substrate geometric information.

The contributions of the work presented herein fall into three categories: 1) development of functional printing materials, 2) development of novel methodologies for quantitatively optimizing the printing qualities of functional printing inks, and 3) development of novel generalized control schemes for handling AM process uncertainty.

BIOGRAPHICAL SKETCH

Daniel Lawrence Cohen was born in New Brunswick, NJ, on July 1, 1984, to Dorian I. and Gerald R. Cohen. Daniel was raised in East Brunswick, NJ, and attended public schools throughout his early education. As a child, he partook in all the usual Central Jersey rituals, including soccer, music lessons, summer camps, Boy Scouts, and countless trips to the Shore. His parents fostered a love for travel and exploration, and he was fortunate to have been exposed to many interesting sights and diverse cultures at an early age.

In a family with two generations of engineers, Daniel was always drawn toward problem-solving and design. Some of his parents' fondest memories involve Daniel going around the house fixing various objects. Like all young engineers-to-be, he also enjoyed taking things apart to learn how they worked . . . successful reassembly was usually a distant afterthought. He explored his technical interests by participating in various science and engineering summer programs. The summer after ninth grade, Daniel participated in the Brandeis Odyssey Program, where he got his first taste of living away from home and found tremendous inspiration in being surrounded by like-minded kids. He returned to the program the summer after tenth grade and worked in the Brandeis High Energy Physics Laboratory, where he conducted original independent research on quality assurance of muon detector tubes, which are critical components of the Large Hadron Collider at the European Organization for Nuclear Research (CERN). Based on this work, Daniel would later go on to win first place in the Monmouth Junior Science Symposium, which resulted in numerous scholarships. Perhaps the most inspirational summer was after eleventh grade, when Daniel was selected to attend the New Jersey Governor's School of Engineering and Technology. Soon after, he began part-time employment lasting

throughout his senior year of high school as a research assistant at Rutgers, in the same lab he worked in while at Governor's School.

Daniel entered Cornell University in 2002 under the Cornell Presidential Research Scholarship (CPRS) and the McMullen Dean's Scholarship. The CPRS program provided Daniel generous research funding to explore his interests, and encouraged him to get an early start in undergraduate research. Within his first week at Cornell, Daniel began working at the Cornell Computational Synthesis Laboratory (CCSL) under Dr. Hod Lipson, and has remained a member of the lab his entire Cornell career. During the undergraduate portion of his time at CCSL, Daniel conducted research on additive manufacturing deposition tools, printable batteries, and tissue printing. He won the NASA Space Grant Scholarship, as well as the Cornell McManus Design Award. Two-and-a-half years after starting at Cornell, Daniel received his Bachelor of Science degree in Mechanical Engineering and subsequently entered the Ph.D. program at Cornell.

Upon starting the doctoral program, Daniel was awarded both the National Science Foundation Graduate Research Fellowship and the Department of Homeland Security Graduate Fellowship. As part of his obligation to the Department of Homeland Security, Daniel worked at Los Alamos National Laboratory in the summer of 2006. While there, he conducted research and development on laser tracking systems, for which he was awarded a U.S. patent. He was also awarded a patent related to his doctoral work on tissue additive manufacturing, and has several others patents pending.

While Daniel pursued his engineering interests throughout childhood, college, and graduate school, he was also drawn toward business and management. Largely influenced by his father, who was trained as a chemical engineer and who has owned an industrial contracting firm for over 35 years, Daniel always had an appreciation for

business strategy and managerial problem-solving. This interest in management and organizational strategy was one he would pursue in college, as a branding consultant to the University senior administration, and in graduate school as a leader of the Fab@Home Project. Upon graduation, Daniel will enter management consulting, where he will combine his interest in business with his passion for problem-solving, a skill well-honed through his engineering training.

Daniel is an Eagle Scout and has varied interests including hockey, photography, sailing, flying, and music.

To my parents, Dorian Ida and Gerald Robert Cohen.

ACKNOWLEDGMENTS

I would like to extend my deepest gratitude to the following people and to recognize their important contributions to my personal development:

To Hod Lipson, for being a phenomenal academic advisor, a visionary technologist, a compassionate person, and with his sense of humor, a very fun person to be around. He has a tremendous ability to consider all sides of an issue, technology, or problem, and his perspectives are not strictly limited to the technical aspects. He maintains an admirable visionary scope in which he focuses on paradigm shifts. This big-picture, high-impact mentality has kept me engaged as a member of the lab since my first week of freshman year as an undergraduate. As I have grown, his perspective has played a very important part in my development and has fostered my gravitation toward solving problems comprising highly diverse components, both technical and beyond. My nearly decade-long stay in the lab is the truest of testaments to both his exceptional academic and personal qualities.

To Larry Bonassar, for his support and contributions to my development as a scientist and researcher. With his extraordinary teaching abilities, writing talents, and rigorous application of the scientific method, he has taught me a great deal about research. The exposure he has helped me gain in the biomedical realm has complemented my mechanical engineering training and has greatly enriched my academic experience.

To my parents, for their love and support. They have always encouraged me to pursue my interests, entrusted me with the freedom to carve my own unique path, and

given me room to grow. They taught me the importance of making bold choices and being unafraid to be different. They have always been my biggest fans, and their unconditional love has made me what I am.

To my cousin, Michael Eisdorfer, for his friendship, his generous support, and his brilliant ability to make me smile.

I would also like to acknowledge the many friends, and colleagues, who have contributed meaningful ideas or collaborated with me over the years:

Evan Malone, Jeff Lipton, Jeff Ballyns, Viktor Zykov, Mike Tolley, Jon Hiller, Mike Schmidt, Aaron Lenfestey, John Amend, Franz Nigl, Satish Degala, Tunde Babalola, and the Fab@Home Undergraduate Project Team.

To the faculty of Cornell University, especially Professors Anthony Reeves, Ephrahim Garcia, Frank Moon, Ursula Krotscheck, and Meg Thompson.

To the staff of Cornell University, especially Nanette Peterson, Marcia Sawyer, Carol Moss, Kirk Gunsallus, Gabriel Terrizzi, and George Petry.

To the National Science Foundation and the Department of Homeland Security, for supporting me through graduate fellowships during my doctoral studies.

To Suzanne Maher at the Hospital for Special Surgery, for technical assistance during the tissue printing research (Chapter 1).

To the Cornell Center for Material Research (CCMR) for its support of the alginate mixing research (Chapter 2).

To Drs. Meg Thompson and Ursula Krotscheck of the Cornell University College of Veterinary Medicine, for their assistance with CT imaging and tissue defect creation (Chapter 4), respectively.

To the Cornell University School of Hotel Administration for its assistance during the food printing research (Appendix A).

To the entire Fab@Home community and the Cornell Undergraduate Project Team, for their development and support of the printer used throughout many of these experiments.

TABLE OF CONTENTS

LIST OF FIGURES

LIST OF TABLES

INTRODUCTION

The work presented herein advances the field known as additive manufacturing (AM), 3D printing, solid freeform fabrication (SFF), rapid prototyping (RP), or layered manufacturing (LM). The field comprises a group of closely related technologies that use computer-controlled positioning systems to selectively deposit material, resulting in the layer-wise fabrication of 3D objects. While AM's heritage resides primarily in the direct translation of computer automated design (CAD) models into physical engineering prototypes, recent efforts have demonstrated AM's ability to build functional objects, including batteries[1-2], actuators[3], transistors[4], solenoids, and architectural components[5].

However, with new applications of AM toward printing of functional constructs, new advances are necessary in order to address associated challenges. In particular, as AM is used with materials that are relevant for printing functional constructs, these materials tend to have more complex properties than those of traditional modeling materials. Viscoelasticity, property-changing background chemical reactions, and inherently stochastic deposition techniques are just some of the factors that cause functional AM-related *materials uncertainty.* That is, uncertainty in the deposition properties of the printing materials which lead to variation in build-material shape and/or position. The ultimate result of materials uncertainty is geometric error of the resultant construct.

Other types of functional AM-associated uncertainty must be addressed as well. Since the technology will extend beyond model-making, it will likely be applied *in situ*[6-7] to fabrication of constructs on pre-existing parts for the purpose of repair and/or adaptation[8-9]. However, this gives rise to *situational uncertainty* since the substrate geometry is no longer a simple trivial shape. Furthermore, as functional AM

is applied *in situ*, the AM systems will be subject to the environment[8] of the substrate and give rise to *environmental uncertainty.* Once the printer is operating beyond traditional highly controlled environments, even slight fluctuations (temperature, humidity, vibration, etc.) can have severe adverse effects on the geometric fidelity of the printed constructs.

The work presented in this dissertation falls into three categories: 1) development of functional printing materials, 2) development of novel methodologies for quantitatively optimizing the printing qualities of functional printing inks, and 3) development of novel generalized control schemes for handling AM process uncertainty.

The first portion of work presented herein addresses the creation of a novel tissue engineering AM printing ink–pre-calcium-initiated alginate hydrogel. The material platform not only serves as an example of functional printing, which motivates the subsequent work on handling AM uncertainty, but the alginate printing ink also addresses critical challenges facing the field of tissue engineering. While tissue engineering principles had been successfully applied to creation of both living cartilage[10-17] and bone[18-19], fabricating constructs in complex shapes remained highly challenging. Several techniques for achieving geometric complexity have been developed, including: layering of cells[20], layering of cell-seeded hydrogels[21-22], casting of seeded hydrogels onto complex surfaces[23], seeding of molded porous scaffolds[24], and injection molding of seeded hydrogels[25]. These techniques, however, did not enable fabrication of constructs with multi-axial spatial heterogeneities, including different cell types or densities. Furthermore, these techniques required custom tooling and achieving patient-specific shapes was often prohibitively challenging. One approach that overcomes these limitations is additive manufacturing (AM) of cell-seeded hydrogels. A number of techniques have recently emerged, such as AM of

photocrosslinkable hydrogels (PEG[26-28]), thermoreversible gels (gelatin[29-34], pluronic[35], collagen[30,35-36]), and post-deposition ionically crosslinked alginate hydrogel[33-34,37]. Many of these techniques however, were incapable of producing constructs with multi-axial spatial heterogeneities; none of them enabled printing without substantial post-deposition environmental constraints. That latter concern is especially important for potential future application of the technology *in situ*, such as in conjunction with minimally invasive surgical procedures. The technique proposed herein, pre-initiated calcium-crosslinked alginate hydrogel, was the only tissue engineering technique that was both capable of producing mutli-axially spatially heterogeneous constructs as well as not imposing post-deposition constraints in order to initiate material phase change. Experiments were conducted to find an optimal formulation that enabled deposition tool extrusion while retaining construct-shape (Chapter 1). Further investigations were conducted to validate that the technique produced constructs which were sterile, cell-viable, biologically functioning (in terms of extracellular matrix production), and mechanically intact (Chapter 1).

The next portion of work presented herein addressed methodologies for quantitatively optimizing ink formulation with respect to material homogeneity, as well as applying this technique to the study of alginate hydrogel. While the alginate AM technique was shown to possess favorable printing and biological qualities, anecdotal evidence suggested that the mixing technique used to combine the alginate and calcium crosslinking solutions had a critical effect on the homogeneity of the printing ink, and consequently, on the geometric fidelity and reliability of printed constructs. While some studies addressed the effects of AM machine printing parameters on ink quality, in particular tip diameter and pumping pressure on cell viability[38-39], no studies assessed the effects of material formulation on bio-ink efficacy and mixing technique was not addressed at all. Even in the broader tissue

engineering context, injection molding techniques involving alginate hydrogel did not analyze the effects of mixing[25,40-45], likely due to the lack of methodologies for quantitatively characterizing gel homogeneity. By developing novel experimental methodologies based on real-time measurement of gel-extrusion force, homogeneity was characterized as a function of mixing amount (Chapter 2). The investigation discovered significant improvements in homogeneity and printed construct geometric fidelity in mixing regimes far outside those suggested in prior literature[25,40-45]. The investigation discovered improvements in cell viability and mechanical integrity as mixing was increased (Chapter 2). This work provided new insights into the alginate hydrogel material platform and had additional implications for other non-AM techniques that use the material[25,40-49]. Furthermore, this work established new methodologies which could be generalized to other printing inks in order to characterize ink-homogeneity, which is one of the most important factors related to achieving high geometric fidelity of printed constructs.

The complexities associated with functional materials (Chapters 1, Chapter 2, Appendix A) motivated the need for a more generalized approach to handling materials uncertainty. Not only do functional printing materials possess properties that may prohibit effective open-loop tuning, but even if such tuning were conceivably attainable, the effort to do so may make it unfeasible. In addition to handling materials uncertainties, this novel control scheme also needed to handle situational and environmental uncertainties associated with functional *in situ* AM. One approach to handling a wide range of uncertainties was feedback control.

Low-level-parameter closed-loop feedback control schemes have been implemented in SFF systems to improve the geometric fidelities of printed parts. These techniques, however, mostly monitored and stabilized low-level non-geometric process parameters, such as machine temperature, material federate, melt-pool depth[50],

4

and tool position[51]. Several techniques monitored low-level geometric parameters in an attempt to improve print quality, including monitoring bead height to determine laser power[52], as well as modeling droplet geometry to determine feed-rates[53-54] and jetting pressures[55]. However, these control schemes were still low-level approaches because whole-part geometry was not directly monitored/manipulated; there was only an indirect relationship between the droplet shape and final overall shape of the part. Since none of these aforementioned closed-loop feedback schemes "closed the loop" at the level of whole-part geometry, none of them could account for errors that occurred at a higher level than the process-variable level. Even monitoring the shapes of individual droplets leaves room for higher level errors (i.e., errors occurring in the whole-part geometry) to be undetectable. Furthermore, none of the prior control techniques directly manipulated the shape of the overall geometry and consequently they had potentially limited ability to correct for errors that occurred on the whole-part geometry level (such as during-print whole-part deformation, as well as uneven substrates).

Herein, a novel technique called Greedy Geometric Feedback (GGF) was proposed in which the whole-part geometry was monitored in order to determine locations of subsequent droplets (Chapter 3). Since GGF closed the loop on the whole-part level, it was able to detect and correct types of errors that were previously un-addressable by prior control techniques. Simulations were performed and physical experiments conducted in order to validate and study the characteristics of GGF (Chapter 3).

While GGF was a generalized technique that could address wide ranges of types of AM process uncertainties, during subsequent proof-of-concept experiments, situational uncertainty was focused on in particular due to its relevance for enabling *in*

situ AM which is an important application of functional AM. When solely addressing situational uncertainty, new techniques were explored that were less computationally/feedback expensive. Rather than real-time closed-loop geometric feedback (e.g. GGF), other techniques were investigated for handling situational uncertainty with static-shaped substrates. Difference based planning methods were devised and other *in situ*-specific issues were addressed, including material selection, geometric data capture, image processing, registration, and geometric benchmarking (Chapters 4 & 5). Very few methodologies existed for quantifying geometric fidelity of printed constructs[40], and thus new techniques had to be created to meaningfully characterize the geometric fidelity of the *in situ* prints (Chapters 4 & 5). The first proof-of-concept experiment demonstrated *in situ* repair of chondral and osteochondral defects on a calf femur with alginate hydrogel and a novel formulation of Demineralized Bone Matrix (DBM). The geometric fidelity was compared to clinical benchmarks[56-61] for shape error and found to be mostly within clinical standards. The second proof-of-concept experiment demonstrated *in situ* repair and adaptation of a four-legged robot. The robot leg was critically damaged, and subsequently repaired to restore function. Also, two of the legs were morphologically adapted to yield new capability. Not only do these *in situ* techniques and demonstrations have implications for biomedical applications, but they also have the potential to bridge computational autonomous design techniques with the physical world[62-63].

Prior to this work, there were only a few examples of *in situ* AM[6-7], however, even in these cases, the substrate geometry was hard-coded into the system *a priori*. The proof-of-concept prints herein use novel techniques to overcome challenges related to situational uncertainty, and thus are the first examples of generalized *in situ*

AM in which the system was not provided hard-coded *a priori* knowledge of the substrate geometry.

Through novel materials developed to enable functional AM, new methodologies for quantitatively optimizing key parameters such as homogeneity, and novel control/AM-planning techniques for handling process uncertainties, AM has the potential to greatly expand into new territories. As functional printing becomes more prevalent and *in situ* applications are further explored, AM will likely extend well beyond its model-making heritage and become an important fabrication technology for low-volume, highly customized production of functional objects, as well as for autonomous repair and adaptation of complex systems.

REFERENCES

[1]   E. Malone, K. Rasa, D. L. Cohen, T. Issacson, H. Lashley, and H. Lipson, "Freeform fabrication of 3D zinc-air batteries and functional electromechanical assemblies," in *Fourteenth Solid Freeform Fabrication Symposium*, Austin, Texas, 2003, pp. 363-374.

[2]   E. Malone, K. Rasa, D. L. Cohen, T. Issacson, H. Lashley, and H. Lipson, "Freeform fabrication of zinc-air batteries and electromechanical assemblies," *Rapid Prototyping Journal,* vol. 10, pp. 58-69, 2004.

[3]   E. Malone and H. Lipson, "Freeform fabrication of ionomeric polymer-metal composite actuators," *Rapid Prototyping Journal,* vol. 12, pp. 244-253, 2006.

[4]   R. Havener, J. Boyea, E. Malone, D. Bernards, J. DeFranco, G. Malliaras, and H. Lipson, "Freeform fabrication of organic electromechanical transistors," in *Eighteenth Solid Freeform Fabrication Symposium*, Austin, Texas, 2007, pp. 60-73.

[5]   J. I. Lipton, D. L. Cohen, and H. Lipson, "Brick printing: Freeform fabrication of modular architectural elements with embedded systems," in *Twentieth Annual International Solid Freeform Fabrication Symposium*, Austin, Texas, 2009, pp. 711-723.

[6]   S. Sampath, "Novel concepts in direct writing of electronics and sensors," *IEEE Sensors Journal,* vol. 4, 2004.

[7]   L. Sun, K. J. Jakubenas, J. E. Crocker, S. Harrison, L. L. Shaw, and H. L. Marcus, "In situ thermocouples in macro-components fabricated using SALD and SALDVI techniques," *Materials and Manufacturing Processes,* vol. 13, pp. 909-919, 1998.

[8]   M. P. Bodiford, S. D. Gilley, R. W. Howard, J. P. Kennedy, and J. A. Ray, "Are we there yet?… developing in situ fabrication and repair (ISFR) technologies to explore and live on the Moon and Mars," in *First Space Exploration Conference: Continuing the Voyage of Discovery*, Orlando, Florida, 2005, pp. 1-7.

[9]   F. Pérès and D. Noyes, "Envisioning e-logistics developments: Making spare parts in situ and on demand state-of-the-art and guidelines for future developments," *Computers in Industry,* vol. 57, pp. 490-503, 2006.

[10]   Y. Cao, J. P. Vacanti, K. T. Paige, J. Upton, and C. A. Vacanti, "Transplantation of chondrocytes utilizing a polymer-cell construct to produce tissue-engineered cartilage in the shape of a human ear," *Plastic and Reconstructive Surgery,* vol. 100, p. 297, 1997.

[11]   C. Ibarra, C. Jannetta, C. A. Vacanti, Y. Cao, T. H. Kim, J. Upton, and J. P. Vacanti, "Tissue engineered meniscus: a potential new alternative to allogeneic meniscus transplantation," *Transplantation Proceedings,* vol. 29, pp. 986-988, 1997.

[12]   S. H. Kamil, K. Kojima, M. P. Vacanti, L. J. Bonassar, C. A. Vacanti, and R. D. Eavey, "In vitro tissue engineering to generate a human-sized auricle and nasal tip," *Laryngoscope,* vol. 113, p. 90, 2003.

[13]   W. S. Kim, J. P. Vacanti, L. Cima, D. Mooney, J. Upton, W. C. Puelacher, and C. A. Vacanti, "Cartilage engineered in predetermined shapes employing cell transplantation on synthetic biodegradable polymers," *Plastic and Reconstructive Surgery,* vol. 94, p. 233, 1994.

[14]   K. Kojima, L. J. Bonassar, R. A. Ignotz, K. Syed, J. Cortiella, and C. A. Vacanti, "Comparison of tracheal and nasal chondrocytes for tissue engineering of the trachea," *The Annals of Thoracic Surgery,* vol. 76, p. 1884, 2003.

[15]   H. Mizuno, A. K. Roy, C. A. Vacanti, K. Kojima, M. Ueda, and L. J. Bonassar, "Tissue-engineered composites of anulus fibrosus and nucleus pulposus for intervertebral disc replacement," *Spine,* vol. 29, p. 1290, 2004.

[16]   W. C. Puelacher, D. Mooney, R. Langer, J. Upton, J. P. Vacanti, and C. A. Vacanti, "Design of nasoseptal cartilage replacements synthesized from biodegradable polymers and chondrocytes," *Biomaterials,* vol. 15, p. 774, 1994.

[17]   W. C. Puelacher, J. Wisser, C. A. Vacanti, N. F. Ferraro, D. Jaramillo, and J. P. Vacanti, "Temporomandibular joint disc replacement made by tissue-engineered growth of cartilage," *Journal of Oral and Maxillofacial Surgery,* vol. 52, pp. 1172-1177, 1994.

[18]   W. C. Puelacher, J. P. Vacanti, N. F. Ferraro, B. Schloo, and C. A. Vacanti, "Femoral shaft reconstruction using tissue-engineered growth of bone," *International Journal of Oral & Maxillofacial Surgery,* vol. 25, pp. 223-228, 1996.

[19]   Y. Weng, Y. Cao, C. Arevalo, M. P. Vacanti, and C. A. Vacanti, "Tissue-engineered composites of bone and cartilage for mandible condylar reconstruction," *Journal of Oral and Maxillofacial Surgery,* vol. 59, pp. 185-190, 2001.

[20]   T. J. Klein, B. L. Schumacher, T. A. Schmidt, K. W. Li, M. S. Voegtline, K. Masuda, E. Thonar, and R. L. Sah, "Tissue engineering of stratified articular cartilage from chondrocyte subpopulations," *Osteoarthritis and Cartilage,* vol. 11, pp. 595-602, 2003.

[21]   T. K. Kim, B. Sharma, C. G. Williams, M. A. Ruffner, A. Malik, E. G. McFarland, and J. H. Elisseeff, "Experimental model for cartilage tissue engineering to regenerate the zonal organization of articular cartilage," *Osteoarthritis and Cartilage,* vol. 11, pp. 653-664, 2003.

[22]   K. W. Ng, C. C. B. Wang, R. L. Mauck, T. A. N. Kelly, N. O. Chahine, K. D. Costa, G. A. Ateshian, and C. T. Hung, "A layered agarose approach to fabricate depth-dependent inhomogeneity in chondrocyte-seeded constructs," *Journal of Orthopaedic Research,* vol. 23, pp. 134-141, 2005.

[23]   C. T. Hung, E. G. Lima, R. L. Mauck, E. Taki, M. A. LeRoux, H. H. Lu, R. G. Stark, X. E. Guo, and G. A. Ateshian, "Anatomically shaped osteochondral constructs for articular cartilage repair," *Journal of Biomechanics,* vol. 36, pp. 1853-1864, 2003.

[24]   Y. Cao, A. Rodriguez, M. Vacanti, C. Ibarra, C. Arevalo, and C. A. Vacanti, "Comparative study of the use of poly (glycolic acid), calcium alginate and pluronics in the engineering of autologous porcine cartilage," *Journal of Biomaterials Science, Polymer Edition,* vol. 9, pp. 475-487, 1998.

[25]   S. C. Chang, J. A. Rowley, G. Tobias, N. G. Genes, A. K. Roy, D. J. Mooney, C. A. Vacanti, and L. J. Bonassar, "Injection molding of chondrocyte/alginate constructs in the shape of facial implants," *Journal of Biomedical Materials Research,* vol. 55, pp. 503-511, 2001.

[26]   D. R. Albrecht, V. L. Tsang, R. L. Sah, and S. N. Bhatia, "Photo- and electropatterning of hydrogel-encapsulated living cell arrays," *Lab On a Chip,* vol. 5, pp. 111-118, 2004.

[27]   Y. Lu, G. Mapili, G. Suhali, S. Chen, and K. Roy, "A digital micro-mirror device-based system for the microfabrication of complex, spatially patterned tissue engineering scaffolds.," *Journal of Biomedical Materials Research Part A,* vol. 77, pp. 396-405, 2006.

[28]   V. L. Tsang and S. N. Bhatia, "Three-dimensional tissue fabrication," *Advanced Drug Delivery Reviews,* vol. 56, pp. 1635-1647, 2004.

[29]   R. Landers, U. Hübner, R. Schmelzeisen, and R. Mülhaupt, "Rapid prototyping of scaffolds derived from thermoreversible hydrogels and tailored for applications in tissue engineering," *Biomaterials,* vol. 23, pp. 4437-4447, 2002.

[30]   R. Landers, A. Pfister, U. Hübner, H. John, R. Schmelzeisen, and R. Mülhaupt, "Fabrication of soft tissue engineering scaffolds by means of rapid prototyping techniques," *Journal of Materials Science,* vol. 37, pp. 3107-3116, 2002.

[31] X. Wang, Y. Yan, Y. Pan, Z. Xiong, H. Liu, J. Cheng, L. Feng, L. Feng, R. Wu, R. Zhang, and Q. Lu, "Generation of three-dimensional hepatocyte/gelatin structures with rapid prototyping system," *Tissue Engineering,* vol. 12, pp. 83-90, 2006.

[32] X. Wei, W. Xiaohong, Y. Yongnian, Z. Wei, X. Zhuo, L. Feng, W. Rendong, and Z. Renji, "Rapid prototyping three-dimensional cell/gelatin/fibrinogen constructs for medical regeneration," *Journal of Bioactive and Compatible Polymers,* vol. 22, pp. 363-377, July 1, 2007 2007.

[33] Y. Yan, X. Wang, Y. Pan, H. Liu, J. Cheng, Z. Xiong, F. Lin, R. Wu, R. Zhang, and Q. Lu, "Fabrication of viable tissue-engineered constructs with 3D cell-assembly technique," *Biomaterials,* vol. 26, pp. 5864-5871, 2005.

[34] Y. Yan, X. Wang, Z. Xiong, H. Liu, F. Liu, F. Lin, R. Wu, R. Zhang, and Q. Lu, "Direct construction of a three-dimensional structure with cells and hydrogel," *Journal of Bioactive and Compatible Polymers,* vol. 20, pp. 259-269, 2005.

[35] C. M. Smith, A. L. Stone, R. L. Parkhill, R. L. Stewart, M. W. Simpkins, A. M. Kachurin, W. L. Warren, and S. K. Williams, "Three-dimensional BioAssembly tool for generating viable tissue-engineered constructs," *Tissue Engineering,* vol. 10, pp. 1566-1576, 2004.

[36] V. Mironov, T. Boland, T. Trusk, G. Forgacs, and R. R. Markwald, "Organ printing: computer-aided jet-based 3D tissue engineering," *Trends in Biotechnology,* vol. 21, pp. 157-161, 2003.

[37] S. Khalil and W. Sun, "Bioprinting endothelial cells with alginate for 3D tissue constructs," *Journal of Biomechanical Engineering,* vol. 131, pp. 1002-1008, 2009.

[38] R. Chang, J. Nam, and W. Sun, "Effects of dispensing pressure and nozzle diameter on cell survival from solid freeform fabrication-based direct cell writing," *Tissue Engineering Part A,* vol. 14, pp. 41-48, 2008.

[39] K. Nair, K. Yan, and W. Sun, "A computational modeling approach for the characterization of mechanical properties of 3D alginate tissue scaffolds," *Journal of Applied Biomaterials and Biomechanics,* vol. 6, pp. 35-46, 2008.

[40] J. J. Ballyns, D. L. Cohen, E. Malone, S. A. Maher, H. G. Potter, T. M. Wright, H. Lipson, and L. J. Bonassar, "An optical method for evaluation of geometric fidelity for anatomically shaped tissue engineered constructs," *Tissue Engineering Part C: Methods,* accepted.

[41] J. J. Ballyns, J. P. Gleghorn, V. Niebrzydowski, J. J. Rawlinson, H. G. Potter, S. A. Maher, T. M. Wright, and L. J. Bonassar, "Image-guided tissue

engineering of anatomically shaped implants via MRI and Micro-CT using injection molding," *Tissue Engineering Part A,* vol. 14, pp. 1195-1202, 2008.

[42] S. C. Chang, G. Tobias, A. K. Roy, C. A. Vacanti, and L. J. Bonassar, "Tissue engineering of autologous cartilage for craniofacial reconstruction by injection molding," *Plastic and Reconstructive Surgery,* vol. 112, pp. 793-799, 2003.

[43] M. E. Hott, C. A. Megerian, R. Beane, and L. J. Bonassar, "Fabrication of tissue engineered tympanic membrane patches using computer-aided design and injection molding," *The Laryngoscope,* vol. 114, pp. 1290-1295, 2004.

[44] C. K. Kuo and P. X. Ma, "Maintaining dimensions and mechanical properties of ionically crosslinked alginate hydrogel scaffolds in vitro," *Journal of Biomedical Materials Research Part A,* vol. 84, pp. 899-907, 2008.

[45] J.-W. Xu, V. Zaporojan, G. M. Peretti, R. E. Roses, K. R. Morse, A. K. Roy, J. M. Mesa, M. A. Randolph, L. J. Bonassar, and M. J. Yaremchuk, "Injectable tissue-engineered cartilage with different chondrocyte sources," *Plastic and Reconstructive Surgery,* vol. 113, pp. 1361-1371, 2004.

[46] B. Beekman, N. Verzijl, R. A. Bank, K. v. d. Mark, and J. M. TeKoppele, "Synthesis of collagen by bovine chondrocytes cultured in alginate: posttranslational modifications and cell-matrix interaction," *Experimental Cell Research,* vol. 237, pp. 135-141, 1997.

[47] B. O. Enobakhare, D. L. Bader, and D. A. Lee, "Quantification of sulfated glycosaminoglycans in chondrocyte/alginate cultures, by use of 1,9-dimethylmethylene blue," *Analytical Biochemistry,* vol. 243, pp. 189-191, 1996.

[48] K. T. Paige, L. G. Cima, M. J. Yaremchuk, B. L. Schloo, J. P. Vacanti, and C. A. Vacanti, "De novo cartilage generation using calcium alginate-chondrocyte constructs," *Plastic and Reconstructive Surgery,* vol. 97, pp. 168-180, 1996.

[49] K. T. Paige, L. G. Cima, M. J. Yaremchuk, J. P. Vacanti, and C. A. Vacanti, "Injectable cartilage," *Plastic and Reconstructive Surgery,* vol. 96, pp. 1390-1400, 1995.

[50] H. Derouet, L. Sabatier, F. Coste, and R. Fabbro, "Process control applied to laser surface remelting," in *ICALEO'97*, 1997, pp. 71-77.

[51] D. Hu, H. Mei, and R. Kovacevic, "Improving solid freeform fabrication by laser-based additive manufacturing," *Proceedings of The Institution of Mechanical Engineers Part B: Journal of Engineering Manufacture,* vol. 216, pp. 1253-1264, 2002.

[52]   J. Mazumder, A. Schifferer, and J. Choi, "Direct materials deposition: designed macro and microstructure," *Materials Research Innovations,* vol. 3, pp. 118-131, 1999.

[53]   C. Doumanidis and E. Skordeli, "Distributed-parameter modeling for geometry control of manufacturing processes with material deposition," *Journal of Dynamic Systems, Measurement, and Control,* vol. 122, pp. 71-77, 2000.

[54]   C. Doumanidis and Y.-M. Kwak, "Geometry modeling and control by infrared and laser sensing in thermal manufacturing with material deposition," *Journal of Manufacturing Science and Engineering,* vol. 123, pp. 45-52, 2001.

[55]   M. J. Lovelady and J. D. Watts, "Closed loop feedback for continuous mode materials jetting," in *IEEE/CPMT International Electronic Manufacturing Technology Symposium*, Austin, Texas, 1999, pp. 189-195.

[56]   G. Bentley, L. C. Biant, W. J. Carrington, M. Akmal, A. Goldberg, A. M. Williams, J. A. Skinner, and J. Pringle, "A prospective, randomised comparison of autologous chondrocyte implantation versus mosaicplasty for osteochondral defects in the knee," *Journal of Bone and Joint Surgery,* vol. 85, pp. 223-230, 2003.

[57]   W. D. Bugbee and F. R. Convery, "Osteochondral allograft transplantation," *Complex Topics in Knee Surgery,* vol. 18, pp. 67-75, 1999.

[58]   M. Dienst, P. E. Greis, B. J. Ellis, K. N. Bachus, and R. T. Burks, "Effect of lateral meniscal allograft sizing on contact mechanics of the laterial tibial plateau: An experimental study in human cadaveric knee joints," *American Journal of Sports Medicine,* vol. 35, pp. 34-42, 2007.

[59]   S. J. Hospodar and J. M. Tokish, "Management of articular cartilage injuries in the knee," *Operative Techniques in Sports Medicine,* vol. 13, pp. 150-156, 2005.

[60]   R. E. Meehan and M. E. Brage, "Fresh osteochondral allografting for osteochondral defects of the talus: a case review," *Techniques in Foot & Ankle Surgery,* vol. 3, pp. 53-61, 2004.

[61]   M. E. Easley and P. E. Scranton, "Osteochondral autologous transfer system," *Foot and Ankle Clinics,* vol. 8, pp. 275-290, 2003.

[62]   P. Funes and J. Pollack, "Evolutionary body building: Adaptive physical designs for robots," *Artificial Life,* vol. 4, pp. 337-357, 1998.

[63]   H. Lipson and J. Pollack, "Automatic design and manufacture of robotic lifeforms," *Nature,* vol. 406, pp. 974-978, 2000.

CHAPTER 1: DIRECT FREEFORM FABRICATION OF SEEDED HYDROGELS IN ARBITRARY GEOMETRIES[*]

ABSTRACT

A major challenge in tissue engineering is the generation of cell-seeded implants with structures that mimic native tissue, both in anatomic geometries and intratissue cell distributions. By combining the strengths of injection molding tissue engineering with those of Solid Freeform Fabrication (SFF), three-dimensional pre-seeded implants were fabricated without custom-tooling, enabling efficient production of patient-specific implants. The incorporation of SFF technology also enabled the fabrication of geometrically complex, multiple-material implants with spatially heterogeneous properties that would otherwise be challenging to produce. Utilizing a custom-built robotic SFF platform and gel deposition tools, alginate hydrogel was used with calcium sulfate as a crosslinking agent to produce pre-seeded living implants of arbitrary geometries. The process was determined to be sterile and viable at 94±5%. The GAG and hydroxyproline production was found to be similar to that of other implants fabricated using the same materials with different shaping methods. The geometric fidelity of the process was quantified by using the printing platform as a Computerized Measurement Machine (CMM); the RMS surface roughness of printed samples in the z-dimension was found to be 0.16±0.02 mm.

INTRODUCTION

A major challenge in tissue engineering is the generation of cell-seeded implants with structures that mimic native tissue, both in anatomic geometries and

[*] Daniel L. Cohen[1], Evan Malone[1,2], Hod Lipson[1,2], Lawrence J. Bonassar[1,3]; [1]Cornell University, Mechanical and Aerospace Engineering, Ithaca NY; [2]Cornell University, Computing and Information Science, Ithaca NY; [3]Cornell University, Biomedical Engineering, Ithaca NY.

intratissue cell distributions. Indeed, the therapeutic promise of tissue engineering was most famously demonstrated in pioneering work by Charles Vacanti and colleagues in which tissue engineered cartilage was shaped into the form of human ear[1]. In additional work, this idea was extended to demonstrate the generation of cartilage of arbitrary shapes[2], as well as many specific anatomic geometries including temporomandibular disc[3] and joint[4], meniscus[5], trachea[6], intervertebral disc[7], nasal tip[8] and nasal septum[9]. These principles apply to other tissues as well, particularly bone, where the reproduction of anatomically shaped tissue has been demonstrated in the generation of femoral shaft[10] and mandibular condyle[4] in rats and culminating in the generation of a distal phalanx in a human patient[11].

Previous studies demonstrating the engineering of tissues in complex geometries used a variety of techniques to achieve control of shape. Tissues with complex two-dimensional surface-geometries have been generated by casting cell-seeded hydrogel onto substrate base-layers with desired surface-shapes[12]. Three-dimensional tissues with complex geometries have been fabricated through seeding of cells onto molded scaffolds[13] or injection-molding of cell-seeded hydrogels[14]. While these techniques were able to create constructs with complex shapes, they lacked the ability to easily create parts with spatial heterogeneities.

Other studies have investigated methods to reproduce zonal spatial variations in articular cartilage constructs. These approaches created spatially heterogeneous constructs by depositing multiple layers of chondrocytes[15] or chondrocyte-seeded hydrogels[16,17]. While these techniques produced zonal organization in engineered tissues, they were limited to spatially varying the construct-properties only along a single axis. Furthermore, while these techniques were feasible in the case of in vitro construct fabrication, it is not inherently feasible to adapt them for in vivo, or in situ, fabrication. For example, it would be challenging to place pre-formed hydrogel sheets

through a small orifice while achieving proper alignment and bonding, such as would be necessary for incorporation into a minimally invasive implantation scheme.

Solid Freeform Fabrication (SFF) technology has been used both to aid in the fabrication of tissues with complex geometries as well to enable the production of constructs with spatial variations along multiple axes. SFF, often referred to as rapid prototyping, is analogous to three-dimensional printing. In SFF, layers of material are deposited or fused subsequently until a complete freeform geometry has been built.

SFF schemes have been used to engineer tissues with complex geometries by using rapid prototyping techniques and Computer-Aided Manufacturing (CAM) to fabricate traditional porous scaffolds which are subsequently seeded with cells[18]. This approach was capable of creating scaffolds of high geometric complexity, however, problems inherent with traditional scaffolding techniques persisted, such as seeding-depth limitations. A second SFF-assisted approach to creating geometrically complex implants overcame seeding-depth limitations by rapid prototyping molds and injecting pre-seeded-hydrogel[19]. A third SFF-based technique created pre-seeded geometrically complex implants without the need for a mold by photo-crosslinking PEO and PEGM layer-by-layer[20]. However, none of these three SFF-based techniques enabled the fabrication of implants with complex zonal variations in three-dimensions (i.e., three-dimensional spatial variation in cell-type, cell density, etc.). Furthermore, these techniques are not ideal for minimally invasive implantation schemes. The SFF of traditional porous scaffolds[18] and molds[19] relied upon in vitro fabrication of the implants, and likely require invasive surgery in order to implant a full-sized construct. The photo-crosslinking technique[20] is not completely suitable for in situ fabrication because it imposes major constraints upon the environment in which constructs may be fabricated. For example, in the case of in vivo fabrication, it may not be feasible to separate the tissue of the patient widely and steadily enough for a pool of polymer to

be maintained in a stable fashion. Also, it may be difficult to fit a light source into the fabrication cavity at an orientation that is nearly perpendicular to the direction of the filling of the polymer well. Additionally, orientation of the layers is important with SFF, due to the orientation's impact on mechanical properties; however, the photo-crosslinking technique is restricted to creating layer-orientation in a direction perpendicular to gravity because the orientation of the surface of the liquid polymer pool is governed by gravitational force. The disadvantageous constraints imposed upon the printing environment by the polymer pool are also shared by techniques which deposit hydrogel into baths of crosslinker[21].

More recently, studies have investigated approaches using SFF technology that were capable of producing cell-constructs with both geometric complexity and multi-axial zonal organization. Collagen I and Pluronic F-127 were recently used in an SFF process to produce viable cell-gel constructs with complex geometries layer-by-layer[22]. While the technology was also capable of fabricating components with complex zonal organization[22], constructs created with PF-127 and Collagen I are generally not three-dimensionally stable in culture. Furthermore, since the gelation was not initiated prior to the deposition of the material, but rather by means of heat flow, strict thermal constraints were placed upon the fabrication environment which may adversely affect certain in situ or in vivo fabrication approaches.

Thus, there exist no SFF processes to create pre-seeded, arbitrarily shaped, spatially heterogeneous constructs that are three-dimensionally stable in culture and minimally impose constraints upon the printing environment.

The approach presented herein directly used a gantry robot to deposit pre-seeded alginate hydrogel layer-by-layer. This technology was capable of producing implants with both complex geometry and zonal organization that were three-dimensionally stable in culture. Since the gel was pre-seeded and crosslinking was

17

initiated prior to deposition, this technique relaxed the constraints imposed upon the printing environment because, unlike other techniques, it neither required seeding of the construct after deposition nor required energy addition to the material during deposition, such as specific light or temperature conditions. The only energy needed during deposition was that required to extrude the gel; this power source can easily be located externally to the printing environment without interfering with the in situ printing objective, unlike light and thermal energy sources. Alginate serves as a favorable cell delivery material since it is: 1) three-dimensionally stable in culture; 2) non-toxic; 3) extrusion-compatible; 4) pre-seeding-compatible; and, 5) its crosslinking can be initiated prior to deposition.

The objectives of this study were to: 1) develop a process to print pre-cell-seeded alginate gels in arbitrary shapes; 2) document the sterility and viability of the process; 3) determine the mechanical properties and extracellular matrix production characteristics of printed samples; and, 4) characterize the geometric fidelity of the printing technique.

MATERIALS AND METHODS

Robotic Platform

The Solid Freeform Fabrication robotic platform was an open-architecture CAM system that consisted of a gantry robot and a set of interchangeable deposition tools[23] (Figure 1.1). The deposition tools were attached to the X-Y axes of the gantry robot and the hydrogel was deposited onto the Z-stage, which served as the build surface.

The gantry robot had a workspace of 30 cm × 30 cm × 30 cm and was capable of carrying a deposition tool of up to 5 kg. The X-Y axes of the gantry had a maximum traverse speed of 0.05 m/s and a maximum acceleration of 2.1 g. High

traverse acceleration was important in order to maintain constant velocity around corners with small radii of curvature. The gantry robot could position the tip of the deposition tool with 25 µm precision.
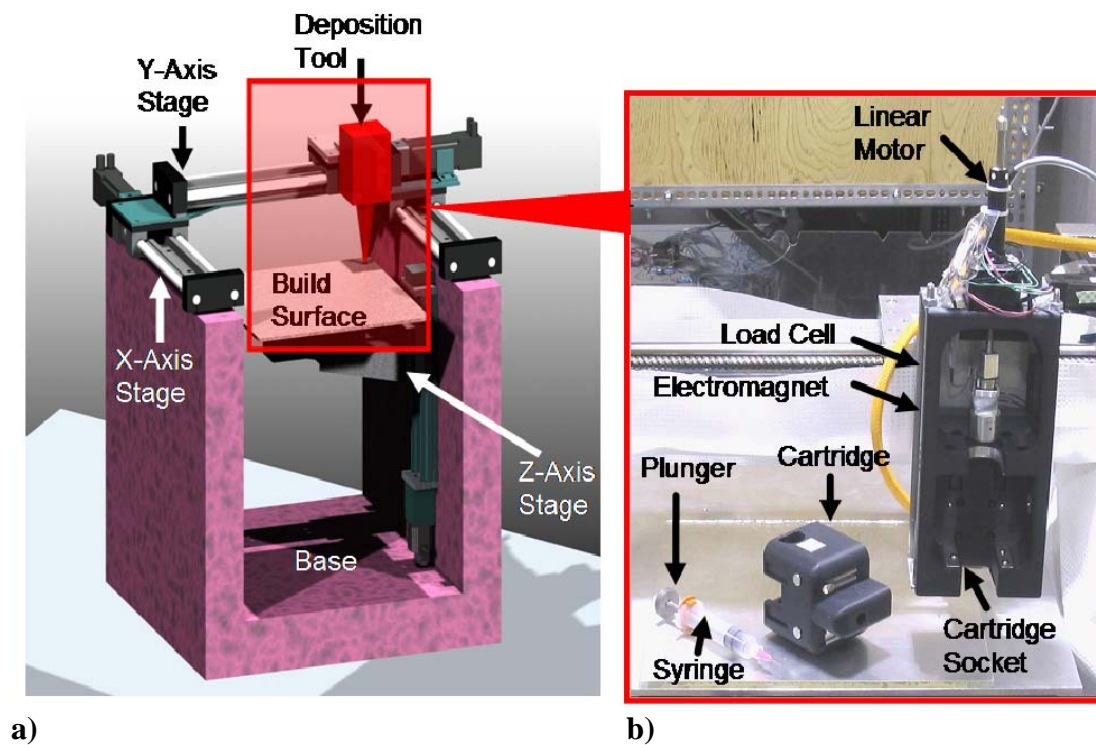
Figure 1.1. Robotic printing platform. (a) CAD rendering of gantry robot. (b) Close-up view of deposition tool.

The deposition tool was a linear actuator-driven syringe with interchangeable syringe tips that served as nozzles of various diameters, ranging from 0.33 mm – 0.84 mm. The maximum volumetric flow rate was 1.4 mL/s. A disposable syringe served as the material bay of the deposition tool. The material bay simply slid-out of the deposition tool in order to facilitate multiple-material print jobs in which the material cartridge was frequently interchanged in mid-print.

a)

b)
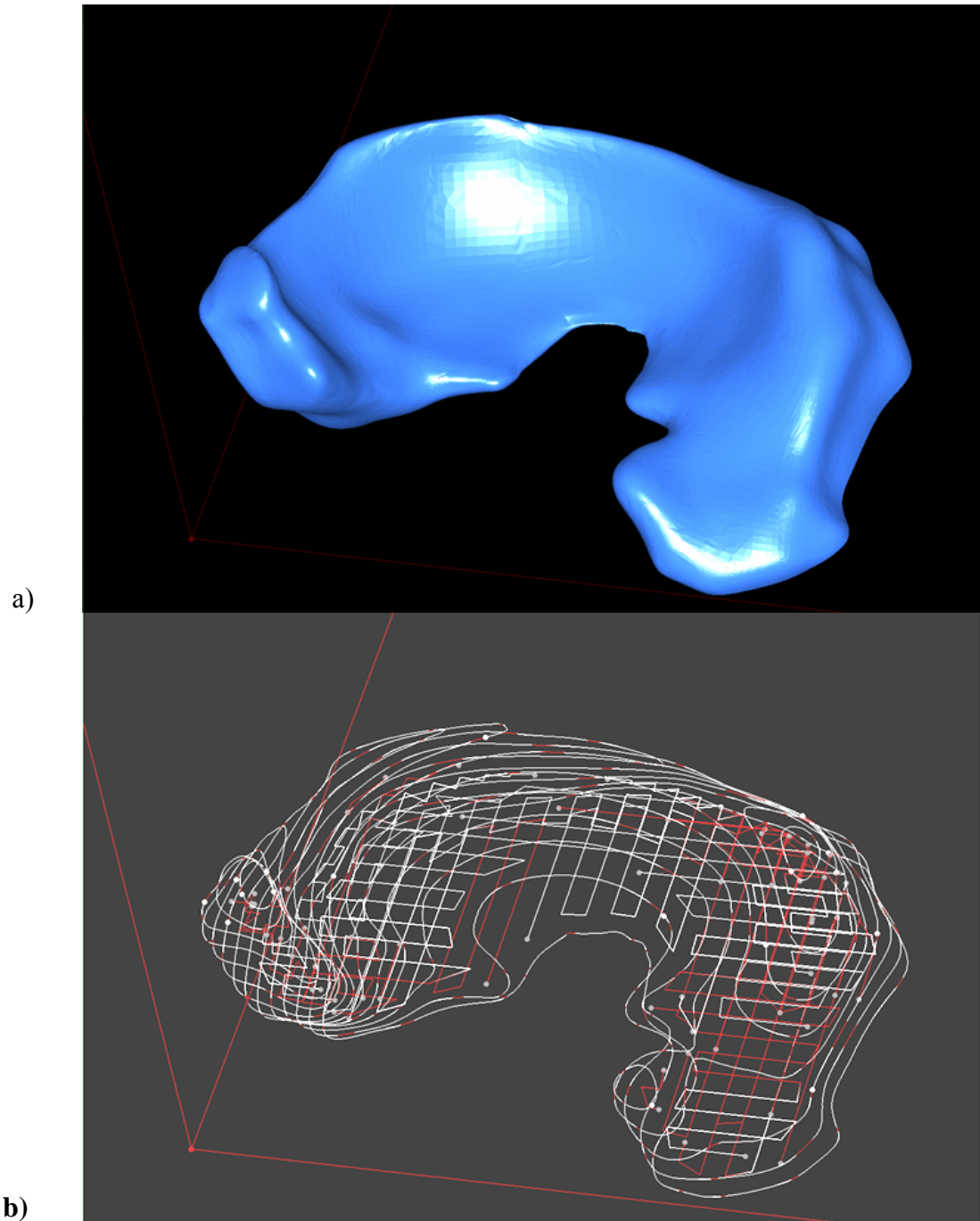
Figure 1.2. Screenshot of trajectory planner. (a) CAD model loaded into trajectory planning software before tool-path generation. (b) Planned tool-paths.

Once the system was loaded with printing material, a CAD model was sent to the robot's control system in Stereolithography (STL) format, a computer file format commonly used in rapid prototyping applications. Custom-written software sliced the

model and planned tool paths within each layer. The tool-path planner prescribed a contour boundary path followed by raster fill-paths. The trajectory was sent from the computer to the robot and printing commenced (Figure 1.2).

Cell Isolation and Culture

Cartilage was harvested from the femeropatellar groove of 1-3 day old calves. The tissue was digested for 18 hours at 37°C and 5% CO_2 in Dulbecco's Modified Eagle Medium (DMEM) containing 0.3% collagenase. The digest solution was filtered with a 100 μm cell strainer. The articular chondrocytes were isolated from the strained digest solution by centrifugation at 412 g for 7 minutes. Cells were washed twice with Phosphate Buffered Saline (PBS)[24]. The initial viability was determined using Trypan blue (Mediatech; Herndon, VA)

Samples were cultured in DMEM with 10% fetal bovine serum. A 1% antibiotic-antimyotic (10,000 units/mL penicillin G sodium, 10,000 µg/mL streptomycin sulfate, 25 µg/mL amophoterocin B in 0.85% saline) was also added to the growth medium, except during the sterility test. The cells were cultured at 37ºC and 5% CO_2[14].

Gel Deposition

During the printing experiments a tip diameter of 0.84 mm was selected. The robot planned the tool paths for material streams with a width of 1.2 mm and a height of 0.8 mm. The gel flow rate was 0.6 mL/min. At the start of each new path, the deposition started 0.2 seconds before the motion of the gantry robot.

Chemical Formulation and Cell Encapsulation

The chondrocytes were suspended in PBS and spun-down into a pellet with a centrifuge. Low-viscosity, high G-content non-medical grade LF10/60 alginate (FMC Biopolymer; Drammen, Norway) was dissolved at a concentration of 20 mg/mL, passed through a 0.22 μm filter, and added to the cell pellet to achieve a density of 50×10^6 cells/mL. The alginate-cell suspension was vortexed and mixed in a 2:1 ratio with autoclaved 10 mg/mL $CaSO_4$ in PBS. After mixing, the resulting hydrogel had a cell density of 33×10^6 cells/mL. Due to the time dependent gelation process, the window for optimal printing was approximately 15 minutes from the time that the crosslinker is mixed with the alginate. The hydrogel was loaded into a syringe and inserted into the deposition tool.

Viability Test

The viability of the deposition process was measured by testing viability immediately before and after the printing process. The process viability was defined as the ratio of cell viability after harvesting but before gel-seeding to the cell viability immediately after deposition. Twenty-four disks, 6 mm (D) × 2 mm (H), were printed into a 24-well plate. Each sample was pulled from the plate and tested with the Live/Dead Viability Assay (Molecular Probes; Eugene, OR). The samples were exposed to 0.15 µM calcein AM and 2 µM ethidium homodimer-1 (EthD-1) for 60 minutes at room temperature. The stained samples were analyzed under a Nikon TE2000-S microscope equipped with an epiflourescence attachment and a Spot RT digital camera. The viability was calculated as the average of the ratios of live over total cells in a given field.

Sterility

   An empty autoclave bag was sealed and autoclaved. The sealed bag was placed under a sterile hood, a slit was cut into the bottom end of the bag and a sterile 24-well plate was inserted. The bag was resealed with tape and ready for printing. The autoclave bag served as a sterile envelope around the plate which protected the printed samples from contamination.

   To test the effectiveness of the envelope concept, twenty-four disks, 6 mm (D) X 2 mm (H), were printed into an envelope-protected sterile plate and cultured for 8 days without antibiotics or antimyotics. After the incubation period, media from each well was pulled and tested for bacterial presence with 100 µM BacLight Green Stain (Molecular Probes), according to the kit manufacturer's instructions. Bacterial counts were performed using a hemacytometer (Hausser Scientific; Horsham, PA) and a Nikon TE2000-S microscope equipped with an epiflourescence attachment and a digital camera.

DNA Content and ECM Accumulation

   Disks, 6 mm (D) × 2 mm (H), were printed into a 24-well plate. The disks were cultured for a period of time ranging from 0 to 142 days. Disks were removed from culture, weighed, lyophilized, and weighed again. All of the dry samples were digested in 1 mL of papain digest buffer (0.1 mol/L sodium phosphate, 10 mmol sodium EDTA [BDH], 10 mmol cysteine hydrochloride [Sigma-Aldrich; St. Louis, MO], and 3.8 U/mL papain [Sigma]) at 65°C for 24 hours.

   The digest was analyzed for DNA content, as a marker of cell quantity. The assay was carried-out in 96-well plates (Nalge Nunc; Rochester, NY). In each well, 190 µL of 0.1 µg/mL Hoechst 33258 dye in TES buffer was added to 10 µL of the digested samples. Calf thymus DNA was used as a standard and the absorbance was

read using a Tecan microplate reader with the excitation wavelength set at 348 nm and the emission wavelength set at 456 nm[25].

The digest was also analyzed for glycosaminoglycans (GAG), as a marker of proteoglycans. The assay was carried-out in 96-well plates. In each well, 50 μL of digest was mixed with 250 μL of dye containing 16 mg/L 1,9-Dimethylmethylene blue (DMMB) and 3.04 g/L Glycine at pH 1.5. The absorbance was read at 595 nm using a microplate reader. Chondroitin-6-Sulfate from shark cartilage (Sigma) was used to construct the standard curve[26].

Additionally, the digest was analyzed for hydroxyproline, as a marker of collagen. One hundred μL of each sample's digest was hydrolyzed in 100 uL of 2N NaOH at 110°C for 18 hours. The following were combined into screw-cap microfuge tubes: 20 μL 5N HCl, 100μL digested hydrolyzed sample, 100 μL 0.01 M $CuSO_4$, 100 μL 2.5 N NaOH, 100 μL 6% H_2O_2. After the addition of H_2O_2, the tubes were allowed to sit at room temperature for about 5 minutes while being shaken occasionally to remove gas bubbles. The tubes were then vortexed and placed in a heat block at 80°C for 5 minutes. The tubes were placed in an ice bath until cooled to room temperature. Four hundred μL of 3N H_2SO_4 and 200 μL of DMAB were added to each tube. Each well of a 96-well plate was filled with 200 μL of a treated sample and absorbance was read at 540 nm[27].

Mechanical Characterization

Disks less than one hour old, 6 mm (D) × 2 mm (H), were printed and placed in an ELF 3200 (EnduraTec; Minnetonka, MN) mechanical test-frame in an unconfined compression chamber between two parallel plates. A 1000 gram load cell (Sensotec; Columbus, OH) was attached to the bottom plate and a displacement sensor to the top plate. The bottom plate was filled with PBS in order to completely

encompass the sample with fluid. The two plates started at a distance corresponding to 0% strain and stepped 0.1 mm towards each other every 100 seconds until 45% strain was achieved. Stress and strain data were acquired at a frequency of 5 Hz[28].

The stress-strain curve of each printed sample was analyzed by first finding the equilibrium stress corresponding to each imposed strain (0% – 45%). The linear region of the equilibrium stress-strain curve was linearly fit; the slope of this line was the Young's modulus of the sample.

Geometric Fidelity

The geometric fidelity of the printing process was determined by using the printing platform as a Coordinate Measuring Machine (CMM). A metal needle was attached to the deposition tool with a wire soldered to the needle. Another wire was attached to the metal base plate of the printer and an electrical power source. Since the hydrogels being measured were electrically conductive, when the needle touched the alginate hydrogel, current flowed from the power source, through the base plate, through the hydrogel sample and back to the tip – thus completing the electrical circuit. Positional data was logged when the robot sensed that the electrical circuit was completed. By stepping over the entire part in 0.35 mm X-Y coordinate increments, a map of the surface points of the hydrogel sample was constructed.

Using the surface map, the average height of the X-Y plane boundary points was calculated; these points represented the height of the base plate. The Z coordinates of all points was shifted down by the mean boundary height in order to make the base plate aligned with the X-Y plane. The list of points was truncated to exclude all points which represented the base plate itself, (i.e., all points with zero valued z-coordinates were removed.) The mean X and Y coordinates were calculated

and then the X and Y coordinates of the points were shifted by the mean values in order to center the samples in the X-Y plane.

The overall average height of the sample was calculated by finding the mean z-value of the points. The average height, excluding the edge effect, was calculated by finding the mean z-value of the points that were in the inner X-Y region of the geometry; that is, all points whose X and Y coordinates fell within 90% × 90% of the total X-Y cross-section. The RMS surface roughness was determined to be the standard deviation of these inner points.

In order to calculate the X-Y geometric fidelity, the point list was further truncated to exclude all points with z-values below half the total average height; doing so removes the effect of the sloping interface between the walls of the geometry and the base plate. The X-Y boundary points were identified using a standard convex hull algorithm, "convhull," in MATLAB (MathWorks; Natick, Massachusetts). These X-Y boundary points were subtracted by the intended X-Y coordinate corresponding to each point in order to generate an X-Y error map. The mean and standard deviation of this error was calculated to reflect the X-Y geometric fidelity.

RESULTS

Spatially Heterogeneous Gel Constructs

A set of gel constructs was created to showcase the ability of the system to fabricate complex, spatially heterogeneous hydrogel geometries. A crescent-shaped part, 2.5 cm (L) × 0.75 cm (W) was printed and elevated with a thin utensil to verify that the part maintained its shape while fully supporting its weight (Figure 1.3). The crescent-shaped part was drawn in the SolidWorks CAD program (Figure 1.4-a1), input into the printer's control software, and printed (Figure 1.4-a2).

Figure 1.3. Printed crescent suspended with tool.

To verify the system's ability to construct a multiple-material, spatially heterogeneous construct, an IV disc-shaped CAD model was generated (Figure 1.4-b1), processed with the robot's control software, and printed (Figure 1.4-b2). The two-material component was fabricated from two different batches of alginate hydrogel, each stained with a dye of a different color. Utilizing the multiple-material capabilities of the robotic platform, the robot stopped at numerous points throughout the print and requested a change of materials, as prescribed by the robot's tool path planner. At each of these points, the material bay and syringe tip unit of the

deposition tool was manually swapped with the designated material bay/syringe tip unit and printing commenced.

In order to demonstrate the system's ability to create implants with complex geometries, a CAD model of an ovine meniscus was constructed from a CT scan (Figure 1.4-c1), and printed (Figure 1.4-c2).
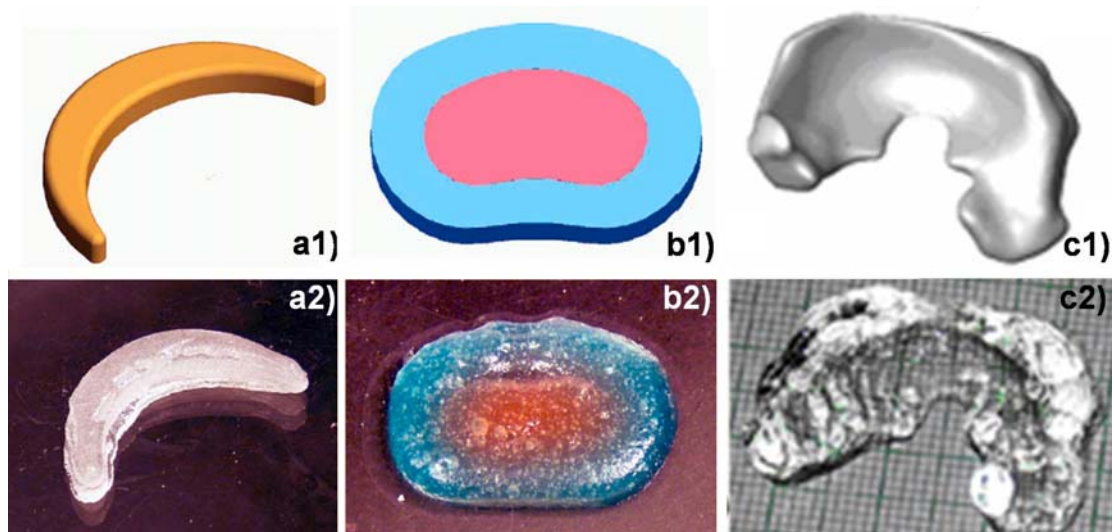
Figure 1.4. CAD models and photographs of printed samples. (a1) CAD model of first-order approximation of meniscus. (a2) Printed first-order approximation of meniscus. (b1) CAD model of two-material first-order approximation of intervertibral disc. (b2) Printed first-order approximation of intervertibral disc. (c1) Micro-CT scan of ovine meniscus. (c2) Printed construct from ovine meniscus CT scan.

Viability and Sterility

Viability tests successfully detected both live (Figure 1.5-a) and dead (Figure 1.5-b) cells in printed gels. The viability of the printing process was determined to be 94±5% (n=15). The viability appeared to be spatially uniform. By inspection with phase contrast microscopy and fluorescence microscopy, the cell distribution was observed to be homogeneous. When inspected by phase contract microscopy, no abnormal morphology was observed.
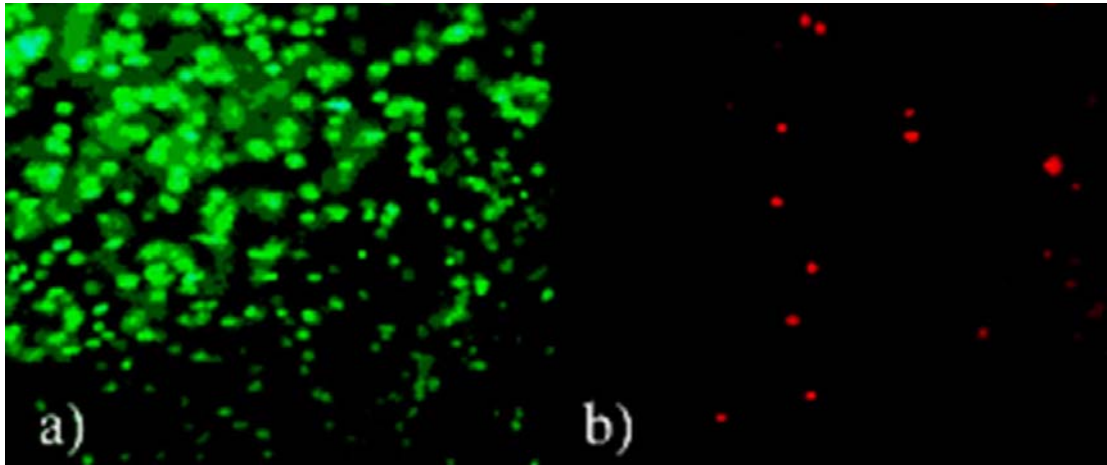
Figure 1.5. Live and dead panels of the same view field from the viability test. (a) Live panel. (b) Dead panel.

After 8 days of incubating a printed gel samples without any antibiotics or antimyotics, less than 1 bacterium per 0.9 μL was detected (n=12).

ECM Accumulation

GAG content increased in printed samples over time in incubation to 18.9±4.2 ug/ug DNA (n=4-17) by 3 weeks (Figure 1.6). Printed disks were cultured beyond 3 weeks to ~ 18 weeks, but GAG level did not change significantly.

Hydroxyproline content increased in the printed samples over time in incubation, as well. Hydroxyproline content reached 0.92±0.15 ug/ug DNA (n=4-17) by 14 weeks (Figure 1.7). At 18 weeks, the disks did not appear to change shape grossly when compared to disks exposed to media immediately after printing (Figure 1.8).
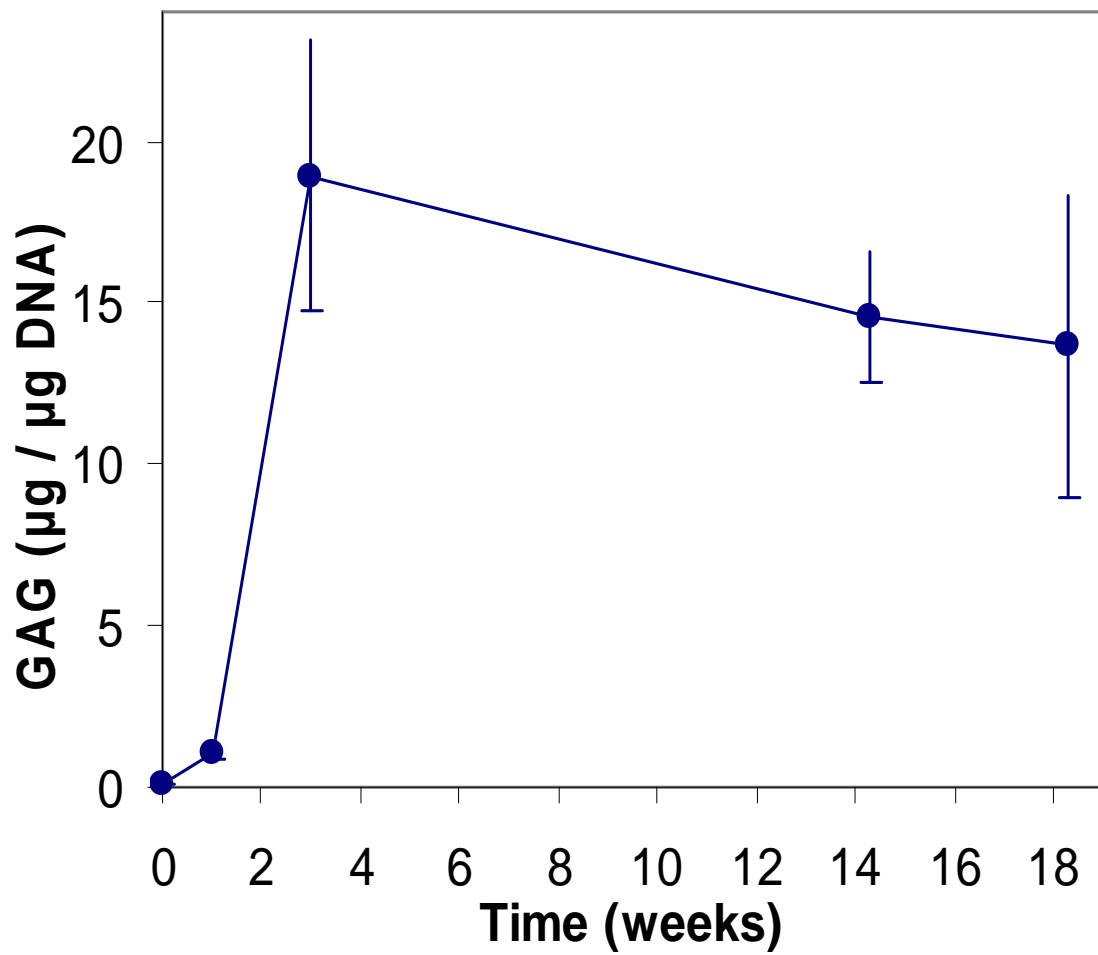
Figure 1.6. GAG content DNA normalized with time in culture.
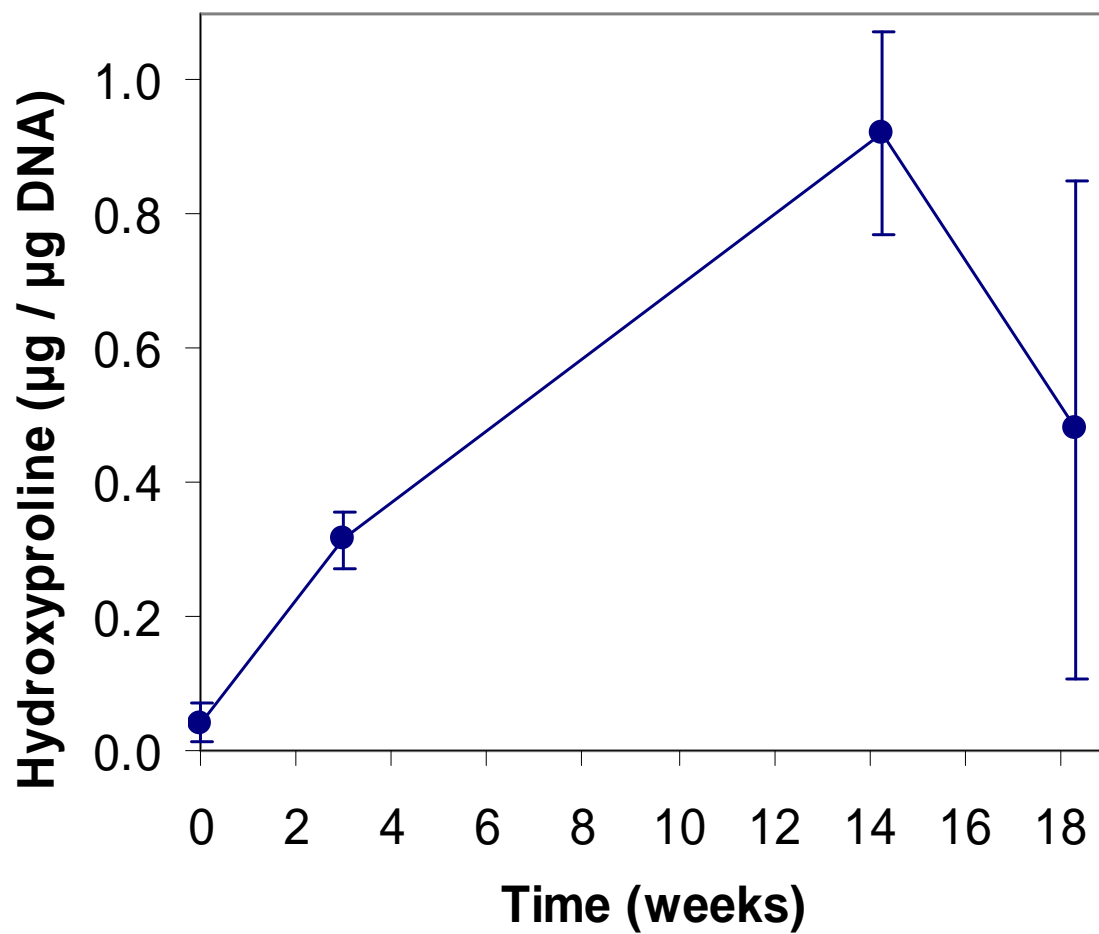
Figure 1.7. Hydroxyproline content DNA normalized with time in culture.

Mechanical Properties

It was observed that the Young's Modulus of samples increased with time after fabrication. The compressive elastic modulus of a typical printed disk that was less than 1 hour old, was determined to be 1.8±0.1 kPa (n=6).
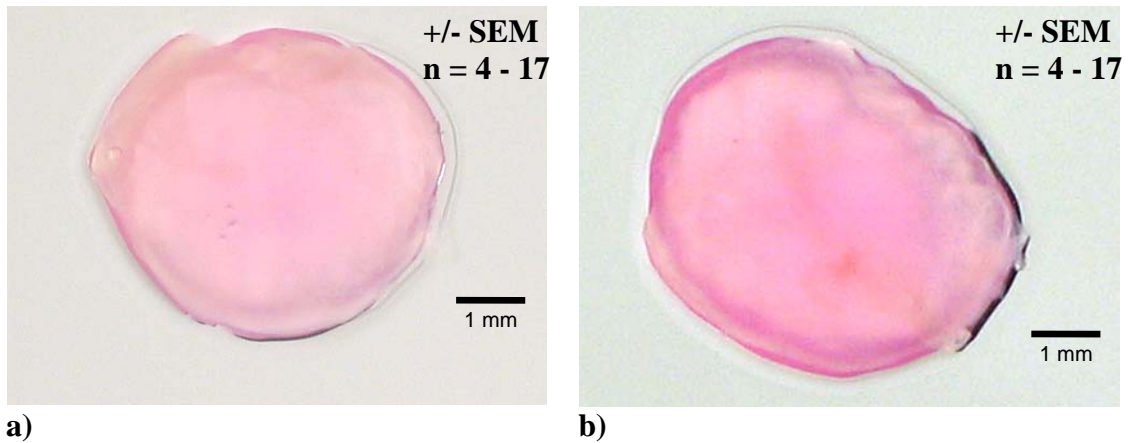
Figure 1.8. Photographs of printed discs with different culture times. (a) Printed disc after 1 day in culture. (b) Printed disc after 142 days in culture.
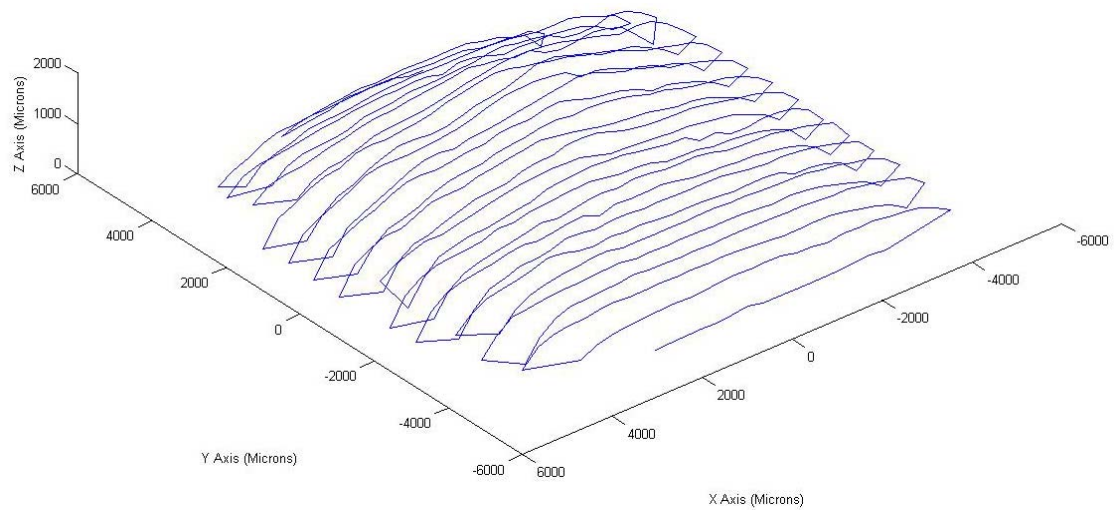
Figure 1.9. Centered and truncated CMM data for an 8mm by 8mm printed geometry.

Geometric Fidelity

When the point maps of the entire printed samples (Figure 1.9) were considered, the average height of a single layer was determined to be 0.80±0.03 mm and the RMS surface roughness was 0.33±0.01 mm. When only the points with X-Y coordinates located in the inner region of the printed samples, the edge effect was ignored and the resulting average height was 1.14±0.06 mm and the RMS surface roughness was 0.16±0.02 mm.

When the X-Y error was analyzed at the mid-height plane (Figure 1.10), the average X-Y error was found to be 0.58±0.07 mm. The standard deviation of the X-Y error was found to be 0.27±0.03 mm.
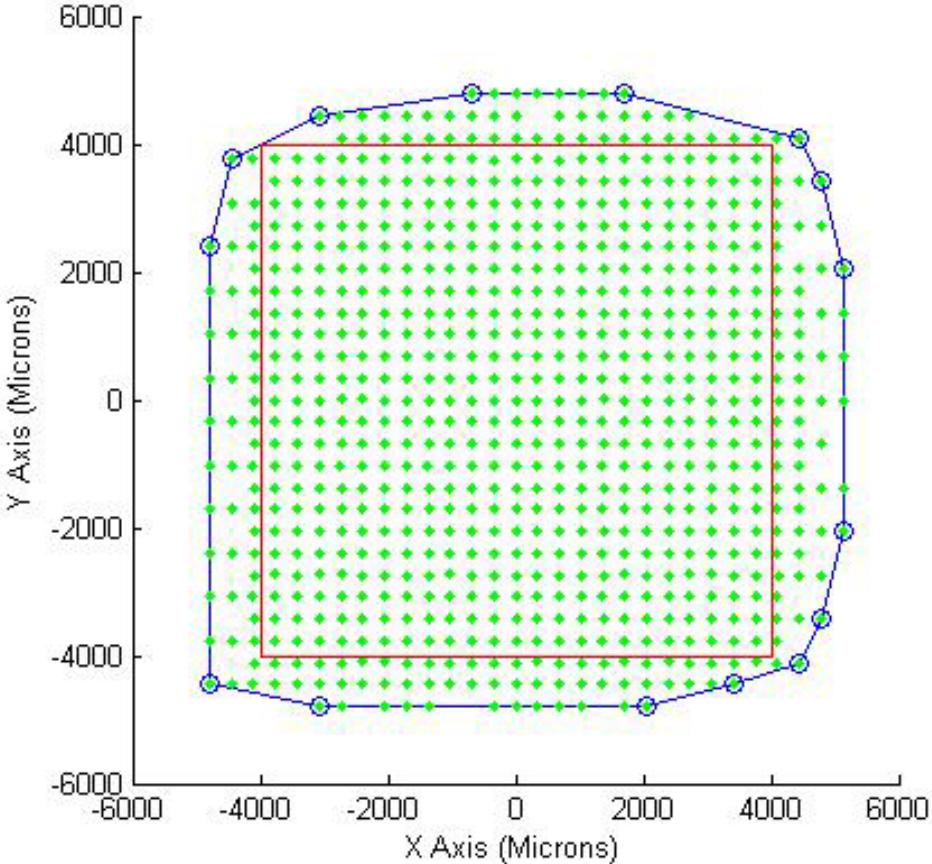
Figure 1.10. Cross-section of CMM map truncated at mid-height.

DISCUSSION

The objective of this research was to develop a technique for directly fabricating pre-seeded constructs in arbitrary geometries with multi-axial zonal organization. In order for the technique to be considered a feasible tissue engineering approach, we focused on a set of benchmarks including: process viability, process sterility, ECM production by printed samples, and mechanical properties of printed samples.

Samples printed into simple geometries retained their shape for the duration of a 20 week culture. This points to an advantage of using alginate as a matieral delivery system for 3D printing. Other materials proposed for such applications are highly amenable to printing[22], but do not retain their shape in culture, due to contraction, in the case of collagen, or swelling and dissolution, in the case of Pluronic F127.

The results of the viability test suggest that the printing process, including the cell encapsulation and gel deposition stages, does not have a major harmful impact on the cell viability of printed cells. A 94±5% process viability is adequate for a new tissue engineering technique. This viability value is markedly higher than other SFF approaches to pre-encapsulated construct fabrication, which are in the range of 60% - 70%[20].

The bacteria count of less than 1 bacterium per 0.9 µL of media suggests that the samples were bacteria free and that the sterile envelope technique worked sufficiently well. The autoclave bag served as an inexpensive and disposable sterile envelope which can be fit to a printing workspace of any size. The use of an environmental envelope reduced the demands placed on the sterility of the production site. Furthermore, other than the syringe and syringe tip, the printer itself did not need to be sterilized. This technique would enable future applications in which the maintenance of environmental sterility would otherwise be challenging.

The peak GAG content of 18.9 ug/ug DNA and the peak hydroxyproline content of 0.92 ug/ug DNA were similar to those observed in a number of studies in which bovine articular chondrocytes were seeded onto a variety of substrates (Table 1.1). This suggests that the printing process did not substaintially interfere with the ability of printed cells to assemble an extracellular matrix.

Table 1.1. Comparison of ECM properties.

	Alginate Beads	**Alginate Injection Molding**	**Alginate SFF**
GAG (μg / μg DNA)	28[26] (3 weeks)	18[28] (10 weeks)	18.9±4.2 (3 weeks)
Hydroxyproline (μg / μg DNA)	2.8[26] (3 weeks)	1.8[28] (10 weeks)	0.92±0.15 (14 weeks)
	1.9[29] (6 weeks)		

The elastic modulus of the alginate hydrogel printed samples was higher than the modulus of samples created by some other SFF techniques which created pre-seeded implants. The modulus of alginate printed samples was higher than those created with the protocrosslinking SFF technique[20]. Also, alginate hydrogels are much stiffer than those made from Pluronic F-127, which was been investigated as a build material for SFF tissue engineering approaches[22]. Further, the mechanical properties of printed alginate implants could be easily improved through addition of calcium in or after the printing process.

The tissue engineering approach detailed herein combines the strengths of molding techniques with those of Solid Freeform Fabrication technology. This technology successfully encapsulates bovine chondrocytes in alginate hydrogel and deposits them in arbitrary geometries while maintaining sterility and viability. Unlike injection molding of pre-seeded alginate hydrogel, this technique does not require

molds, nor does it require any custom tooling to fabricate an implant. Also, due to the inherent benefits of SFF, implants with complex geometries can be fabricated that could not otherwise be molded or easily fabricated using other methods such as layering sheets.

This tissue engineering approach combines the strength and biocompatibility of hydrogel injection molding with the geometric freedom and inherent patient-specificity capabilities of SFF. The method could allow for efficient fabrication of patient-specific implants without the cost and delay normally associated with creating custom tooling. Furthermore, this technique reduces the constraints imposed upon the fabrication environment, which is an important concern for in situ and minimally invasive in vivo implant fabrication. This technology could enable fabrication of geometrically complex, multiple-material implants that would otherwise not be producible. Also, this approach could enable the fabrication of large implants which would otherwise be difficult to seed with cells due to transport limitaitons.

REFERENCES

[1]   Y. Cao, J. P. Vacanti, K. T. Paige, J. Upton, and C. A. Vacanti, "Transplantation of chondrocytes utilizing a polymer-cell construct to produce tissue-engineered cartilage in the shape of a human ear," *Plastic and Reconstructive Surgery,* vol. 100, p. 297, 1997.

[2]   W. S. Kim, J. P. Vacanti, L. Cima, D. Mooney, J. Upton, W. C. Puelacher, and C. A. Vacanti, "Cartilage engineered in predetermined shapes employing cell transplantation on synthetic biodegradable polymers," *Plastic and Reconstructive Surgery,* vol. 94, p. 233, 1994.

[3]   W. C. Puelacher, J. Wisser, C. A. Vacanti, N. F. Ferraro, D. Jaramillo, and J. P. Vacanti, "Temporomandibular joint disc replacement made by tissue-engineered growth of cartilage," *Journal of Oral and Maxillofacial Surgery,* vol. 52, pp. 1172-1177, 1994.

[4]   Y. Weng, Y. Cao, C. Arevalo, M. P. Vacanti, and C. A. Vacanti, "Tissue-engineered composites of bone and cartilage for mandible condylar reconstruction," *Journal of Oral and Maxillofacial Surgery,* vol. 59, pp. 185-190, 2001.

[5]   C. Ibarra, C. Jannetta, C. A. Vacanti, Y. Cao, T. H. Kim, J. Upton, and J. P. Vacanti, "Tissue engineered meniscus: a potential new alternative to allogeneic meniscus transplantation," *Transplantation Proceedings,* vol. 29, pp. 986-988, 1997.

[6]   K. Kojima, L. J. Bonassar, R. A. Ignotz, K. Syed, J. Cortiella, and C. A. Vacanti, "Comparison of tracheal and nasal chondrocytes for tissue engineering of the trachea," *The Annals of Thoracic Surgery,* vol. 76, p. 1884, 2003.

[7]   H. Mizuno, A. K. Roy, C. A. Vacanti, K. Kojima, M. Ueda, and L. J. Bonassar, "Tissue-engineered composites of anulus fibrosus and nucleus pulposus for intervertebral disc replacement," *Spine,* vol. 29, p. 1290, 2004.

[8]   S. H. Kamil, K. Kojima, M. P. Vacanti, L. J. Bonassar, C. A. Vacanti, and R. D. Eavey, "In vitro tissue engineering to generate a human-sized auricle and nasal tip," *Laryngoscope,* vol. 113, p. 90, 2003.

[9]   W. C. Puelacher, D. Mooney, R. Langer, J. Upton, J. P. Vacanti, and C. A. Vacanti, "Design of nasoseptal cartilage replacements synthesized from biodegradable polymers and chondrocytes," *Biomaterials,* vol. 15, p. 774, 1994.

[10]   W. C. Puelacher, J. P. Vacanti, N. F. Ferraro, B. Schloo, and C. A. Vacanti, "Femoral shaft reconstruction using tissue-engineered growth of bone,"

International Journal of Oral & Maxillofacial Surgery, vol. 25, pp. 223-228, 1996.

[11]   C. A. Vacanti, L. J. Bonassar, M. P. Vacanti, and J. Shufflebarger, "Replacement of an avulsed phalanx with tissue-engineered bone," *New England Journal of Medicine,* vol. 344, p. 1511, 2001.

[12]   C. T. Hung, E. G. Lima, R. L. Mauck, E. Taki, M. A. LeRoux, H. H. Lu, R. G. Stark, X. E. Guo, and G. A. Ateshian, "Anatomically shaped osteochondral constructs for articular cartilage repair," *Journal of Biomechanics,* vol. 36, pp. 1853-1864, 2003.

[13]   Y. Cao, A. Rodriguez, M. Vacanti, C. Ibarra, C. Arevalo, and C. A. Vacanti, "Comparative study of the use of poly (glycolic acid), calcium alginate and pluronics in the engineering of autologous porcine cartilage," *Journal of Biomaterials Science, Polymer Edition,* vol. 9, pp. 475-487, 1998.

[14]   S. C. Chang, J. A. Rowley, G. Tobias, N. G. Genes, A. K. Roy, D. J. Mooney, C. A. Vacanti, and L. J. Bonassar, "Injection molding of chondrocyte/alginate constructs in the shape of facial implants," *Journal of Biomedical Materials Research,* vol. 55, pp. 503-511, 2001.

[15]   T. J. Klein, B. L. Schumacher, T. A. Schmidt, K. W. Li, M. S. Voegtline, K. Masuda, E. Thonar, and R. L. Sah, "Tissue engineering of stratified articular cartilage from chondrocyte subpopulations," *Osteoarthritis and Cartilage,* vol. 11, pp. 595-602, 2003.

[16]   T. K. Kim, B. Sharma, C. G. Williams, M. A. Ruffner, A. Malik, E. G. McFarland, and J. H. Elisseeff, "Experimental model for cartilage tissue engineering to regenerate the zonal organization of articular cartilage," *Osteoarthritis and Cartilage,* vol. 11, pp. 653-664, 2003.

[17]   K. W. Ng, C. C. B. Wang, R. L. Mauck, T. A. N. Kelly, N. O. Chahine, K. D. Costa, G. A. Ateshian, and C. T. Hung, "A layered agarose approach to fabricate depth-dependent inhomogeneity in chondrocyte-seeded constructs," *Journal of Orthopaedic Research,* vol. 23, pp. 134-141, 2005.

[18]   W. Sun, B. Starly, A. Darling, and C. Gomez, "Computer-aided tissue engineering: application to biomimetic modelling and design of tissue scaffolds," *Biotechnology and Applied Biochemistry,* vol. 39, pp. 49-58, 2004.

[19]   J. Ballyns, J. Gleghorn, V. Niebrzydowski, J. Rawlinson, S. Maher, and L. J. Bonassar, "Tissue engineering of meniscus using microCT imaging, CAD and injection molding," in *51st Annual Meeting of the Orthopaedic Research Society*, Washington, D.C., 2005.

[20] B. Dhariwala, E. Hunt, and T. Boland, "Rapid prototyping of tissue-engineering constructs, using photopolymerizable hydrogels and stereolithography," *Tissue Engineering,* vol. 10, pp. 1316-1322, 2004.

[21] S. Khalil, J. Nam, and W. Sun, "Multi-nozzle deposition for construction of 3D biopolymer tissue scaffolds," *Rapid Prototyping Journal,* vol. 11, pp. 9-17, 2005.

[22] C. M. Smith, A. L. Stone, R. L. Parkhill, R. L. Stewart, M. W. Simpkins, A. M. Kachurin, W. L. Warren, and S. K. Williams, "Three-dimensional BioAssembly tool for generating viable tissue-engineered constructs," *Tissue Engineering,* vol. 10, pp. 1566-1576, 2004.

[23] E. Malone, K. Rasa, D. Cohen, T. Isaacson, H. Lashley, and H. Lipson, "Freeform fabrication of zinc-air batteries and electromechanical assemblies," *Rapid Prototyping Journal,* vol. 10, pp. 58-69, 2004.

[24] N. G. Genes, J. A. Rowley, D. J. Mooney, and L. J. Bonassar, "Effect of substrate mechanics on chondrocyte adhesion," *Archives of Biochemistry and Biophysics,* vol. 422, pp. 161-167, 2004.

[25] Y. J. Kim, R. L. Y. Sah, J. Y. H. Doong, and A. J. Grodzinsky, "Fluorometric assay of DNA in cartilage explants using Hoechst 33258," *Analytical Biochemistry,* vol. 174, pp. 168-176, 1988.

[26] B. O. Enobakhare, D. L. Bader, and D. A. Lee, "Quantification of sulfated glycosaminoglycans in chondrocyte/alginate cultures, by use of 1,9-dimethylmethylene blue," *Analytical Biochemistry,* vol. 243, pp. 189-191, 1996.

[27] R. E. Neuman and M. A. Logan, "The determination of hydroxyproline," *J Biol Chem,* vol. 184, pp. 299-306, 1950.

[28] Y. J. Kim, L. J. Bonassar, and A. J. Grodzinsky, "The role of cartilage streaming potential, fluid flow and pressure in the stimulation of chondrocyte biosynthesis during dynamic compression," *Journal of Biomechanics,* vol. 28, pp. 1055-1066, 1995.

[29] B. Beekman, N. Verzijl, R. A. Bank, K. v. d. Mark, and J. M. TeKoppele, "Synthesis of collagen by bovine chondrocytes cultured in alginate: posttranslational modifications and cell-matrix interaction," *Experimental Cell Research,* vol. 237, pp. 135-141, 1997.

CHAPTER 2: INCREASED MIXING IMPROVES HYDROGEL HOMOGENEITY AND QUALITY OF 3D PRINTED CONSTRUCTS[*]

ABSTRACT

As the tissue engineering and drug delivery communities place greater emphasis on producing constructs of complex geometry, 3D printing is becoming as an increasingly important technique. While numerous tissue printing techniques have emerged, little has been done to characterize the properties of printing inks and the resultant effects on geometric fidelity, cell viability and mechanical integrity. These questions have been neglected largely because of the lack of methods to characterize the real-time properties of printing inks. We present a novel technique for characterizing the homogeneity of hydrogel tissue printing inks that measures loads during ink deposition and its temporal variation, called, "mechanical noise." We then used this technique to determine the effects of increased mixing on the homogeneity of alginate hydrogels and determined whether this results in improved geometric fidelity of printed constructs. We also studied potential adverse effects on cell viability and mechanical integrity of printed parts. Increased mixing between alginate and crosslinker to 128 cycles yielded an 82% reduction in mechanical noise. Geometric fidelity also improved with this increased mixing, in terms of a smoother surface texture, better matching of the target geometry, and fewer point defects. Viability was not adversely affected by increased mixing, and it actually improved by 34% with a 45 minute curing time. As mixing prior to printing was increased from 8 to 200 cycles, the modulus also increased by 110% from 4.0 ± 0.1 kPa to 8.4 ± 1.0 kPa. The results

[*] Daniel L. Cohen[1], Winifred Lo[1,2], Andrew Tsavaris[1,3], David Peng[4], Hod Lipson[1,5], Lawrence J. Bonassar[1,4]; [1]Cornell University, Mechanical and Aerospace Engineering, Ithaca NY; [2]Northwestern University, Biomedical Engineering, Evanston IL; [3]Princeton University, Chemical Engineering, Princeton NJ; [4]Cornell University, Biomedical Engineering, Ithaca NY; [5]Cornell University, Computing and Information Science, Ithaca NY.

presented herein motivate a radical shift in alginate printing protocol, and also propose a useful methodology for characterizing 3D printing materials.

INTRODUCTION

Hydrogels are an increasingly important class of biomaterials for tissue engineering and drug delivery. These materials have long been used for cell delivery in beads[1,2], disks[3] and injectable form[4], and recently their use has been extended to processes such as injection molding[5-11] and 3D printing[12-26]. While recently emerging 3D printing applications hold tremendous potential, there are specific challenges associated with using hydrogels for 3D tissue printing. This process requires controlling the sol-gel transition such that the material is sufficiently inviscid while being extruded out of a print nozzle (to preserve mechanical integrity despite shear forces), and yet viscous enough to hold its shape when patterned on a substrate. This process must also preserve cell viability by minimizing shear forces on cells during deposition and avoiding the use of cytotoxic initiators of the sol-gel transition. Toward this end, a number of strategies have been employed including the use of photocrosslinkable (PEG[12,19,22]) and thermoreversible (gelatin[17,18,23-26], pluronic[21], collagen[18,20,21]) polymers. Our previous work has used ionically crosslinked alginate hydrogels[16,25,26], with $CaSO_4$ employed to initiate gelation prior to material deposition[14].

Although this process can be used successfully for 3D tissue printing, it is vulnerable to high levels of variability, both within a given print and across consecutive prints. Due to the rapid kinetics of gelation upon contact with calcium, ionic crosslinking of alginate can generate heterogeneous gels[14], which could be detrimental to the tissue printing process. While distribution of calcium ions is a concern that is unique to alginate-based systems, spatial uniformity of crosslinking is

likely an issue for all hydrogel-based printing techniques. Such heterogeneity may result from gradients in either chemical crosslinkers or the physical phenomena that induce crosslinking (e.g. heat or light). Despite this concern, there has been little effort to evaluate the uniformity of printing material or the homogeneity of printed parts. Attempts to conduct such evaluation have been hampered by the lack of methods available for assessing the properties of these hydrogels in real-time during deposition from a print nozzle.

One particularly important process parameter, perhaps most pertinent to the homogeneity of the resultant gels, is the amount of mixing used to combine the alginate and crosslinker solutions prior to printing. This poorly understood process parameter was never studied in a 3D printing context. It was previously thought that 8 mixings through as stopcock was sufficient for 3D printing gels (a process inherited from the technique's injection molding heritage[5-11]), and that increased mixing would not necessarily improve gel homogeneity or printed-part geometric fidelity. Furthermore, it was assumed that increased mixing would adversely affect gel mechanical integrity and cell viability due to increased shearing. Despite established hydrogel injection molding protocol suggesting that 8 mixings were sufficient[5-11], more recent anecdotal evidence suggested that increased mixing could possibly lead to increased gel homogeneity and consequently to improved geometric fidelity of printed parts. However, this new evidence was anecdotal and purely qualitative, and the effects on mechanical integrity and cell viability were still unknown.

The goals of this study were twofold: 1) to develop a quantitative method for characterizing hydrogel homogeneity during printing, and 2) to use this technique to determine whether increased mixing improved gel homogeneity and geometric fidelity of printed parts, while preserving cell viability and mechanical integrity. We present a novel characterization technique that measures extrusion force in real-time during

deposition and describes gel homogeneity in terms of the extrusion force temporal variation, called "mechanical noise." In addition to determining the effects of mixing on gel homogeneity, we used visual inspection to determine the effects of mixing on geometric fidelity of printed parts. We also used the Live/Dead assay and confined compression mechanical testing to determine whether gel homogeneity benefits came at the expense of cell viability and mechanical integrity, respectively.

MATERIALS AND METHODS

Cell Isolation

Chondrocytes were isolated from articular cartilage obtained from the femeropatellar groove of 1- to 3-day-old calves, as described previously[27]. The tissue was digested for 18 h at 37°C and 5% CO_2 in Dulbecco's modified Eagle medium (DMEM) containing 0.3% collagenase. The digest solution was filtered with a 100 μm cell strainer. The articular chondrocytes were isolated from the strained digest solution by centrifugation at 412 g for 7 min. Cells were washed twice with phosphate buffered saline (PBS). The initial viability was determined using trypan blue (Mediatech, Herndon, VA), and only batches of cells with viability of >90% were used.

Alginate Hydrogel Formulation and Cell Encapsulation

Alginate hydrogels for cell printing were prepared using techniques based on those described previously[14]. The alginate was prepared by mixing low-viscosity, high G-content non-medical grade LF10/60 alginate (FMC Biopolymer, Drammen, Norway) with PBS at a concentration of 20 mg/mL. For experiments requiring cell-seeded gels, cells were mixed into the alginate solution using a vortex spinner at a density of 50 million cells/mL prior to mixing with the crosslinker. The $CaSO_4$ crosslinker was prepared at a concentration of 10 mg/mL in PBS. The alginate and

crosslinker were combined in a 2:1 ratio and then mixed a variable number of times

(from 8 to 200 times, depending on the experiment) through a stopcock at 1 Hz. The

mixed alginate hydrogel was loaded into a syringe and allowed to cure for at least 15

minutes before use in any printing or experimentation.

Solid Freeform Fabrication System

      A Fab@Home open-source, open-architecture Solid Freeform Fabrication

(SFF) system was used for printing of the hydrogel[28] (Figure 2.1). This system, which

was designed and deployed by our lab, comprised a laser cut acrylic base with a three-

axis gantry motion system. Each axis was belt-driven and actuated by a stepper motor

(Haydon Switch & Instruments, Waterbury, CT). Communication and motion was

coordinated by a USB-interfaced electronic control board based on the Olimex LPC-

H2148 microcontroller. The open-source control software was written by our lab, and

along with the hardware design files, are freely available at www.fabathome.org. This

software imported CAD models in STL file format, sliced the geometries layer-wise

and planned tool paths for each layer based upon user-specified printing parameters.

The standard printing parameters used in the following experiments were: 0.68 mm

path width, 0.68 mm path height, and 10 mm/s gantry traverse rate. The software also

communicated with the control board and was responsible for coordinating motion

among the gantry axes and the deposition tool.
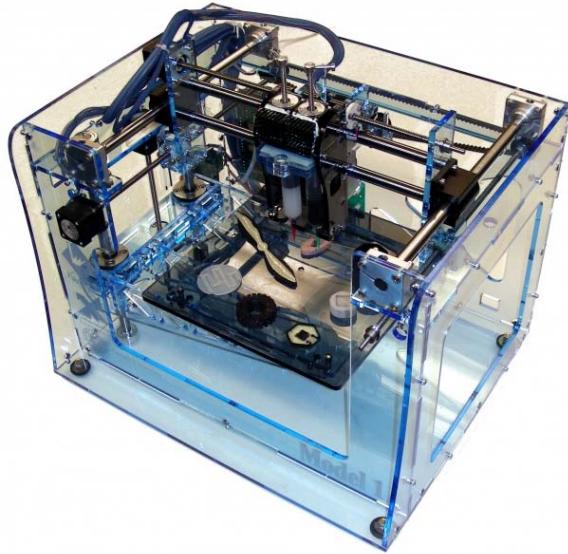
a)
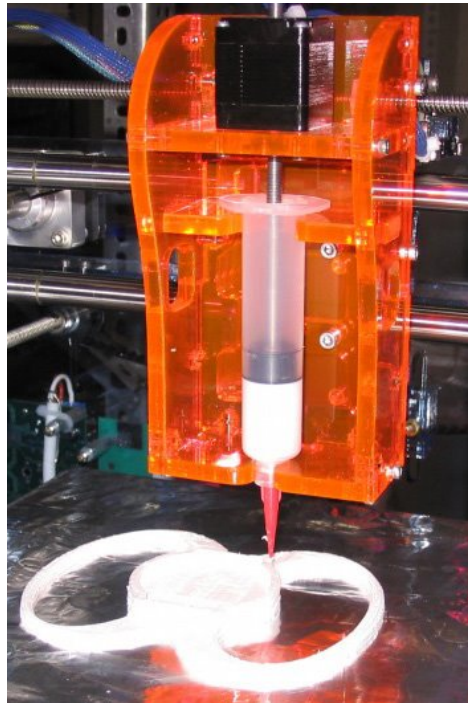
b)

Figure 2.1. Fab@Home open-source open-architecture 3D printing system. (a) Hardware comprising 3-axis gantry motion system and deposition tool. (b) The material-filled syringes plug into the Fab@Home's deposition tool, and a stepper motor pushes upon the plunger to extrude material through the Luer-lok deposition tip.

The standard Fab@Home deposition tool was modified in order to accommodate sterile syringes for biological applications. The deposition tool gripped

10 mL disposable syringes (Exel International Medical Products, St. Petersburg, FL) and pushed upon the syringe plunger with a stepper motor at 0.25 mm/s (Figure 2.1). Tapered Luer-lok syringe tips (EFD Inc., East Providence, RI) of 0.25 mm inner diameter were attached to the syringe barrel and were used as the nozzle. For experiments utilizing cells, each tip was sterilized in 70% isopropyl alcohol for 2 hours.

Measurement of Gel Homogeneity

Gel homogeneity was assessed by measuring the real-time extrusion force variation during deposition. With a perfectly homogenous deposition material, if a constant displacement rate were imposed on the syringe plunger, the uniformity of the material would yield a constant extrusion force. That is, the force required to achieve the target constant displacement rate would also be *constant*, and the magnitude would depend on the displacement rate, material viscosity and orifice diameter. By contrast, if the deposition material were compositionally heterogeneous, as portions of varying viscosity passed through the syringe tip, the force required to maintain a constant plunger displacement rate would vary. More specifically in the case of alginate hydrogel deposition, as clumps of over-crosslinked gel attempted to pass through the syringe tip at a constant displacement rate, the clumps' relatively high viscosity would cause the plunger extrusion force to increase; conversely, as under-crosslinked clumps passed through the syringe tip, the plunger extrusion force would decrease. Gels with greater compositional heterogeneity would exhibit greater temporal variation of the plunger extrusion force. This temporal variation in plunger extrusion force can be quantitatively represented by calculating the standard deviation of the plunger extrusion force over time. Herein, we call the standard deviation of the plunger extrusion force over time, "mechanical noise."

A novel experimental platform was devised to measure the "mechanical noise" exhibited by alginate hydrogels during prints. We needed to precisely measure the plunger extrusion forces that typically occur within a deposition tool. Toward this end, the syringe was held within a custom jig (Figure 2.2) that was mounted on an ELF3200 mechanical test-frame (EnduraTec, Minnetonka, MN). The jig was mounted to the static bottom plate of the test-frame and held the syringe vertically, similar to how the deposition tool houses the syringe. The mechanical test-frame's top plate was actuated and capable of being driven at constant displacement rates. A 50 lbs load cell (Sensotec, Columbus, OH) was mounted to the top plate of the test-frame and also connected to the syringe plunger via a custom adapter (Figure 2.2). The test-frame's actuated top plate behaved analogously to the stepper motor of the deposition tool, in that both imposed constant displacement rates onto the syringe plunger. The test-frame's top plate was displaced at 0.25 mm/s (the same linear rate as the deposition tool's stepper motor) in order to reproduce the syringe plunger extrusion rates that occur during printing, meanwhile, the in-line load cell collected force data at 200 Hz. The forces reproduced in the test-frame were highly representative of typical 3D printing scenarios since the extrusion rates were identical and the same wetted components (i.e., 10 mL Exel syringes and 0.25 mm diameter EFD syringe tips) were used in both systems. For these "mechanical noise" measurements, non-cell-seeded gels were prepared according to the protocol described above, and the extent of mixing was prescribed between 8 and 200 mixings.

a)
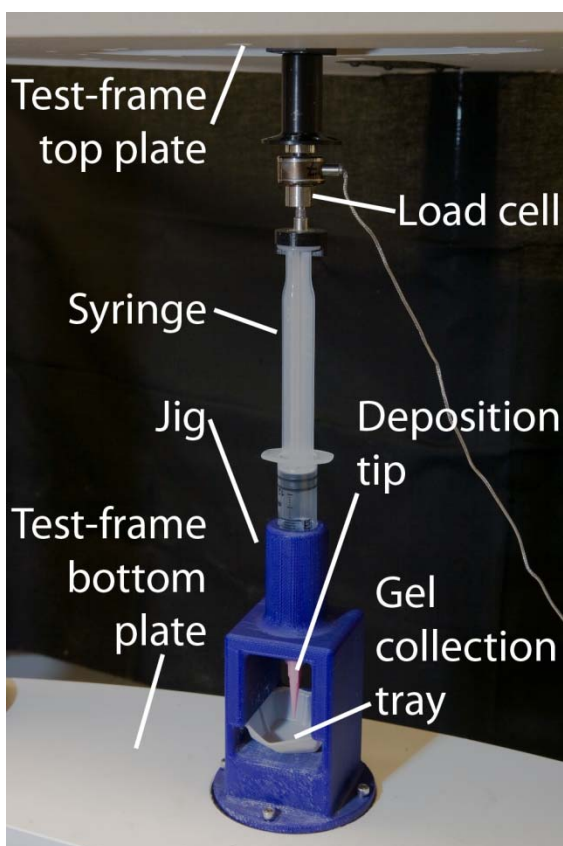
b)

Figure 2.2. Gel homogeneity characterization platform. (a) Gels are mixed by manually pumping alginate and crosslinker solutions through a 3-way stopcock at 1 Hz for a variable number of cycles, depending on the experiment. (b) For gel characterization, the syringe is held vertically by the custom jig and material is extruded through the deposition tip into a disposable weigh boat which serves as a collection tray. An in-line load cell measures the plunger extrusion force in real-time during deposition. The mechanical test-frame imposes a displacement at a constant rate and measures the plunger extrusion force with a 50 lbs. load cell at 200 Hz.

In order to accurately describe the "mechanical noise" of the gel, two types of noise needed to be filtered out from the raw plunger extrusion force data. Firstly, very high-frequency plunger extrusion force variation appeared to be a result of plunger-on-syringe wall friction (Figure 2.3). This high-frequency noise was determined to be non-material specific plunger-on-syringe friction because it was also present in tests performed with water. It was clear from these calibration experiments that the high-frequency component of the plunger extrusion force variation was not related to the deposition material heterogeneity. A second type of noise that needed to be filtered out was very low-frequency variation that was related to the taper of the syringe barrel. For practical reasons related to the injection molding process by which the syringes were manufactured, most commercial syringes are designed with a 1 degree taper, called the draft. Consequently, as the plunger moved deeper into the syringe barrel, the diameter decreased and the plunger-on-syringe wall friction increased which ultimately increased the plunger extrusion force. Again, this low-frequency phenomenon was also present in tests with water as the deposition material, and it was clear that the effect was unrelated to material heterogeneity.

The high-frequency friction and low-frequency draft effects were both removed so that the resultant extrusion force variation would be purely indicative of the material heterogeneity. To do so, a band-pass filter was applied to the plunger extrusion force. Force variations between the frequencies of 0.5 Hz and 40 Hz were passed; these threshold values were determined experimentally by using water as a calibration deposition material due to its low viscosity and high homogeneity. Finally, the "mechanical noise" was calculated as the standard deviation of the band-pass-filtered plunger extrusion force over 25 seconds, with the first 5 seconds disregarded.
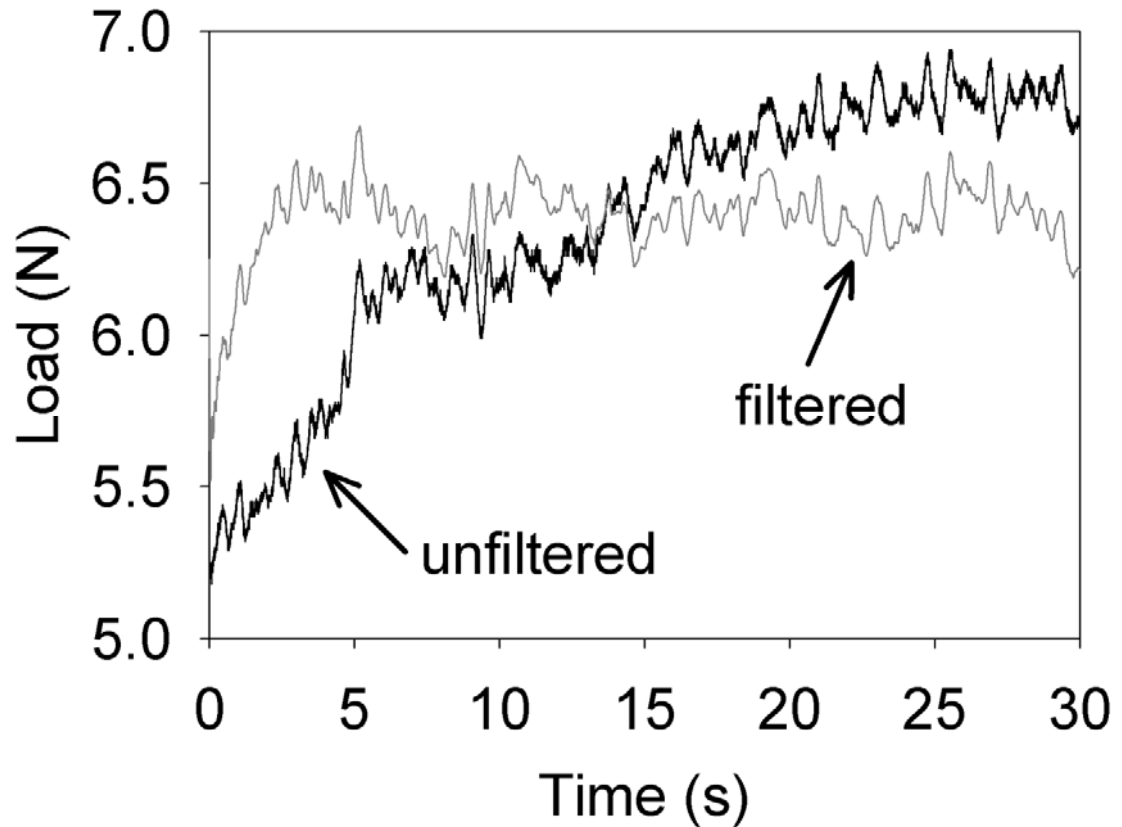
Figure 2.3. Effects of band-pass filtering. The dark black line represents raw plunger extrusion force vs. time for a 200 cycle-mixed gel through a tip of 0.25 mm diameter at a constant plunger displacement rate of 0.25 mm/s. The 1 degree draft tapering within the syringes causes the mean running-average-load to monotonically increase. The dark grey line represents the band-pass-filtered load, where frequency components below 0.5 Hz and above 40 Hz were removed (to account for the draft and plunger-on-syringe friction). While transient effects are still present during the first ~5 seconds of the filtered load resulting from the ramp-up of the test-frame, the load reaches a steady state in which the running-average-load no longer monotonically increases.

Statistically significant differences were analyzed using a 1-way ANOVA, post-hoc Tukey test, with a p-value of 0.05.

Geometric Fidelity Characterization

Geometric fidelity was qualitatively characterized by visually inspecting constructs printed on the Fab@Home SFF system. CAD models of various

geometries were converted into STL files and loaded into the Fab@Home control
software, including high-aspect ratio cylinders, cubes, disks and an ovine meniscus
from CT imaging. The software subsequently planned the tool paths and afterwards,
non-cell-seeded alginate gel was mixed between 8 and 200 times, loaded into syringes
and placed in the deposition tool. The gel preparation and prints were conducted
according to the protocol described above.

Photographs of the printed constructs were captured for subsequent
comparison between samples of different test groups. Key characteristics emphasized
during observation included surface texture, similarity of the overall shape compared
to the intended geometry, and presence of point defects such as missing material.

Elastic Modulus Characterization

Using the hydrogel fabrication protocol described above, non-cell-seeded
alginate hydrogel was mixed between 8 and 200 times, and subsequently cast between
glass plates using 1 mm spacer plates. Disks were stamped out with a 6 mm diameter
biopsy punch, post-crosslinked for 20 minutes in 2% $CaCl_2$ and stored for no more
than 1 hour in HEPES buffer. The disks were then placed in an ELF 3200
(EnduraTec, Minnetonka, MN) mechanical test-frame in a confined compression
chamber to assess equilibrium modulus as described previously[29]. A 1000 g load cell
(Sensotec, Columbus, OH) was attached to the bottom plate and a displacement sensor
to the top plate. The bottom plate was filled with PBS in order to completely
encompass the sample with fluid. The two plates started at a distance corresponding to
0% strain and stepped 0.1 mm towards each other every 100 s until 45% strain was
achieved. Load data were acquired at a frequency of 5 Hz, and displacement and load
data were converted to strain and stress respectively by normalizing to sample
thickness and area. The stress-strain curve of each printed sample was analyzed by

51

first finding the equilibrium stress corresponding to each imposed strain (0–45%). The linear region of the equilibrium stress-strain curve was fit linearly; the slope of this line was the Young's modulus of the sample.

Statistically significant differences were analyzed using a 1-way ANOVA, post-hoc Tukey test, with a p-value of 0.05.

Viability Test

Viability of the cells suspended in the alginate gel was measured immediately after the printing process. Disks, 6 mm in diameter ✕ 2 mm in height, were printed on the Fab@Home using the same gel preparation and printing protocol described above. Gels were mixed between 8 and 200 times. In addition to the standard syringe tip diameter of 0.25 mm, diameters of 0.61 mm and 5 mm were also used during viability experimentation. Also, in addition to the standard duration of 15 minutes between mixing and printing, 30 minute and 45 minute curing periods were also tested with a 0.25 mm diameter tip. Each sample was tested with the Live/Dead Viability Assay (Molecular Probes, Eugene, OR). The samples were exposed to 0.15 μM calcein AM and 2μM ethidium homodimer-1 (EthD-1) for 60 minutes at room temperature. The stained samples were analyzed under a Nikon TE2000-S microscope equipped with an epiflourescence attachment and a Spot RT digital camera. The viability was calculated as the average of the ratios of live over total cells in a hemacytometer (Hausser Scientific, Horsham, PA), normalized by the initial cell viability.

Statistically significant differences were analyzed using a 2-way ANOVA, post-hoc Tukey test, with a p-value of 0.05. All data are presented as mean ± standard error of the mean.

Effects of Mixing Amount on Gel Homogeneity

      Gels that were prepared with greater mixing of the alginate and crosslinker prior to printing exhibited much less temporal variation in plunger extrusion force. That is, for samples that were highly mixed, the max-to-min variation in extrusion force was smaller than for those samples that were mixed fewer times (Figure 2.4). Gels that were mixed 8 times exhibited a range in load of ~1.5 N, whereas gels mixed 200 times only exhibited a range of ~0.5 N.
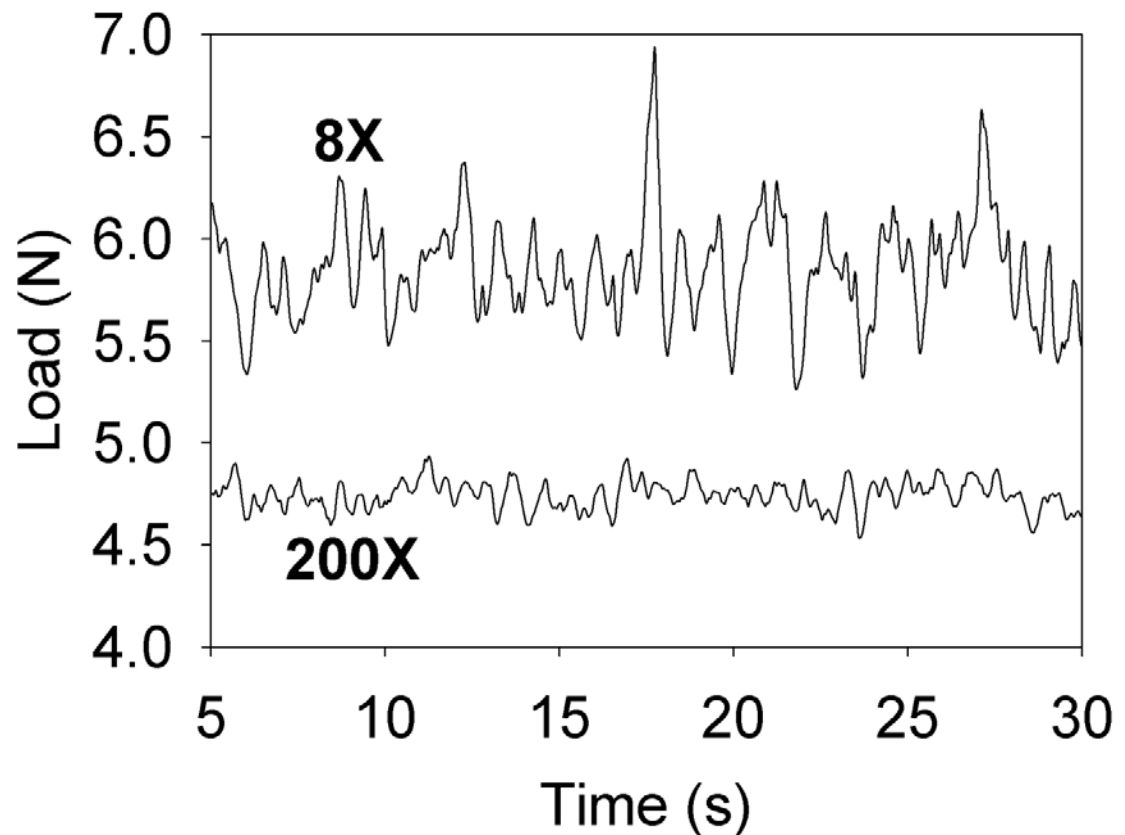
Figure 2.4. Heterogeneity of gel reflected in temporal load. The two lines represent band-pass-filtered temporal load, of which the first 5 seconds have been discarded to ignore transients resulting from test-frame ramp-up. The 200 cycle-mixed gel exhibits much narrower temporal variation in load, with a range of ~0.5 N, whereas the 8 cycled-mixed gel exhibits a range of ~1.5 N.
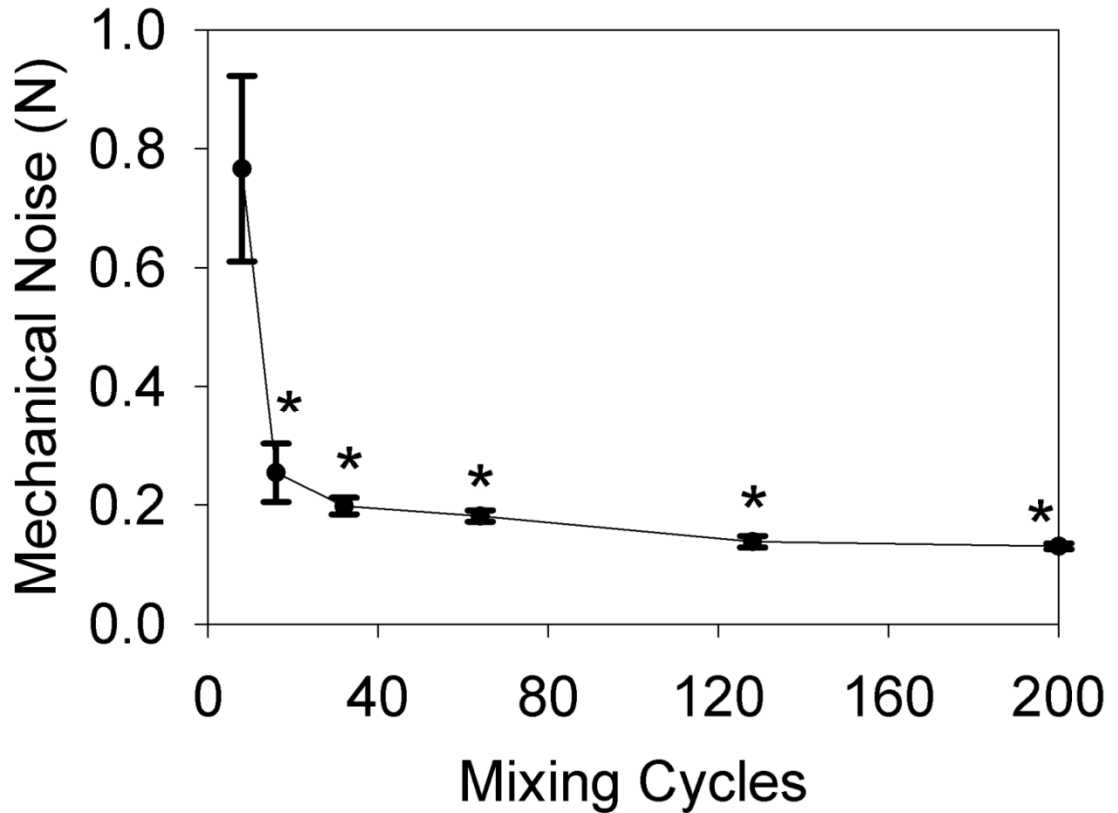
Figure 2.5. Mechanical noise vs. number of mixing cycles. As the number of mixing cycles between the alginate and crosslinker increases from 8 cycles to 200 cycles, the associated mechanical noise monotonically decreases. At 8 mixing cycles, the mechanical noise is 0.77±0.16 N, and as the mixing cycles increases to 120 cycles, the mechanical noise drops by 82% to 0.14±0.01 N. Note: Error bars represent the standard error of the mean and n = 10; "*" denotes $p < 0.05$ vs. 8 mixings.

The effect of mixing amount on gel homogeneity was also apparent when expressed in terms of "mechanical noise," or the standard deviation of the plunger extrusion force over time (Figure 2.5). For samples mixed 8 times, the mechanical noise was 0.77±0.16 N (n = 10). The mechanical noise drastically dropped to 0.25±0.05 N at 16 mixings ($p < 0.05$) and continued to drop to 0.14±0.01 N at 128 mixings (n = 10). In the low-mixing regime, merely increasing the mixing by 8 cycles yielded a 68% reduction in mechanical noise. The additional mixing cycles between

16 and 128 mixings, yielded an additional 44% reduction in mechanical noise. Overall, mixing 128 times instead of 8 times yields an 82% decrease in mechanical noise ($p<0.05$).

Effects of Mixing Amount on Geometric Fidelity of Printed Constructs

Geometric fidelity was qualitatively assessed in terms of surface texture, similarity to target geometry and point defects. Samples that were printed with gels mixed 200 times exhibited much smoother surfaces than those mixed only 8 times. Furthermore, the 200× samples exhibited closer similarity to the target geometry and fewer point defects, such as locations with missing material or too much material.

The higher geometric fidelity of 200× printed gels, as compared to 8× gels, was particularly evident in the print of the ovine meniscus from CT imaging (Figure 2.6). The surface texture of the 8× sample was rougher and clearly displayed the laminar nature of the layer-wise manufactured construct. However, the 200× sample had a smooth surface and the individual layers were visually imperceptible.

Furthermore, the 200× samples better matched the intended geometry particularly at the horns of the meniscus and alone the top rim of the construct. As for point defects, the 8× sample exhibited numerous cavities of missing material as well as mounds of gel that are nonexistent in the target geometry.

Not only was within-print geometric fidelity higher for 200× gels, but the print-to-print variability was much smaller (Figure 2.6). The 200× gels yielded constructs that were consistently smooth, defect free, and similar to the target geometry. However, the geometric fidelity of 8× gels greatly varied from print-to-print, sometimes yielding prints of moderate geometric fidelity but other times yielding very poor geometric fidelity.
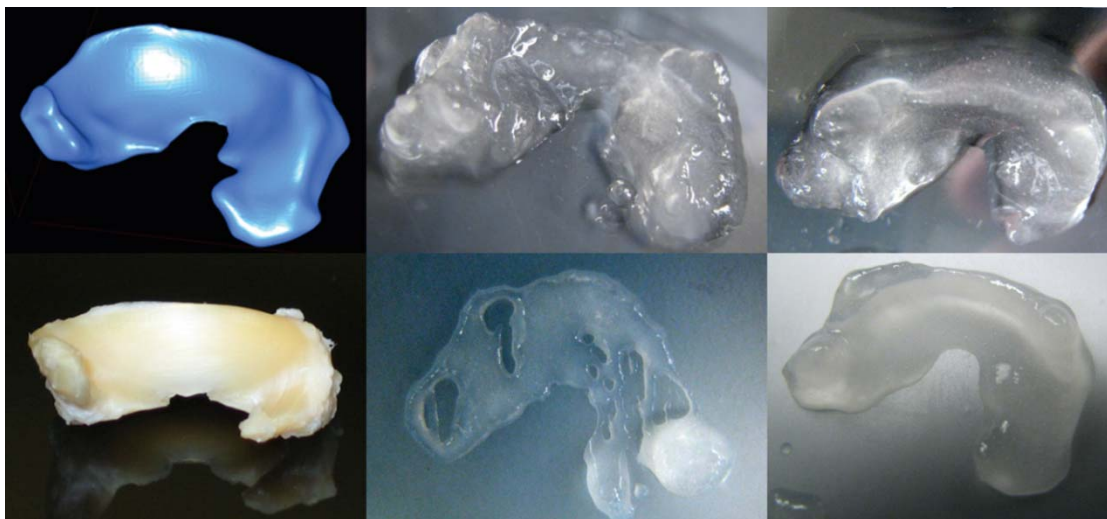
Figure 2.6. Geometric fidelity of printed ovine menisci vs. number of mixing cycles. An ovine meniscus (bottom-left) was imaged using a CT scanner (top-left) and printed. The print with the 8 cycle-mixed gel (top-middle) exhibited a rough surface texture, presence of point defects including cavities, and deviation from target geometry along the upper rim. The print with the 200× gel (top-right) exhibited a smoother surface texture, better matching of the target geometry and fewer point defects. Also, print-to-print variability was poorer with the 8× gel, sometimes resulting in complete failures (bottom-middle), whereas the 200× gel produced more consistent results (bottom-right).

Effects of Mixing Amount on Elastic Modulus of Printing Gel

The compressive modulus of hydrogel disks increased monotonically with mixing (Figure 2.7). At 30 mixings, the post-crosslinked printed disks possessed an elastic modulus of 4.0 ± 0.1 kPa (n = 5). The elastic modulus increased to 5.9 ± 0.3 kPa and 8.4 ± 1.0 kPa, at 120 and 200 mixing cycles, respectively (n = 5). The 4-fold increase in mixing between 30 and 120 cycles, yielded a 50% increase in elastic modulus ($p<0.05$). Overall, mixing the gel 200 times versus only 30 times yielded a 110% increase in elastic modulus ($p<0.05$).
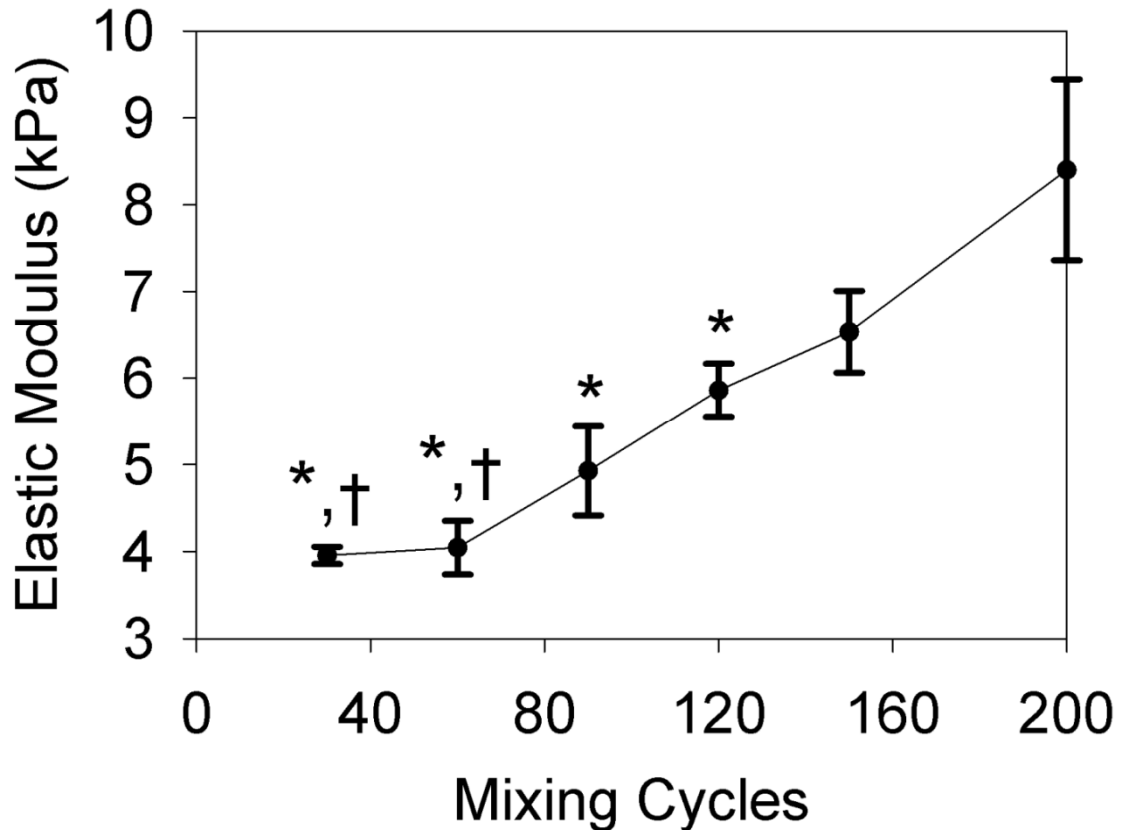
Figure 2.7. Elastic modulus vs. number of mixing cycles. As the number of mixing cycles between the alginate and crosslinker increases, from 30 cycles to 200 cycles, the associated elastic modulus monotonically increases. At 30 mixing cycles, the mechanical noise is 4.0±0.1 N and as the mixing cycles increases to 200 cycles, the mechanical noise increases by 110% to 8.4±1.0 N. Note: Error bars represent the standard error of the mean and n = 5; "*" denotes $p<0.05$ vs. 200 mixings and "†" denotes $p<0.05$ vs. 150 mixings.

Effects of Mixing Amount on Viability of Printed Constructs

The first viability experiment tested the effect of tip diameter, from 0.25 mm to 5 mm, on viability with samples that were printed 15 minutes after mixing under various mixing techniques, including 8×, 64× and 200×. While the viabilities ranged from 65% to 77%, it did not do so as a function of tip diameter or number of mixing cycles (Figure 2.8).
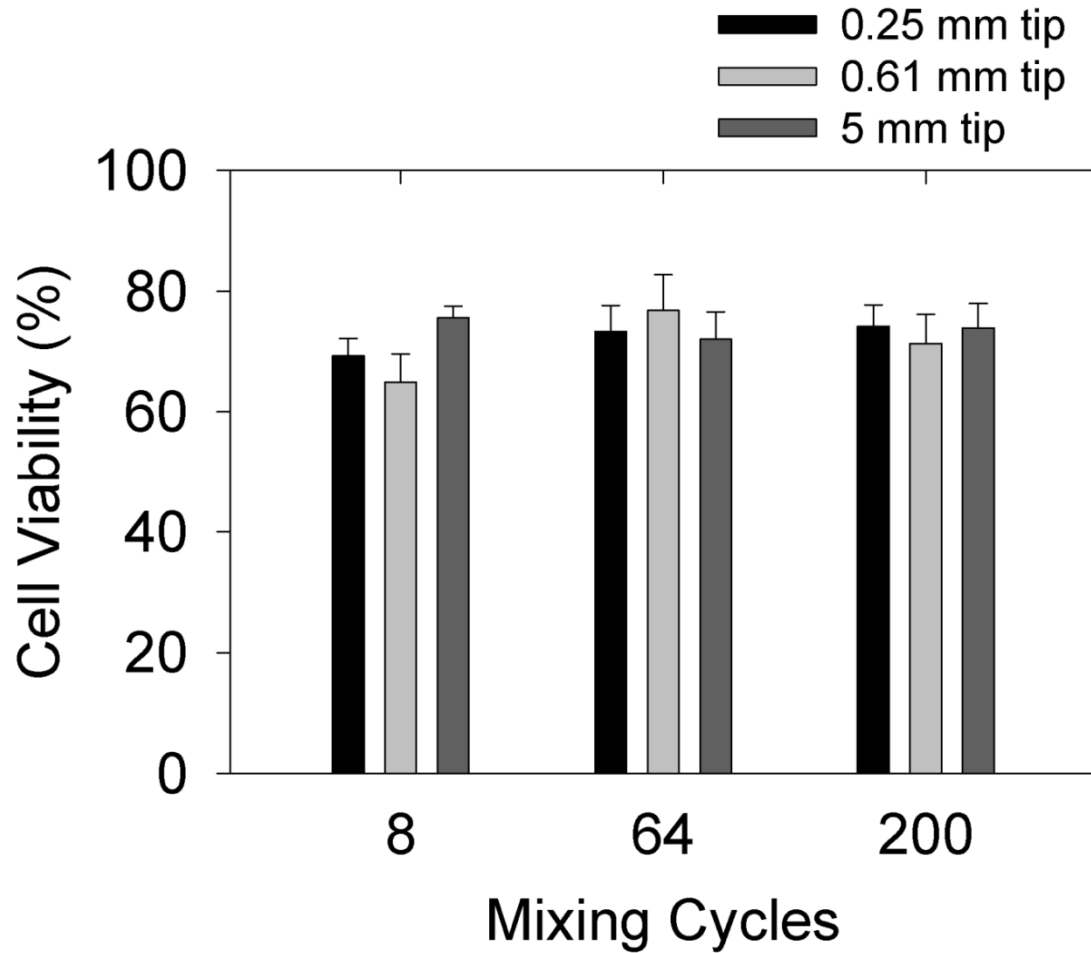
Figure 2.8. Cell viability vs. deposition tip diameter and number of mixing cycles. The size of the deposition tip, within the range of 0.25 mm to 5 mm, does not have effect on the viability of printed cells. Note: Error bars represent the standard error of the mean and n = 10.

The second viability experiment tested the effect of cure time (i.e. the time between mixing and printing) on viability. For gels printed through a 0.25 mm diameter tip, 8× and 200× gels did not have different viabilities with cure times of 15 minutes nor of 30 minutes. However, with a cure time of 45 minutes, the viability increased (p<0.05) for 200× gels compared to 8× gels (Figure 2.9). With a 45 minute cure time, printed 8× gels only had a viability of 64.5+5.1%. However, printed 200× gels had a 34% higher viability, 87.1+2.4%.
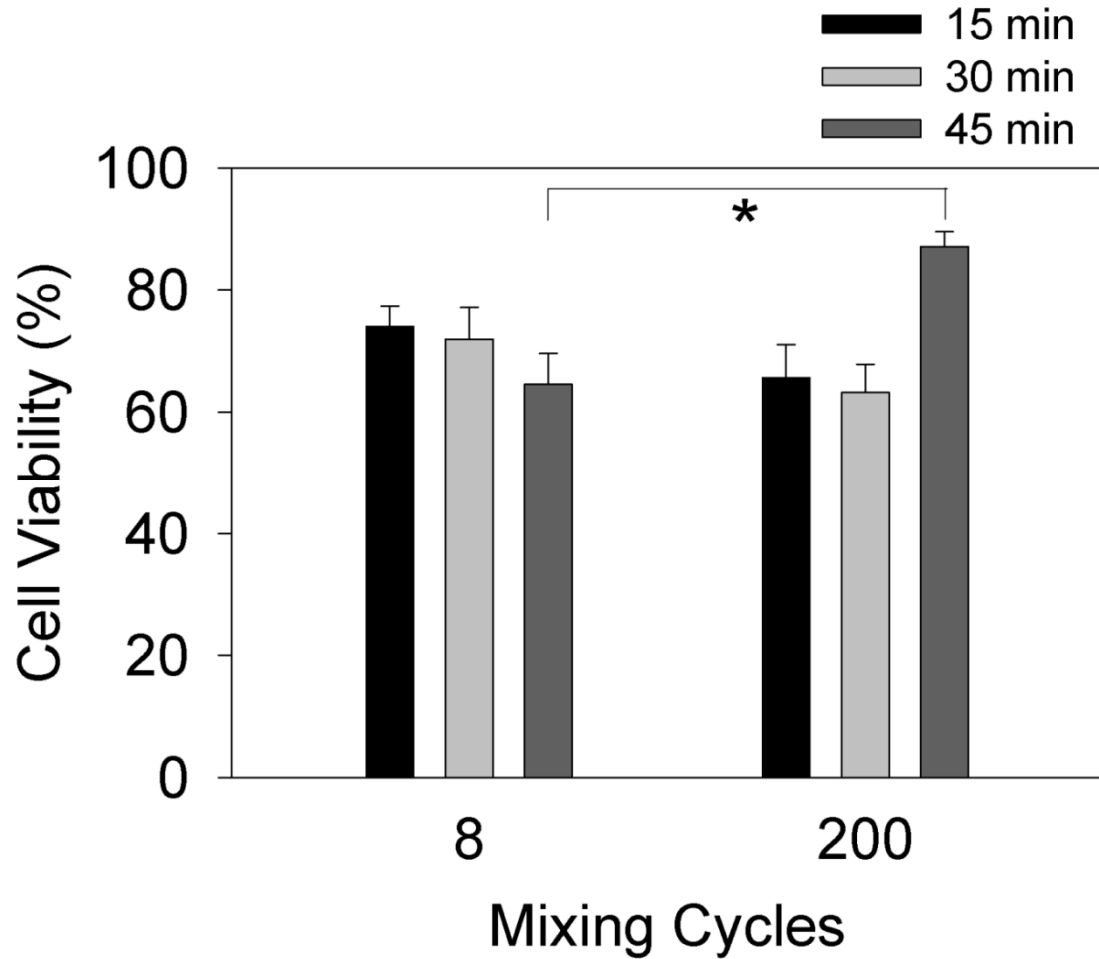
Figure 2.9. Cell viability vs. time between mixing and printing, and number of mixing cycles. Viability does not significantly vary with mixing at cure times of 15 or 30 minutes. However, with a cure time of 45 minutes, the viability increases by 34% from 64.5+5.1% in an 8× gel to 87.1+2.4% in a 200× gel. Note: Error bars represent the standard error of the mean and n = 10; "*" denotes p<0.05.

DISCUSSION

This study is one of the first to present a method for assessing the printing characteristics, in particular the homogeneity, of tissue printing inks. A mechanical test-frame was used to capture load data during extrusion of alginate hydrogel through a deposition nozzle. The load data was filtered to remove friction effects unrelated to the hydrogel, and the standard deviation of the temporal syringe extrusion force was

taken as the "mechanical noise" of the gel. Standard material characterization techniques, such as measurement of elastic modulus and viscosity, do not serve as good indicators of how a gel will behave during printing. These test methods fail to accurately describe a gel's "printability" due to the printing technique's extreme sensitivity to heterogeneity of the printing ink. Due to the rapid kinetics of gelation when calcium is mixed with alginate, these hydrogels are highly susceptible to localized variation in material properties, such as viscosity. As portions of varying stiffness are pushed through the deposition tool at constant displacement rates, these variations in gel properties lead to inconsistent flow rates which adversely affects the geometric fidelity of printed parts; in extreme cases, the printer will completely clog as high-viscosity clumps attempt to pass through the deposition tool.

Unlike traditional material characterization methods, the technique presented herein not only describes the homogeneity of printing inks, but does so directly in a 3D printing context. That is, gel homogeneity was measured within the same types of wetted components (i.e., syringes and syringe tips) that are used in 3D printers and the forces imposed on the syringes mimic those during an actual print. This measurement within a 3D printing context enhances the usefulness of the results obtained because the test conditions so closely match those of the end-use; consequently, the methodology is highly relevant for characterizing positive displacement extrusion of hydrogels[14,15,21], as well as non-hydrogel bio-materials[30,31]. This characterization methodology is also applicable to characterization of bio-printing inks for pressure deposition[13,17,18,23-26,32-36] and rotary screw extrusion[37-39] techniques, even though the printing apparatus' configurations are not identical to the experimental setup.

Once we devised a method for quantitatively describing the homogeneity of printing inks, the effect of mixing on homogeneity was one of the most pertinent process parameters that needed to be better understood. The 3D printing of alginate

evolved from injection molding of the material. Established hydrogel injection molding protocol prescribes 4-8 mixings between the calcium and alginate prior to injection[5-11]. Mixing beyond 4-8 cycles was assumed to be unnecessary and potentially detrimental to cell viability and mechanical integrity, due to excess shearing of the gel. As the alginate hydrogel formulation was modified for 3D printing, mixing was never addressed due to the lack of relevant characterization methods. While some anecdotal evidence suggested that increased mixing potentially improved the geometric fidelity of printed parts, it was unclear if this was related to material homogeneity, and furthermore, it was unknown whether mixing adversely affected cell viability and construct strength.

In fact, mixing has a profound effect on the homogeneity of alginate gel during printing. Mixing 16 cycles versus the established 8-cycle norm yielded a 68% decrease in mechanical noise. Furthermore, mixing 128 cycles versus 8 cycles delivers an 82% reduction in mechanical noise. Such high mixing cycles were completely at odds with the established injection molding protocol[5-11], which considered 128 or even 16 mixing cycles entirely unnecessary and detrimental to the viability and mechanical integrity of resultant constructs.

Increased mixing of the alginate and calcium crosslinker enhanced gel homogeneity due to the more thorough redistribution of the calcium ions. As the gel is further mixed, the additional mixing energy more evenly distributed the calcium ions throughout the calcium-alginate mixture. With more even calcium ion distribution, the local concentration of calcium is more uniform and the resultant stiffness of the gel is likewise more consistent. In poorly mixed gels, uneven calcium ion concentration leads to localized pockets of under- and over-crosslinked gel which result in varying flow rates when a constant displacement rate is imposed on the syringe plunger.

We next needed to determine whether the improved homogeneity of the alginate gel translated to improvements in geometric fidelity of printed constructs. Prints conducted with 200× gels indeed exhibited smoothers surfaces, less perceptible layering, closer matching to target geometry, and fewer point defects than prints conducted with 8× gels. Furthermore, 200× gels yielded better print-to-print reliability in terms of geometric fidelity. That is, 200× gels consistently produced constructs of high geometric fidelity whereas 8× gels resulted in a much wider range of geometric fidelities, varying from moderate to very poor.

Increased mixing improved geometric fidelity likely because the greater homogeneity led to more consistent deposition flow rates. The geometric fidelity of printed constructs is highly sensitive to the uniformity of the deposition material flow. Since the deposition tool traverses without feedback on the material flow, even slight changes in the material flow rate load to cavities if the flow rate is too low or mounds if the rate is too high. In extreme cases, the gel heterogeneity leads to very stiff clumps of gel attempting to pass through the deposition tool, in which case the tool completely clogs and deposition halts entirely.

Even though we demonstrated the gel homogeneity and geometric fidelity benefits of increased mixing, we still needed to address the concerns that such mixing would adversely affect viability and mechanical integrity. While mechanical properties[40] and viability[41,42] of printed hydrogel constructs have been studied, they have never been analyzed as a function of mixing technique and gel homogeneity. We employed elastic modulus mechanical testing and the Live/Dead assay to investigate the effects of increased mixing to rule out potential adverse effects.

One concern was that mixing beyond 4-8 cycles would degrade the mechanical integrity of the resultant gel because as the gel mixes it transitions into a solid, and further mixing would permanent rip the material. Our testing demonstrated that rather

than degrading mechanical integrity, increased mixing actually increased the final elastic modulus two-fold. Mixing 120 times instead of 30 times increased the final elastic modulus 50% to 5.9 kPa. Increasing the mixing from 30 cycles to 200 cycles, yields a 110% increase in the final elastic modulus of the printed constructs, resulting in a modulus of 8.4 kPa. Interestingly, although we were initially concerned about detrimental shearing of the gel through increased mixing, we did not observe such effects and instead actually saw enhanced mechanical integrity resulting from increased mixing. Several hypotheses potentially explain why increased mixing improved mechanical integrity. Firstly, better distribution of the calcium ions initially as the gel was mixed may have made the ions more readily available for crosslinking through the constructs resulting in more efficient use of the ions. Secondly, better distribution of the calcium may have eliminated pockets of extremely over-crosslinked gel which upon deposition would have been torn apart by the restricted orifice of the deposition tool to the detriment of the overall mechanical integrity. Thirdly, by eliminating these localized pockets of over-crosslinked gel, the gel may have exhibited more consistent diffusivity which further allowed for efficient transport and use of calcium ions, as well as allowed for polymer chain realignment.

Besides mechanical integrity being preserved, we also found that viability of the cells within printed constructs was maintained even with increased mixing. Not only was cell viability preserved over a range of syringe tip diameters, but when a print was conducted 45 minutes after mixing, the viability of 200× gels was actually statistically significantly higher than for 8× gels. We believe that as mixing is increased, the gel becomes more homogenous and localized clumps of over-crosslinked gel are eliminated. These clumps, present in less mixed samples, exert high shear stress on the cells when forced through the nozzle and consequently decrease sample viability. We also believe this effect is only noticeable with a curing

time of 45 minutes, and not with lesser curing times, because the overall viscosity of the gel is too low in lesser cured samples for the clumps to exert shear stresses above the critical threshold.

Upon close consideration of the differences between alginate injection molding and alginate printing, we can begin to reconcile the established injection molding protocol with the findings of this paper. With injection molding, the gel is mixed 4-8 times and immediately shot into the mold[5-11]. After injection, the localized variation of material properties would be unobservable because it is concealed within a mold and unperturbed. However, in printing, local variation in material properties is much more noticeable because small portions are extruded serially from a nozzle, effectively displaying local material properties parcel-by-parcel. Furthermore, the time scales are different between the two techniques. With molding, the gel is evacuated from the syringe seconds after mixing, whereas with printing the gel leaves the deposition tool up to 45 minutes after mixing. Heterogeneity is far less pronounced seconds after mixing since it is still a relatively low-viscosity liquid, whereas with printing, the sol-gel transition enacts and such heterogeneities are much more perceptible. Simply put, the molding technique does not readily allow for the observation that 4-8 mixings produces heterogeneous gels.

This study not only provides greater insight the effects of mixing on alginate hydrogel properties, but it also fundamentally changes key process parameters that drastically improve the efficacy of hydrogel 3D printing. Instead of relying upon prior established guidelines of 4-8 mixings[5-11], we suggest a radical shift to a mixing regime of 128-200 mixings. We also have proven that such a radical shift in technique does not come at the expense of mechanical properties or cell viability, and to the contrary, actually improves both aspects. In addition to improving alginate hydrogel 3D printing, we also provide a test methodology that enables the characterization all

hydrogels[12-26], as well as other types of biologically relevant printing inks[30-39]. The test methodology is directly applicable to positive displacement-based printing techniques, but is also useful for characterizing pressure-based[13,17,18,23-26,32-36] and rotary screw-based[37-39] printing approaches. As tissue 3D printing moves closer toward the clinic, we will need to address concerns about reliability, and methodologies such as the one presented herein are crucial for optimizing printing inks and ensuring acceptable levels of reproducibility.

REFERENCES

[1]   B. Beekman, N. Verzijl, R. A. Bank, K. v. d. Mark, and J. M. TeKoppele, "Synthesis of collagen by bovine chondrocytes cultured in alginate: posttranslational modifications and cell-matrix interaction," *Experimental Cell Research,* vol. 237, pp. 135-141, 1997.

[2]   B. O. Enobakhare, D. L. Bader, and D. A. Lee, "Quantification of sulfated glycosaminoglycans in chondrocyte/alginate cultures, by use of 1,9-dimethylmethylene blue," *Analytical Biochemistry,* vol. 243, pp. 189-191, 1996.

[3]   K. T. Paige, L. G. Cima, M. J. Yaremchuk, B. L. Schloo, J. P. Vacanti, and C. A. Vacanti, "De novo cartilage generation using calcium alginate-chondrocyte constructs," *Plastic and Reconstructive Surgery,* vol. 97, pp. 168-180, 1996.

[4]   K. T. Paige, L. G. Cima, M. J. Yaremchuk, J. P. Vacanti, and C. A. Vacanti, "Injectable cartilage," *Plastic and Reconstructive Surgery,* vol. 96, pp. 1390-1400, 1995.

[5]   J. J. Ballyns, D. L. Cohen, E. Malone, S. A. Maher, H. G. Potter, T. M. Wright, H. Lipson, and L. J. Bonassar, "An optical method for evaluation of geometric fidelity for anatomically shaped tissue engineered constructs," *Tissue Engineering Part C: Methods,* accepted.

[6]   J. J. Ballyns, J. P. Gleghorn, V. Niebrzydowski, J. J. Rawlinson, H. G. Potter, S. A. Maher, T. M. Wright, and L. J. Bonassar, "Image-guided tissue engineering of anatomically shaped implants via MRI and Micro-CT using injection molding," *Tissue Engineering Part A,* vol. 14, pp. 1195-1202, 2008.

[7]   S. C. Chang, J. A. Rowley, G. Tobias, N. G. Genes, A. K. Roy, D. J. Mooney, C. A. Vacanti, and L. J. Bonassar, "Injection molding of chondrocyte/alginate constructs in the shape of facial implants," *Journal of Biomedical Materials Research,* vol. 55, pp. 503-511, 2001.

[8]   S. C. Chang, G. Tobias, A. K. Roy, C. A. Vacanti, and L. J. Bonassar, "Tissue engineering of autologous cartilage for craniofacial reconstruction by injection molding," *Plastic and Reconstructive Surgery,* vol. 112, pp. 793-799, 2003.

[9]   M. E. Hott, C. A. Megerian, R. Beane, and L. J. Bonassar, "Fabrication of tissue engineered tympanic membrane patches using computer-aided design and injection molding," *The Laryngoscope,* vol. 114, pp. 1290-1295, 2004.

[10]   C. K. Kuo and P. X. Ma, "Maintaining dimensions and mechanical properties of ionically crosslinked alginate hydrogel scaffolds in vitro," *Journal of Biomedical Materials Research Part A,* vol. 84, pp. 899-907, 2008.

[11]   J.-W. Xu, V. Zaporojan, G. M. Peretti, R. E. Roses, K. R. Morse, A. K. Roy, J. M. Mesa, M. A. Randolph, L. J. Bonassar, and M. J. Yaremchuk, "Injectable tissue-engineered cartilage with different chondrocyte sources," *Plastic and Reconstructive Surgery,* vol. 113, pp. 1361-1371, 2004.

[12]   D. R. Albrecht, V. L. Tsang, R. L. Sah, and S. N. Bhatia, "Photo- and electropatterning of hydrogel-encapsulated living cell arrays," *Lab On a Chip,* vol. 5, pp. 111-118, 2004.

[13]   T. H. Ang, F. S. A. Sultana, D. W. Hutmacher, Y. S. Wong, J. Y. H. Fuh, X. M. Mo, H. T. Loh, E. Burdet, and S. H. Teoh, "Fabrication of 3D chitosan-hydroxyapatite scaffolds using a robotic dispensing system," *Materials Science and Engineering Part C,* vol. 20, pp. 35-42, 2002.

[14]   D. L. Cohen, E. Malone, H. Lipson, and L. J. Bonassar, "Direct freeform fabrication of seeded hydrogels in arbitrary geometries," *Tissue Engineering,* vol. 12, pp. 1325-1335, 2006.

[15]   L. Geng, W. Feng, D. W. Hutmacher, Y. S. Wong, H. T. Loh, and J. Y. Fuh, "Direct writing of chitosan scaffolds using a robotic system," *Rapid Prototyping Journal,* vol. 11, pp. 90-97, 2005.

[16]   S. Khalil and W. Sun, "Bioprinting endothelial cells with alginate for 3D tissue constructs," *Journal of Biomechanical Engineering,* vol. 131, pp. 1002-1008, 2009.

[17]   R. Landers, U. Hübner, R. Schmelzeisen, and R. Mülhaupt, "Rapid prototyping of scaffolds derived from thermoreversible hydrogels and tailored for applications in tissue engineering," *Biomaterials,* vol. 23, pp. 4437-4447, 2002.

[18]   R. Landers, A. Pfister, U. Hübner, H. John, R. Schmelzeisen, and R. Mülhaupt, "Fabrication of soft tissue engineering scaffolds by means of rapid prototyping techniques," *Journal of Materials Science,* vol. 37, pp. 3107-3116, 2002.

[19]   Y. Lu, G. Mapili, G. Suhali, S. Chen, and K. Roy, "A digital micro-mirror device-based system for the microfabrication of complex, spatially patterned tissue engineering scaffolds.," *Journal of Biomedical Materials Research Part A,* vol. 77, pp. 396-405, 2006.

[20]   V. Mironov, T. Boland, T. Trusk, G. Forgacs, and R. R. Markwald, "Organ printing: computer-aided jet-based 3D tissue engineering," *Trends in Biotechnology,* vol. 21, pp. 157-161, 2003.

[21]   C. M. Smith, A. L. Stone, R. L. Parkhill, R. L. Stewart, M. W. Simpkins, A. M. Kachurin, W. L. Warren, and S. K. Williams, "Three-dimensional

BioAssembly tool for generating viable tissue-engineered constructs," *Tissue Engineering,* vol. 10, pp. 1566-1576, 2004.

[22] V. L. Tsang and S. N. Bhatia, "Three-dimensional tissue fabrication," *Advanced Drug Delivery Reviews,* vol. 56, pp. 1635-1647, 2004.

[23] X. Wang, Y. Yan, Y. Pan, Z. Xiong, H. Liu, J. Cheng, L. Feng, L. Feng, R. Wu, R. Zhang, and Q. Lu, "Generation of three-dimensional hepatocyte/gelatin structures with rapid prototyping system," *Tissue Engineering,* vol. 12, pp. 83-90, 2006.

[24] X. Wei, W. Xiaohong, Y. Yongnian, Z. Wei, X. Zhuo, L. Feng, W. Rendong, and Z. Renji, "Rapid prototyping three-dimensional cell/gelatin/fibrinogen constructs for medical regeneration," *Journal of Bioactive and Compatible Polymers,* vol. 22, pp. 363-377, 2007.

[25] Y. Yan, X. Wang, Y. Pan, H. Liu, J. Cheng, Z. Xiong, F. Lin, R. Wu, R. Zhang, and Q. Lu, "Fabrication of viable tissue-engineered constructs with 3D cell-assembly technique," *Biomaterials,* vol. 26, pp. 5864-5871, 2005.

[26] Y. Yan, X. Wang, Z. Xiong, H. Liu, F. Liu, F. Lin, R. Wu, R. Zhang, and Q. Lu, "Direct construction of a three-dimensional structure with cells and hydrogel," *Journal of Bioactive and Compatible Polymers,* vol. 20, pp. 259-269, 2005.

[27] J. P. Gleghorn, A. R. Jones, C. R. Flannery, and L. J. Bonassar, "Boundary mode frictional properties of engineered cartilaginous tissues," *European Cells and Materials,* vol. 14, pp. 20-29, 2007.

[28] E. Malone and H. Lipson, "Fab@Home: the personal desktop fabricator kit," *Rapid Prototyping Journal,* vol. 13, pp. 245-255, 2007.

[29] N. G. Genes, J. A. Rowley, D. J. Mooney, and L. J. Bonassar, "Effect of substrate mechanics on chondrocyte adhesion," *Archives of Biochemistry and Biophysics,* vol. 422, pp. 161-167, 2004.

[30] M. Endres, D. W. Hutmacher, A. J. Salgado, C. Kaps, J. Ringe, R. L. Reis, M. Sittinger, A. Brandwood, and J. T. Schantz, "Osteogenic induction of human bone marrow-derived mesenchymal progenitor cells in novel synthetic polymer-hydrogel matrices," *Tissue Engineering,* vol. 9, pp. 689-702, 2003.

[31] B. Xie, R. L. Parkhill, W. L. Warren, and J. E. Smay, "Direct writing of three-dimensional polymer scaffolds using colloidal gels," *Advanced Functional Materials,* vol. 16, pp. 1685-1693, 2006.

[32] C. X. F. Lam, X. M. Mo, S. H. Teoh, and D. W. Hutmacher, "Scaffold development using 3D printing with a starch-based polymer," *Materials Science and Engineering Part C,* vol. 20, pp. 49-56, 2002.

[33] L. Rüdiger and M. Rolf, "Desktop manufacturing of complex objects, prototypes and biomedical scaffolds by means of computer-assisted design combined with computer-guided 3D plotting of polymers and reactive oligomers," *Macromolecular Materials and Engineering,* vol. 282, pp. 17-21, 2000.

[34] G. Vozzi, C. Flaim, A. Ahluwalia, and S. Bhatia, "Fabrication of PLGA scaffolds using soft lithography and microsyringe deposition," *Biomaterials,* vol. 24, pp. 2533-2540, 2003.

[35] G. Vozzi, A. Previti, D. De Rossi, and A. Ahluwalia, "Microsyringe-based deposition of two-dimensional and three-dimensional polymer scaffolds with a well-defined geometry for application to tissue engineering," *Tissue Engineering,* vol. 8, pp. 1089-1098, 2002.

[36] C. Weinand, I. Pomerantseva, C. M. Neville, R. Gupta, E. Weinberg, I. Madisch, F. Shapiro, H. Abukawa, M. J. Troulis, and J. P. Vacanti, "Hydrogel-[beta]-TCP scaffolds and stem cells for tissue engineering bone," *Bone,* vol. 38, pp. 555-563, 2006.

[37] L. Shor, S. Guceri, M. Gandhi, X. Wen, and W. Sun, "Solid freeform fabrication of polycaprolactone/hydroxyapatite tissue scaffolds," *Journal of Manufacturing Science and Engineering,* vol. 130, pp. 210-218, 2008.

[38] F. Wang, L. Shor, A. Darling, S. Khalil, W. Sun, S. Guceri, and A. Lau, "Precision extruding deposition and characterization of cellular poly-caprolactone tissue scaffolds," *Rapid Prototyping Journal,* vol. 10, pp. 42-49, 2004.

[39] Z. Xiong, Y. Yan, S. Wang, R. Zhang, and C. Zhang, "Fabrication of porous scaffolds for bone tissue engineering via low-temperature deposition," *Scripta Materialia,* vol. 46, pp. 771-776, 2002.

[40] K. Nair, K. Yan, and W. Sun, "A computational modeling approach for the characterization of mechanical properties of 3D alginate tissue scaffolds," *Journal of Applied Biomaterials and Biomechanics,* vol. 6, pp. 35-46, 2008.

[41] R. Chang, J. Nam, and W. Sun, "Effects of dispensing pressure and nozzle diameter on cell survival from solid freeform fabrication-based direct cell writing," *Tissue Engineering Part A,* vol. 14, pp. 41-48, 2008.

[42] M. Li, X. Tian, N. Zhu, D. J. Schreyer, and X. Chen, "Modeling process-induced cell damage in the biodispensing process," *Tissue Engineering Part C: Methods,* Accepted.

CHAPTER 3: GEOMETRIC FEEDBACK CONTROL OF DISCRETE-DEPOSITION SFF SYSTEMS[*]

INTRODUCTION

Solid freeform fabrication (SFF) is evolving to address new applications, such as in-situ manufacture[1] and the fabrication of fully functional components[2]. Along with these innovative applications come the technological challenges associated with a variety of process uncertainties, including "situational," "environmental," and "build-material" uncertainties (Figure 3.1). Existing control schemes attempt to harness closed-loop feedback control in order to achieve desirable geometric fidelity in the face of some process uncertainties[3]. However, these specific control schemes are limited in the types of uncertainties for which they can correct. Moreover, they are susceptible to changes or inaccuracies in the models that relate whole-part geometry to low-level process variables.

In this paper we propose a closed-loop feedback control scheme, which we call Greedy Geometric Feedback (GGF) control. Unlike other schemes which indirectly control part-geometry by monitoring and manipulating low-level system parameters (e.g., build-material flow rate, temperature, head position), GGF directly monitors whole-part geometry and directly manipulates the location of deposited matter to compensate for geometric inaccuracies. We suggest that "closing the loop" at the whole-part geometry level, rather than at the process-variable level, increases the extent to which process uncertainties can be detected and corrected, and thus allows for the compensation of a wider range of process uncertainties. We also suggest that this technique is more generalized in that it does not rely upon the knowledge of any specific relationships between whole-part geometry and low-level process variables.

[*] Daniel L. Cohen[1], Hod Lipson[1,2]; [1]Cornell University, Mechanical and Aerospace Engineering, Ithaca NY; [2]Cornell University, Computing and Information Science, Ithaca NY.
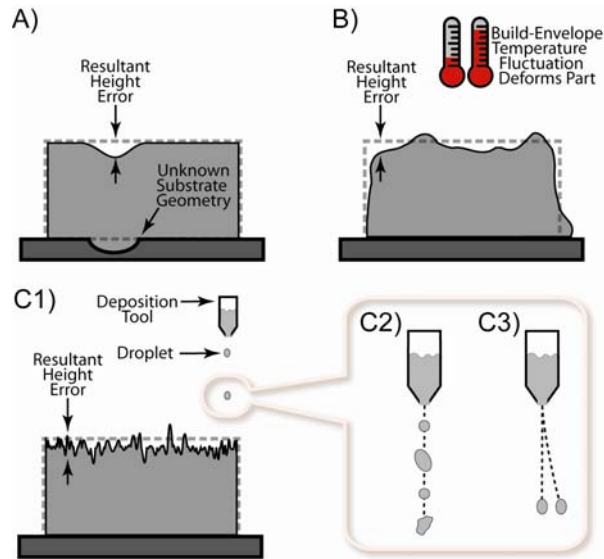
Figure 3.1. Three classes of process uncertainties relevant to printing depicted through cross-sections of printed parts (box-shaped dotted outlines signify intended geometries and shaded solid outlines represent actual printed objects). (a) An example of "situational uncertainty" in which an unknown substrate geometry causes a geometric defect in the printed part and results in a height error. (b) An example of "environmental uncertainty" in which build-envelope temperature fluctuation causes deformation via melting and results in height errors. (c1) An example of "build-material uncertainty" in which unstable material properties lead to (c2) varying droplet size/shape and (c3) varying droplet positioning, causing geometric defects and resulting in height errors.

PROBLEM STATEMENT

New applications of SFF, such as in-situ manufacture[4] and the fabrication of fully functional components[5], have inherent process uncertainties that can potentially diminish the geometric fidelity of the fabricated parts. Three classes of process uncertainties are especially relevant: 1) "situational," 2) "environmental," and 3) "build-material" uncertainties.

An application that exemplifies both "situational" and "environmental" process uncertainties is in-situ SFF. In the literature, the term "in-situ SFF" refers to Layered Manufacturing (LM) where the fabrication substrate has a complex or arbitrary geometry. For example, in-situ SFF could refer to LM on top of a pre-existing part[6] or

the use of LM to embed one component within another[7]. The uncertainty in substrate geometry during in-situ prints is one example of situational process uncertainty (Figure 3.1A).

Furthermore, if the pre-existing target substrate (e.g., external armor of a battle tank[8] or internal cavity of a human body[9]) is unable to be placed within a traditional SFF machine (e.g., due to large substrate size or sterility), then the SFF system must be capable of operating within the substrate's environment. While operating within the substrate's environment, the SFF system faces a less certain process parameter landscape, i.e., the SFF system is subject to substantial environmental process uncertainty. In-situ environmental conditions such as vibration, substrate movement, humidity variation, temperature fluctuation and substrate-on-part squeeze, are factors that could pose environmental process uncertainties and result in diminished geometric fidelity of the part (Figure 3.1B).

In addition to situational and environmental process uncertainties, a third class of process uncertainty is "build-material uncertainty." An application of SFF that demonstrates materials-based process uncertainty is the LM of fully functional components. While some functional components can be rapid prototyped with reasonable parametric certainty under open-loop control[10], other techniques face greater process uncertainty. Laser Metal Deposition (LMD) is an SFF technique with inherent process uncertainty that is used for producing functional metal components[3]. Also, syringe extrusion-based approaches to LM of fully functional electro-mechanical components are fraught with process uncertainty due to its materials' non-homogeneity, unfavorable viscosities and viscoelasticity[11]. Additionally, the hydrogels used in fabricating living, functional biological constructs are also particularly challenging to print[12]. This is due to materials-based phenomena such as background polymer cross-linking reactions, phase separation, non-homogenous

73

composition, low strength and viscoelastic behavior[9]. These non-traditional, functional SFF materials behave unpredictably and cause the fabricated components to have diminished geometric fidelity (Figure 3.1C).

While there are several classes of process uncertainties, and numerous examples of each, they will manifest themselves either at the process-variable level (e.g., droplet shape/position errors [Figure 3.1C]) or at the whole-part geometry level (e.g., during-print part-shape deformations [Figure 3.1B]). Ultimately, the result of these process uncertainties is some height error between the intended and the actual part geometries (Figure 3.1).

Open-loop control schemes are insufficient for some of the more innovative applications of SFF[13]. More advanced control schemes must be developed to achieve a desirable geometric fidelity despite under-constrained printing circumstances and/or inherently uncertain SFF processes and materials.

PRIOR WORK

Low-level closed-loop feedback control schemes have been implemented in many SFF systems to improve the geometric fidelities of printed parts. However, none of the approaches directly monitored the whole-part geometry. Instead, they monitored and manipulated low-level system variables such as machine temperature, material feedrate and individual droplet shape, anticipating that this would lead to better part-geometry.

Low-level, independent SFF process variables are commonly stabilized in both research and commercial RP systems using closed-loop feedback control. Process variables such as substrate position, envelope temperature, deposition tool temperature, laser power and material feedrate are often stabilized using closed-loop feedback control[14]. In these cases, a low-level independent variable is monitored and

directly actuated. For example, the envelope temperature is directly monitored with a temperature sensor and then directly manipulated with a heating element. However, these low-level independent process variables have only an indirect influence on the final part-geometry.

On a slightly higher level, dependent process variables have also been stabilized. For example, in LMD systems, melt pool depth was stabilized with a PID-controller by monitoring the melt pool profile, inferring the melt pool depth and then manipulating laser power and traverse speed[15]. However, these examples of dependent variable regulation are still low-level control schemes because whole-part geometry itself is not being directly monitored/manipulated; there is an indirect relationship between these dependent process variables and the whole-part geometry.

On yet a higher level of control, droplet geometry has been stabilized through closed-loop control. Geometric profiles of deposited beads were used to regulate the bead height through the manipulation of laser power[16]. Distributed-parameter modeling was used to generate real-time surface geometry models by identifying droplets' geometric parameters during-print[17]. This distributed-parameter model was used in conjunction with a PI-controller to regulate bead geometry through the manipulation of traverse speed and material feed rate[18]. Closed-loop feedback control has also been applied to non-LMD SFF systems. For example, computer vision feedback was used to regulate droplet diameter by manipulating the differential pressure of continuous mode materials-jetting systems[19]. However, these control schemes are still low-level approaches because whole-part geometry is not directly monitored/manipulated; there is an indirect relationship between the droplet shape and final overall shape of the part.

Since none of these aforementioned closed-loop feedback schemes "close the loop" at the level of whole-part geometry, none of them can account for errors that

occur at a higher level than the process-variable level. Even monitoring the shapes of individual droplets leaves room for higher level errors (i.e., errors occurring in the whole-part geometry) to be undetectable. Furthermore, none of the prior control techniques directly manipulates the shape of the overall geometry and consequently they have potentially limited ability to correct for errors that occur on the whole-part geometry level (such as during-print whole-part deformation, as well as an uneven substrate). In addition to the notion that the existing control schemes mentioned, are limited in the extent to which process uncertainties can be observed and corrected, the disconnect between low-level process variables and the whole-part geometry causes existing feedback control schemes to be vulnerable to changes in the relationships between process variables and whole-part geometry. Existing control schemes are often critically reliant upon models of the relationships between low-level process variables and whole-part geometry, yet these relationships are susceptible to change.

PROPOSED CONCEPT: GREEDY GEOMETRIC FEEDBACK CONTROL
Overview of Two Embodiments of GGF Scheme

The general concept behind the proposed Greedy Geometric Feedback (GGF) control scheme is that the system iteratively decides where to place droplets at run-time based on geometric feedback. During each iteration, using geometric measurements and a model of the target object, the system chooses appropriate locations for subsequent droplets such that the fabricated part ultimately matches the target geometry. The system chooses these deposition locations from a set of candidate locations by selecting those candidates with the highest scores, as defined by a user-selected heuristic. Since the system chooses the best candidates during each iteration, the algorithm is considered to be "greedy". This greedy algorithmic process replaces the more traditional path planning performed *a-priori* by most SFF systems.

There are two embodiments of the GGF control scheme proposed herein. The first embodiment, Local-Greedy Geometric Feedback (Local-GGF) considers a limited number of candidate locations during each iteration. In other words, the algorithm iteratively decides where to place the subsequent droplet by searching a *local selection space*, i.e., a set of locations immediately surrounding the previously deposited droplet.

The second embodiment of the GGF control scheme is Global-Greedy Geometric Feedback (Global-GGF). In this embodiment, during each iteration, the algorithm chooses one or more locations for subsequent droplets from the *global selection space*, i.e., the set of all possible deposition locations throughout the entire build envelope.

Whereas Local-GGF only requires a limited set of geometric measurements (e.g., heights at 4, 6 or 8 locations immediately surrounding the previously deposited droplet) to be performed during each iteration, Global-GGF requires a global scan during each iteration. The global scans required by Global-GGF are more expensive than the local scans required by Local-GGF. However, countering this increased expense of scanning, Global-GGF selects a plurality of droplet locations per iteration whereas Local-GGF only selects one droplet location per iteration.

The commonality between both embodiments, and the crux of the Greedy Geometric Feedback scheme proposed in this paper, is that both variants at run-time iteratively choose deposition locations with the highest scores from their respective selection spaces.

Local-Greedy Geometric Feedback (Local-GGF)

First Iteration of Algorithm

The iterative decision making process begins with the deposition of a seed droplet at a random location within the "global selection space," Q (Figure 3.2A). The global selection space is the set of all possible locations of subsequent droplets. Since droplets can only be placed at fixed intervals, this space is discrete.
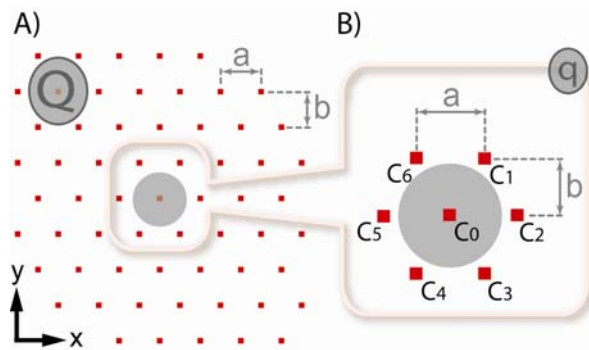
Figure 3.2. Diagram of selection spaces. (a) Global selection space, Q, in which the circle represents a droplet and the squares represent candidate locations of subsequent droplets. (b) Local selection space, q, with seven candidate locations, C_0 through C_6, and the vertical and horizontal spacing intervals, b and a, respectively.

However, scanning the entire global selection space after the placement of each droplet is both computationally expensive and time consuming. Therefore it is more efficient to iteratively perform updates on only a small subset of the global selection space after each droplet is placed and then to use this subset as the selection space for the decision of where to place the subsequent droplet.

This subset of the global selection space is referred to as the "local selection space," q (Figure 3.2B). The local selection space is the set of seven positions that includes the location of the previously deposited droplet (i.e., the current position of the deposition tool) plus its six neighbors.

Each position within the local selection space, q, is considered to be a candidate for the placement of the subsequent droplet and the system measures the heights at each candidate location. These seven candidate locations, C_i, are assigned scores based upon a particular scoring heuristic. While this heuristic can be designed with more complexity, we shall choose this heuristic simply to be the difference between the intended and actual heights at a particular *(x,y)* coordinate for the purposes of this paper. This score is essentially the real-time height error of a certain position:

$$S(x, y, t) = T(x, y) - A(x, y, t)$$ eq. (1)

where *S(x,y,t)* is the score, *T(x,y)* is the height of the intended target geometry and *A(x,y,t)* is the height of the build-surface.

Once heuristic scores are assigned to all seven candidates within the local selection space, the candidate with the highest score becomes the location of the next droplet. If more than one candidate share the value of the maximum heuristic score, then the algorithm randomly selects among them as long as C_0 is not one of the tied candidates. If C_0 is one of the candidates that happen to share the value of the maximum score, then C_0 is given priority and is selected. This last rule serves to reduce the number of tool movements.

Main Loop: Iterative Decision Making

The process of measuring local selection space heights and then selecting a location for the next droplet is repeated. As long as one of the candidates within the local selection space has a score above some threshold, *L,* the iterative cycle continues.

The threshold, *L,* can be user-selected depending on the specific scoring heuristic used. In this case, with the scoring heuristic being the real-time height error,

the threshold, *L*, is simply zero. That is, the print continues as long as at least one of the candidates has a positive height error.

A deadlock is temporarily reached when none of the candidates within the local selection space has a score above the threshold. At this point, the system has satisfied the "halt condition" and it breaks the iterative cycle to address the circumstance.

Halt and End Conditions

The iterative decision making (and hence the printing process) halts when none of the candidates in the local selection space is viable, i.e., none of the candidate scores is greater than the score threshold:

$$Halt\ Condition: \quad S(q) \leq L$$

<div align="right">eq. (2)</div>

When the halt condition is satisfied, the algorithm searches for a "re-insertion point," i.e., a position within the global selection space at which the candidate score is viable. The re-insertion point may be found through a random walk or brute force search (i.e., complete scan of global selection space). In the simulations and physical experiments conducted for this paper, re-insertion points were found through brute force searches by selecting the point in the global decision space with the highest heuristic score. If a viable re-insertion point is found, then the iterative decision making process continues, starting at this point. If no viable re-insertion point is found, then the "end condition" is satisfied and the print is finished:

$$End\ Condition: \quad S(Q) \leq L$$

<div align="right">eq. (3a)</div>

Global-Greedy Geometric Feedback (Global-GGF)

Main Loop: Iterative Decision Making

During each iteration of the Global-GGF algorithm, a scan of the global selection space is conducted. Each candidate position within the global selection space is assigned a score, in a fashion similar to the scoring process of Local-GGF.

After each scan, the top H candidates within the global selection space are chosen to become the locations of the next set of droplets, where H is the maximum number of locations at which droplets can be placed during a single iteration, i.e. per scan of the global selection space.

End Condition

The iterative process ends when none of the candidates within the global selection space has a score above some threshold, L. As in Local-GGF, L is user-selected and for the purposes of this paper taken to be zero. That is, with the scoring heuristic being the real-time height error and the threshold being zero, the print ends when none of the locations within the global selection space has a positive height error.

$$End\ Condition: \quad S(Q) \leq L$$

eq. (3b)

Practical Considerations

Alternative Configurations of the Selection Space

In the experimentation conducted herein, we primarily considered the particular implementation of GGF in which droplets were hexagonally packed. That is, the global selection space was a large set of hexagonally packed points and the local selection space comprised the location of the previously deposited droplet and its six, 6-connected neighbors (6-connectivity). However, a hexagonally packed

selection space is not the only conceivable configuration. A square lattice packing of droplets could also be considered; within the square lattice packing configuration, the local selection space could either be based upon 4- or 8-connectivity. That is, with a square lattice packing of droplets, the local selection space could either be the previously deposited droplet's location and its four, 4-connected neighbors or it could be the previously deposited droplet's location and its eight, 8-connected neighbors.

We only implemented the 6-connectivity configuration in our physical experiments. While we primarily focused on hexagonal packing, this configuration is not necessarily the optimal choice for either efficiency or effectiveness. The selection of the optimal configuration would depend on time requirements, metrology constraints, droplet packing behavior, as well as the specific efficiency/accuracy tradeoff landscape. The optimality of the selection space configuration is beyond the scope of this proof-of-concept treatment of the GGF algorithm.

Metrology / Height Measurement

GGF is independent of the specific imaging modality used for collecting the necessary height information during the print. The computational simulations make no reference to any specific imaging modality, as height information is all that is required by the GGF algorithm. For the physical experimentation, we chose the Microtrak II CMOS laser triangulation distance sensor (MTI Instruments Inc; Albany, NY). Again, numerous other imaging modalities could also conceivably be used including camera-based computer vision techniques, or for in-situ medical applications, real-time CT.

Furthermore, in our particular implementation with the Microtrak II laser sensor we are only able to measure one point at a time. For Local-GGF, in order to scan the local selection space, the gantry robot had to move the sensor to each position

sequentially. However, future advancements in metrology could conceivably enable the real-time monitoring of the entire local selection space. For example, arrays of point sensors or line scanners could be mounted in near proximity to the deposition tool to enable real-time geometric data acquisition.

While future advancements could enable real-time measurement of local selection spaces for Local-GGF, currently available metrology technology can make scanning the global selection space substantially more efficient (which would benefit Global-GGF as well as the re-insertion point searches of Local-GGF). Commercially available laser line scanners, such as the M2D scanner (Mikroelektronik GmbH; Munich, Germany) could capture the entire global selection space with a single swipe across the build-part. Single swipes across the build-surface are relatively low-cost. Moreover, considering that some commercial RP systems such as the Eden Series (Objet Geometries Inc.; Billerica, MA) already require the printhead to swipe across the entire build-part for each layer, adding a laser line scanner to such RP systems could enable seamless geometric data acquisition.

Deposition Technology

The discretized, serial decision making of GGF naturally lends itself to suitability for drop-on-demand RP systems. The computational simulations were based upon drop-on-demand deposition and our physical implementation used a custom wax droplet deposition tool. However, the GGF algorithm is directly applicable to any deposition technology in which the material deposition is discretized.

Continuous filament-based deposition techniques are conceivably relevant if the deposition were discretized into "virtual packets" of material. However, it should be noted that depositing small volumes in a continuous filament system is quite

challenging as they tend to excel in long-path printing situations. It remains to be seen, in future experimentation, to what extent the GGF algorithm is feasible for such continuous filament deposition systems.

Multi-nozzle Implementation and Parallelization

Within the drop-on-demand regime, this algorithm is not limited to single nozzle deposition; commercially available deposition heads comprising an array of hundreds of nozzles can be used with GGF. With an array of hundreds of nozzles, multiple nozzles may be fired simultaneously forming droplet primitives that range in size from that produced by one nozzle to any number of nozzles, i.e. "super-primitives" may be formed of arbitrary size and shape. The choice of primitive size and shape, in the case of an array-based deposition head, would be selected depending on the resolution/print speed trade-off landscape and the operator's specific needs.

Another consideration relating to boosting the speed of GGF prints is the notion of parallelization. While Global-GGF inherently deposits a plurality of droplets per iteration, Local-GGF deposits one droplet per iteration. However, the localized nature of Local-GGF can be exploited by having multiple deposition heads operate on different regions of the part.

Droplet Scale and Print Resolution

It is important to note that GGF is dimensionless in that it is conceptually valid at any scale of droplet or part size. While specific scales were selected for simulation and physical implementation, these scales are only representative of this approach's capability. GGF could be implemented on smaller scale systems than those studied herein. At the extreme end of the size scale, metrology considerations become increasingly important, however these challenges stand to be overcome by future

84

metrology advancements, as the GGF algorithm itself is conceptually valid at any scale.

Determination of Operating Parameters

While this approach notably does not demand detailed modeling of the underlying process physics, as it operates on a high (whole-part) level, certain parameters must still be selected. These operating parameters include primarily, *a* and *b*, the vertical and horizontal spacing intervals between droplets. In the experimentation performed herein, these parameters were selected based on which combination gave the smoothest surface packing for a specific nominal droplet geometry. However, further investigation could unveil a better method for selecting operating parameters, including a computational learning approach (e.g., genetic algorithms) in which the parameters are efficiently and automatically optimized over a wide range of values.

As for selection of the threshold, L, in simulation this parameter was tuned to achieve optimal results. However, in practice, it was found to be an unimportant parameter to tune. Simply setting the parameter equal to 0 produced indistinguishable from other tunings since the physical noise had a much more profound impact on the print. Furthermore, the worst case with an improper tuning is that an additional layer is deposited; the deposition of a single, additional layer is a nuance too small to carry much import in a realistic implementation.

COMPUTATIONAL SIMULATOR FOR GGF

Overview

We developed a Matlab simulator to analyze the performance of the GGF technique in comparison to an open-loop control scheme. The simulator mimicked the

drop-by-drop deposition of build material, similar to that of a drop-on-demand rapid prototyping system.

Computational Representation of Physical Spaces

In the physical world, the target object, the droplets and the deposition field all are continuous spaces. However, for the purposes of simulation, $T(x,y)$, $D(x,y)$ and $A(x,y,t)$ were all represented as discrete spaces by matrices T, D, and A_n, respectively. These matrices, or heightmaps, were essentially spatial sub-samples of their corresponding physical spaces, where T, D and A_n represent the target geometry, droplet geometry and actual geometry at the nth iteration of the algorithm, respectively. The "physical resolution," e, is the distance in the physical world that each of the matrixes' discrete element-to-element intervals represent. We simulate the physical printing procedure by tracking printed matter at the resolution, e, which is finer than the resolutions of Q and q.

While physical spaces are represented as heightmaps in these simulations, it should be noted that not all 3D objects can be represented as such, due to features like overhangs or internal cavities. The heightmap representation was used for computational simplicity, but the representation could be generalized by using voxel or parametric representations. That is, a top-down 2.5D geometric representation was used for these simulations; however, this same algorithmic principle could be represented in a fully 3D geometric model such as a voxel representation, or a parametric representation in which the geometry is explicitly modeled with equations.

Intended Target Object Heightmap

The matrix T was created by sub-sampling $T(x,y)$ at the simulation resolution, e (Figure 3.3). Each sample point is e units in physical space away from one another.
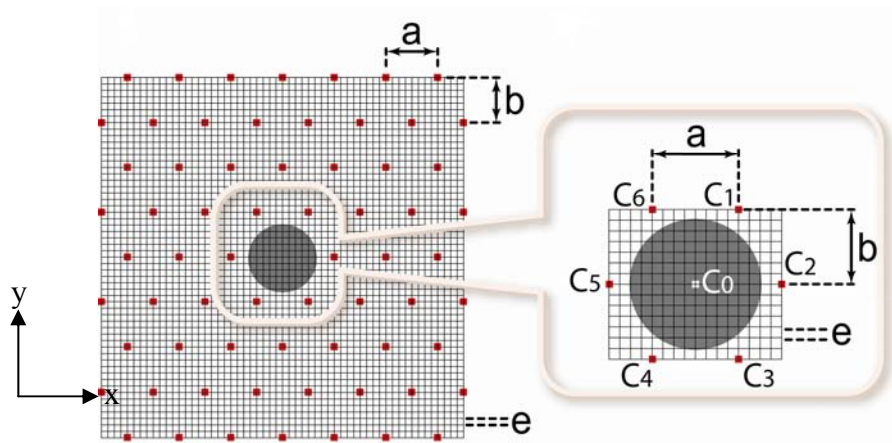
Figure 3.3. Physical resolution. Overlay of physical resolution matrices on the Global Selection Space (Left) and the Local Selection Space (Right).
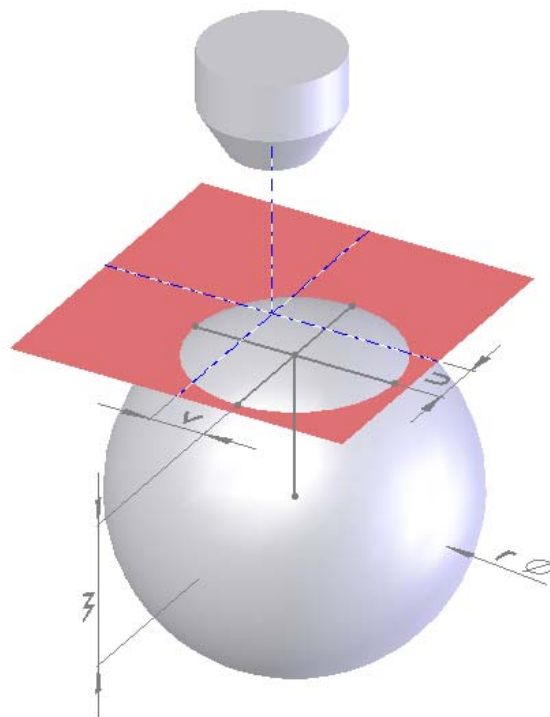
Figure 3.4. Diagram of droplet parameters. The deposition tool nozzle above the substrate and the underlying droplet modeled as a lens. Also shown is the corresponding truncated sphere and associated parameters u, v, w, and r.

Single Droplet Heightmap

The liquid droplet shape associated with RP techniques can be mathematically approximated using a lens model, as explained in prior literature[17]. Therefore, an approximation for the surface of a single droplet is:

$$\hat{D}(x, y) = \sqrt{r^2 - (x - (X - u)) - (y - (Y - v))} + w \qquad \text{eq. (4)}$$

where r is the radius of curvature; X and Y are the lens' center coordinates; u and v are the deviations of the actual droplet center from the intended center due to process error; w is the lens' center-to-substrate offset (Figure 4.4). Note that u and v represent the translation of the droplet relative to the deposition tip's location, i.e., natural deviation from the intended droplet center due to physical process errors.

Given the lens parameters, eq. 4 can be used to generate a matrix that approximates the surface of the droplet. This surface can be sub-sampled at the resolution, e, to create the heightmap of the nth droplet, $\boldsymbol{D_n}$:

$$[D]_n = \begin{bmatrix} \hat{D}(0,0) & \hat{D}(e,0) & \hat{D}(2e,0) & \ldots & \hat{D}(C \cdot e,0) \\ \hat{D}(0,e) & \hat{D}(e,e) & \hat{D}(2e,e) & & \\ \hat{D}(0,2e) & \hat{D}(e,2e) & \hat{D}(2e,2e) & & \\ \vdots & & & \ddots & \\ \hat{D}(0,R \cdot e) & & & & \hat{D}(C \cdot e, R \cdot e) \end{bmatrix} \qquad \text{eq. (5)}$$

where $\hat{D}$ is a function of the lens parameters: r_n, X_n, u_n, Y_n, v_n and w_n. R and C represent the number of rows and columns of the matrix (i.e. size) required to describe the simulated X-Y plane.

Deposition Field Heightmap

The deposition field immediately after the nth droplet has been deposited can be represented with the heightmap, $\boldsymbol{A_n}$:

$$[A]_n = \begin{bmatrix} A(0,0,t_n) & A(e,0,t_n) & A(2e,0,t_n) & \cdots & A(C \cdot e,0,t_n) \\ A(0,e,t_n) & A(e,e,t_n) & A(2e,e,t_n) & & \\ A(0,2e,t_n) & A(e,2e,t_n) & A(2e,2e,t_n) & & \\ \vdots & & & \ddots & \\ A(0,R \cdot e,t_n) & & & & A(C \cdot e,R \cdot e,t_n) \end{bmatrix} \qquad \text{eq. (6)}$$

where t_n is the time just after the nth droplet has been deposited.

Simulation Flow

The core of the simulation is the iterative update of the deposition field heightmap, A_n. Since A_n represents the physical space in which the print is occurring, the A_n heightmap reflects the results of all algorithmic decisions as well as the effects of process uncertainties. The simulation begins with A_n as a matrix of zeros.

Then a seed droplet, D_1, is generated by using the lens parameters: r_1, u_1, v_1 and w_1. The seed droplet's center coordinates (X_1, Y_1) are randomly selected from points in the global selection space. The first droplet is deposited in simulation by superimposing the droplet matrix, D_1, over the deposition field matrix, A_0.

$$[A]_1 = [A]_0 + [D]_1 \qquad \text{eq. (7)}$$

Once the seed droplet has been deposited into the deposition field, the main iterative portion of Local-GGF commences. In order to choose the location of the second droplet, (X_2, Y_2), the local selection space is constructed. The set, q_n, represents the local selection space just before the nth droplet is deposited:

$$q_2 = \{C_0 \quad C_1 \quad C_2 \quad C_3 \quad C_4 \quad C_5 \quad C_6\}_2 \qquad \text{eq. (8)}$$

The scores of the candidates in the local selection space are generated:

$$S(q_2) = \{S(C_0) \quad S(C_1) \quad S(C_2) \quad S(C_3) \quad S(C_4) \quad S(C_5) \quad S(C_6)\}_2$$

$$\ldots \quad = \quad \left\{ T\left[\frac{C_i}{e}\right] - A\left[\frac{C_i}{e}\right] \mid i \in Z, 0 \le i \le 6 \right\}_1 \qquad \text{eq. (9)}$$

where C_i represents the $(x,y)_i$ coordinates (i.e. location of the ith candidate location in physical space), and $C_i/e = (x/e, y/e)_i$ (i.e. location of the ith candidate location represented in terms of $A[\ ]$'s matrix indexes).

The location of the next droplet is selected by choosing the candidate with the highest score, and the droplet is deposited in simulation by superimposing the matrixes:

$$[A]_2 = [A]_1 + [D]_2 \qquad \text{eq. (10)}$$

These steps are repeated, whereby:

$$q_n = \{C_0 \quad C_1 \quad C_2 \quad C_3 \quad C_4 \quad C_5 \quad C_6\}_n$$

$$= \left\{ (X_{n-1}, Y_{n-1}) \quad \left(X_{n-1} + \frac{a}{2}, Y_{n-1} + b\right) \quad (X_{n-1} + a, Y_{n-1}) \right.$$

$$\left. \left(X_{n-1} + \frac{a}{2}, Y_{n-1} - b\right) \quad \left(X_{n-1} - \frac{a}{2}, Y_{n-1} - b\right) \quad (X_{n-1} - a, Y_{n-1}) \quad \left(X_{n-1} - \frac{a}{2}, Y_{n-1} + b\right) \right\}_n$$

eq. (11)

$$S(q_n) = \left\{ T\left[\frac{C_i}{e}\right] - A\left[\frac{C_i}{e}\right]_{n-1} \mid i \in Z, 0 \le i \le 6 \right\} \qquad \text{eq. (12)}$$

$$[A]_n = [A]_{n-1} + [D]_n = [A]_0 + \sum_{k=1}^{n} [D]_k \qquad \text{eq. (13)}$$

For each set of simulation parameters, a range of heuristic score thresholds, L, were tested to find near-optimal performance of the Local-GGF process. The threshold that yielded the lowest RMS surface height error was selected. The optimal heuristic score thresholds varied from case-to-case and are listed in the "Results" section where appropriate.

The simulation ends when end condition (eq. 3) has been satisfied:

$$(T[r,c] - A[r,c]) \leq L, \quad where\ r \in Z, 0 \leq r \leq R\ and\ c \in Z, 0 \leq c \leq C \qquad \text{eq. (14)}$$

where r and c are the matrix indexes, and $T[\ ]$ and $A[\ ]$ are of size R by C.

The same simulation engine was used for Global-GGF, except that the top 50% of the candidates in the global selection space were selected for subsequent deposition during each iteration.

Modeling of Process Uncertainty

Process uncertainties that occur at the droplet-shape level, were incorporated into the simulations by randomly drawing the r, u, v and w parameters from normal distributions; $r \sim N(r_{nom}, \sigma_r)$, $u \sim N(u_{nom}, \sigma_u)$, $v \sim N(v_{nom}, \sigma_v)$ and $w \sim N(w_{nom}, \sigma_w)$, where σ_r, σ_u, σ_v, σ_w, r_{nom}, u_{nom}, v_{nom} and w_{nom} are user-defined parameters of the r, u, v and w distributions. Variation in the r parameter represents uncertainty in the radius of curvature of the droplets. Uncertainty in the x-y positioning of droplets is represented by variation in u and v. The variation in w represents uncertainty in the maximum droplet thickness.

Process uncertainties that occur on the overall part-shape level (e.g., during-print part deformation due to melting), can be incorporated by applying a morphological filter to A_n during each iteration after the D_n matrix is superimposed. The morphological filter used in this paper is a 2-D linear filter that uniformly averages over a specified radius of pixels.

While these simulated process uncertainties do not capture all existing physical possibilities, they do serve as a representative set.

Simulation Parameter Selection

The droplet parameters r_{nom}, u_{nom}, v_{nom} and w_{nom} were selected based upon suggested values in prior literature[17]:

Table 3.1 Droplet parameter values.

r_{nom}	u_{nom}	v_{nom}	w_{nom}
5 mm	0 mm	0 mm	$-$ 3 mm

These parameter values result in a droplet radius of 4 mm and a droplet maximum height of 2 mm. The values of σ_r, σ_u, σ_v, σ_w and the score threshold, L, were experimentally varied throughout the following simulation experiments.

Next, an optimal value for the droplet center-to-center spacing had to be determined, which yielded minimal surface height variations when droplets were hexagonally packed. The spacing necessary for the midpoint between droplet centers to have a height equal to the height of the droplet centers was:

$$\sqrt{3r^2 + 2rw - w^2} = \sqrt{3 \cdot 5^2 - 2 \cdot 5 \cdot 3 - (-3)^2}\,[mm] = 6 \; mm \qquad \text{eq. (15)}$$

The a, b and e parameters were coupled and had to be chosen carefully. In order for the droplets to hexagonally pack, the a and b values had to be in a $2/\sqrt{3}{:}1$ ratio. However, in order to have the hexagonally-packed droplets' centers perfectly align with the square-packed matrix, A_n, the a and b intervals had to be multiples of e. One set of a and b values that were multiples of e and yet still closely approximated a $2/\sqrt{3}{:}1$ ratio, was $a{=}8e$, $b{=}7e$. Given that the center-to-center spacing, a, had to be 6 mm (as shown above in eq. 15), e and b were then fixed to 0.75 mm and 5.25 mm, respectively.

Simulation of Open-Loop Control

The simulator for the open-loop SFF technique was very similar to that for the GGF case. However, the iterative decision making was replaced by a list of points that corresponded to the locations for droplet centers, i.e., a tool path plan. This list was generated by filling the intended target geometry with the nominal droplet-shaped structuring element, until all points on the surface had heights greater than or equal to $T(x,y)$. Droplets, D_n, were then placed in A_n for each point in the list.

PHYSICAL TEST PLATFORM FOR GGF
(PROOF-OF-CONCEPT IMPLEMENTATION)

Overview

In order to validate the concepts proposed above, and also to address the feasibility of physically implementing the control scheme, a physical test platform was developed to demonstrate the GGF control technique.
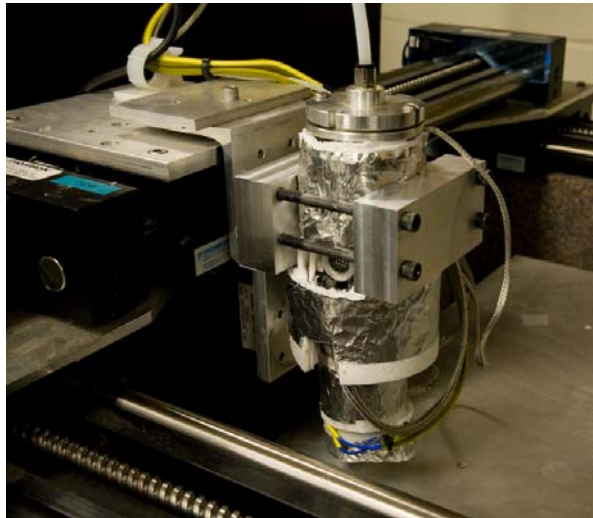
Figure 3.5. Physical experimentation platform. Custom wax deposition tool mounted on X-Y-Z gantry robot

System Design

A custom SFF test platform was developed to implement and test the GGF technique; in addition to performing GGF prints, the system was also capable of performing open-loop prints under similar test conditions. By controlling the print conditions and inducing specific forms of process uncertainty, the performance of different control schemes could be studied.

Positioning System

We designed and built a custom gantry positioning system comprising two coupled linear actuators along the X-axis, one along the Y-axis and one along the z-axis (Aerotech Inc.). The positioning system was capable of moving at accelerations up to 20 m/s^2. The system has a positioning accuracy and repeatability of 25 μm. The custom-fabricated granite base reduced structural vibration and ensured accurate tool positioning.

Deposition Tool

The custom-designed and fabricated deposition tool was a paraffin drop-on-demand tool. A 0.007" diameter VHS-M jet valve (INKX05153350AA; Lee Company) was attached to a custom-fabricated aluminum liquid reservoir through a Minstac male-to-male connector (INZX0530650AA; Lee Company) and an in-line 12 micron filter (INMX0350000AA; Lee Company). The aluminum reservoir heated with a 200 Watt band heater and monitored with a band-mounted J-type thermocouple. The reservoir was also pressurized in an air-over-liquid fashion at 12 psi.

A 5V control signal was output from the controlling PC through a digital I/O board and fed into a spike-and-hold valve controller (IECX0501350A; Lee Company) which provided the proper electrical control signal to the valve.

Metrology

Measurements of the printed part height were used during closed-loop prints as part of the GGF algorithm, as well as for quantifying part height error after the completin of both closed- and open-loop prints.

While future implementations would ideally monitor the heights of neighboring candidates simultaneously in real-time, in this proof-of-concept implementation, the neighboring candidate heights were measured serially by a single-point height sensor. The sensor used in this system was a CMOS laser triangulation range sensor (Microtrak II, MTI Instruments Inc.).

The sensor had a range of 10 mm, a spot size of 30 μm, and a resolution of 1.25 μm. The sensor output an analog signal, which was read-in by the controlling PC through an analog-to-digital converter.

Control Software

A custom-written control program was developed in C++ to execute the GGF and open-loop control sequences. Aerotech C++ libraries were integrated to handle low-level motion control operations and sensor I/O.

Implementation Considerations

Several practical issues had to be addressed during the implementation of the feedback control scheme. Firstly, due to the parallax between the laser beam and laser sensor, tall vertical parts sometimes were difficult to measure; the vertical edges of the parts occasionally hid the laser beam from its own laser sensor. This problem is not a fundamental limitation of the GGF control scheme, rather, it was a practical concern of this particular proof-of-concept implementation. However, by printing parts with smoother surfaces, adverse effects caused by this issue were avoided.

Another practical issue encountered was the size of the droplets produced by the deposition tool. The lower limit of the control system's valve signal was one millisecond. Given the particular valve used, and the minimum reservoir pressure (dictated by a threshold below which the fluid pooled instead of jetted), the droplet was restricted to diameters on the order of approximately one millimeter. Again, this is not by any means a fundamental limitation of the control algorithm itself. Furthermore, the conceptual validity and feasibility of implementation can be demonstrated with this platform regardless of the particular droplet size. On a side note, the size of the droplets resulted in a thermal mass which yielded droplets that took about one second to set, and about three seconds to freeze. The larger the droplets the more they retained heat due to their increased mass, and thus, the longer they took to freeze. Consequently, the time between droplets had to be selected accordingly to ensure subsequently droplets were not deposited on top of molten droplets.

It is important to note that this experimental SFF platform was intended to demonstrate the physical implementation of the control algorithm and is a proof-of-concept. No claims are being made about the optimality of the platform as a high-throughput SFF system, rather, we are only making claims about the *algorithm* itself.

Induced Process Uncertainties

We induced process uncertainties in several ways. In order to induce uncertainty in the droplet size, which represents uncertainty in the material properties of the build-material, we varied the hold time of the valve by adding a Gaussian random term to the nominal hold time of 4 milliseconds.

In order to represent uncertainty of the substrate geometry, we printed samples on top of ABS plastic constructs to create non-flat print substrates.

Print Parameter Selection

We determined the nominal valve hold time based upon the desired droplet size. The drop-to-drop distance was empirically determined based upon which spacing yielded a line of droplets of constant height. If the spacing was too small, the line of droplets would be discontinuous. If the spacing was too great, the droplets would overlap and the height of the printed line would continue to increase resulting in a line with a non-flat surface.

The time between droplets was empirically determined to be four seconds to ensure that droplets were not being deposited on top of a molten surface. While this is not optimized for efficiency and speed, we needed to ensure solidification of the substrate since we were primarily concerned with measuring the resultant geometric fidelity.

PERFORMANCE EVALUATION METHODOLOGY

We used an open-loop SFF process (no feedback control) as a baseline for comparison in both the simulation and physical experiments.

The quantitative metric used for comparison was the RMS surface error between the actual printed surface and the theoretically intended surface. This was calculated via a simple point-by-point comparison of the actual and intended surfaces:

$$RMS\ Error = \sqrt{\frac{1}{R \cdot C} \sum_{j=1}^{R} \sum_{i=1}^{C} (T[i,j] - A[i,j])^2} \qquad \text{eq. (16)}$$

Methodology for Simulation Experiments

In simulation, the GGF technique's performance was compared to that of the open-loop baseline by simulating the print of three different target shapes with both

GGF and open-loop control schemes. The three target shapes chosen were: 1) a rectangular prism, 2) a dome and 3) an ovine meniscus cartilage.

For each control scheme and each target shape, the RMS surface error was measured under four types of process uncertainty (as discussed in *Section 5.4*). These four types of process uncertainty were: 1) droplet radius of curvature, 2) droplet thickness, 3) droplet placement, and 4) during-print part deformation of the part.

To test the control scheme under uncertainty in droplet radius, the droplet radius was varied during simulation by adding a random radius offset to the nominal radius dimension, r. The distribution of this random offset was characterized by the standard deviation of this random variable (i.e. the radius offset). To test under varying levels of uncertainty in radius, this random variable's standard deviation was varied from zero (no uncertainty in the radius) to 1.5 mm.

Similarly, to test the control scheme under uncertainty in droplet thickness, a random offset was added to the parameter, w. To test under varying levels of uncertainty in droplet thickness, the standard deviation of the random offset was varied from zero (no uncertainty in droplet thickness) to 1.5 mm.

To test under varying levels of uncertainty in droplet placement, a random offset was added to the u and v parameters; the standard deviation of this offset was varied from zero to 6 mm.

To simulate the fourth type of uncertainty, during-print part deformation, the linear morphological filter was applied to the geometric model after each iteration of the simulation. To simulate varying levels of during-print part deformation, the radius of the filtering element was varied from zero to 3 mm.

Each simulation was conducted three times under identical conditions, and then the results were averaged by taking the arithmetic mean.

Methodology for Physical Experiments

In the physical experimentation, the target shape was a 5 mm tall dome with a radius of curvature of 12 mm. Both GGF and open-loop were tested on the dome target shape, and the RMS surface error was measured under: 1) no induced error, 2) a variation in valve time with a standard deviation of 20 milliseconds, and 3) a non-flat substrate representing situation/environmental uncertainty (the print was conducted on top of an ABS plastic dome of radius 12 mm and height 3 mm).

The RMS surface error calculation was made based upon a 0.2 mm resolution laser scan of the complete printed object, which was conducted at the conclusion of each scan. Point-to-point comparison between the scan of the printed component and the intended geometry was conducted to perform the calculation.

SIMULATION RESULTS & DISCUSSION

Case 1 – Varying Uncertainty in Droplet Radius of Curvature

The RMS errors were smaller for Local-GGF than for open-loop control for all shapes and all degrees of uncertainty in the radius of curvature (Figure 3.6). Local-GGF's RMS error appeared to asymptotically level-off whereas the open-loop error appeared to grow exponentially. With a 1.125 mm standard deviation in the radius of curvature distribution (28% of the nominal radius of curvature), the Local-GGF RMS error was 74%, 74% and 70% less than the open-loop error for the rectangular prism, dome and meniscus, respectively. This disparity in performance grew as the uncertainty in radius increased.

The error growth of the open-loop case seems to grow exponentially as the radius of curvature, and hence the droplet volume, become less certain. As the uncertainty increases, so does the mean droplet volume, which contributes to fast

growth of the RMS error in open-loop. The error growth for GGF appears to slow as

uncertainty increases, due to the error fighting behavior of the algorithm.
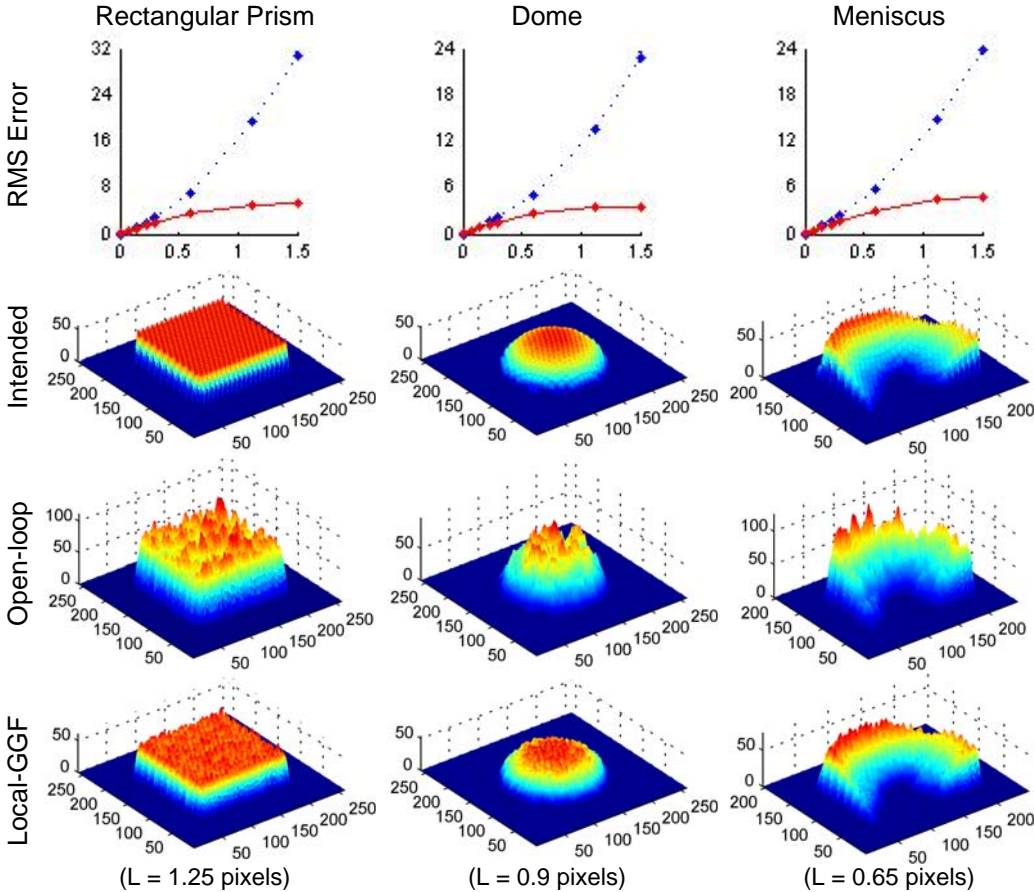
Figure 3.6. Performance comparison with uncertainty in droplet radius of curvature. (Row 1) RMS error of printed surface (mm) vs. standard deviation (i.e., SD) of droplet radius of curvature distribution (mm) [Dotted Line = Open Loop; Solid Line = Local-GGF]. (Rows 2-4) Surface plots of intended and printed geometries (mm) with SD of radius of curvature uncertainty equal to 1.125 mm.

Case 2 – Varying Uncertainty in Droplet Thickness

The RMS errors were smaller for Local-GGF than for open-loop control for all

shapes and all degrees of uncertainty in the droplet thickness (Figure 3.7). GGF's

RMS error appeared to grow linearly, whereas the open-loop error seemed to grow

exponentially. With a 1.125 mm standard deviation in the droplet thickness

distribution (56% of the nominal droplet thickness), the Local-GGF RMS error was 51%, 55% and 49% less than the open-loop error for the rectangular prism, dome and meniscus, respectively. This disparity in performance grew as the uncertainty in droplet thickness increased.
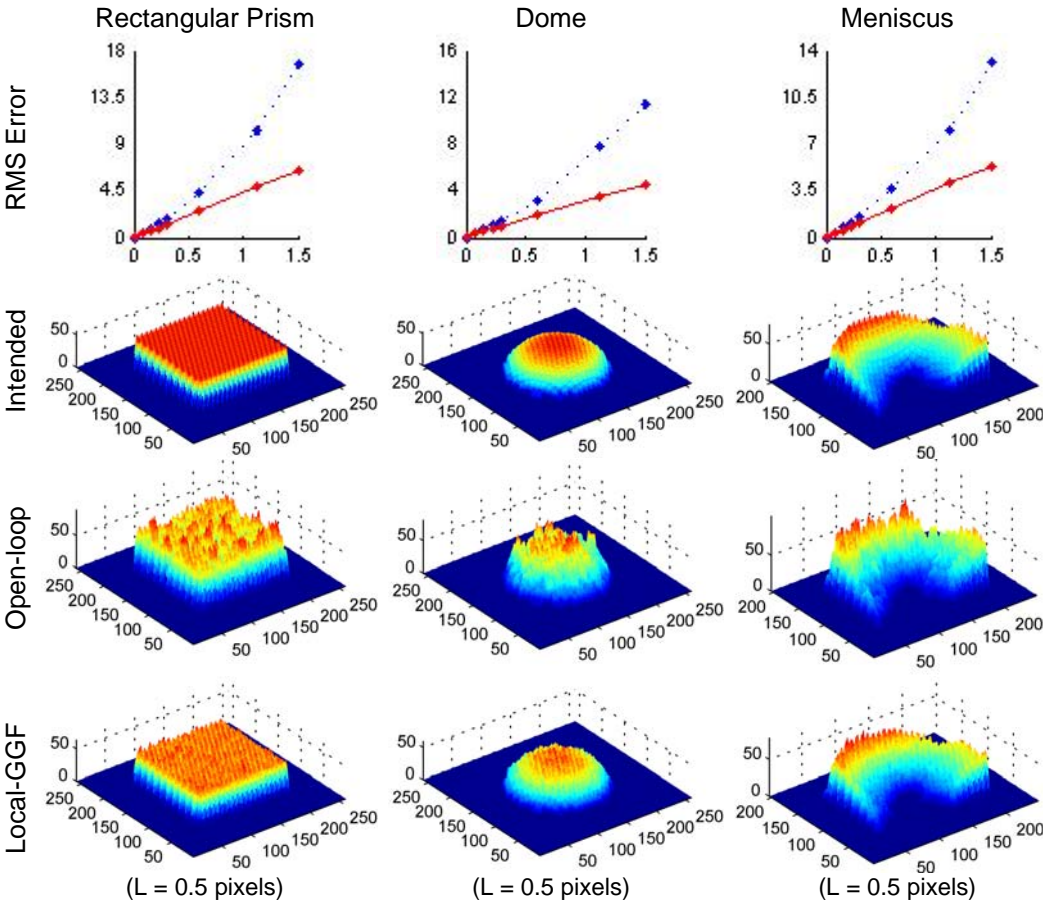
Figure 3.7. Performance comparison with uncertainty in droplet thickness. (Row 1) RMS error of printed surface (mm) vs. standard deviation (i.e., SD) of droplet thickness distribution (mm) [Dotted Line = Open Loop; Solid Line = Local-GGF]. (Rows 2-4) Surface plots of intended and printed geometries (mm) with SD of droplet thickness uncertainty equal to 1.125 mm.

As in the previous case, as uncertainty in the droplet thickness increases, so does uncertainty in the droplet volume. As this uncertainty increases, the mean droplet volume grows, which leads to rapidly increasing RMS error for open-loop.

101

Again, GGF error grows less quickly and the error growth slows (although this slowing is much less pronounced than in the prior case).
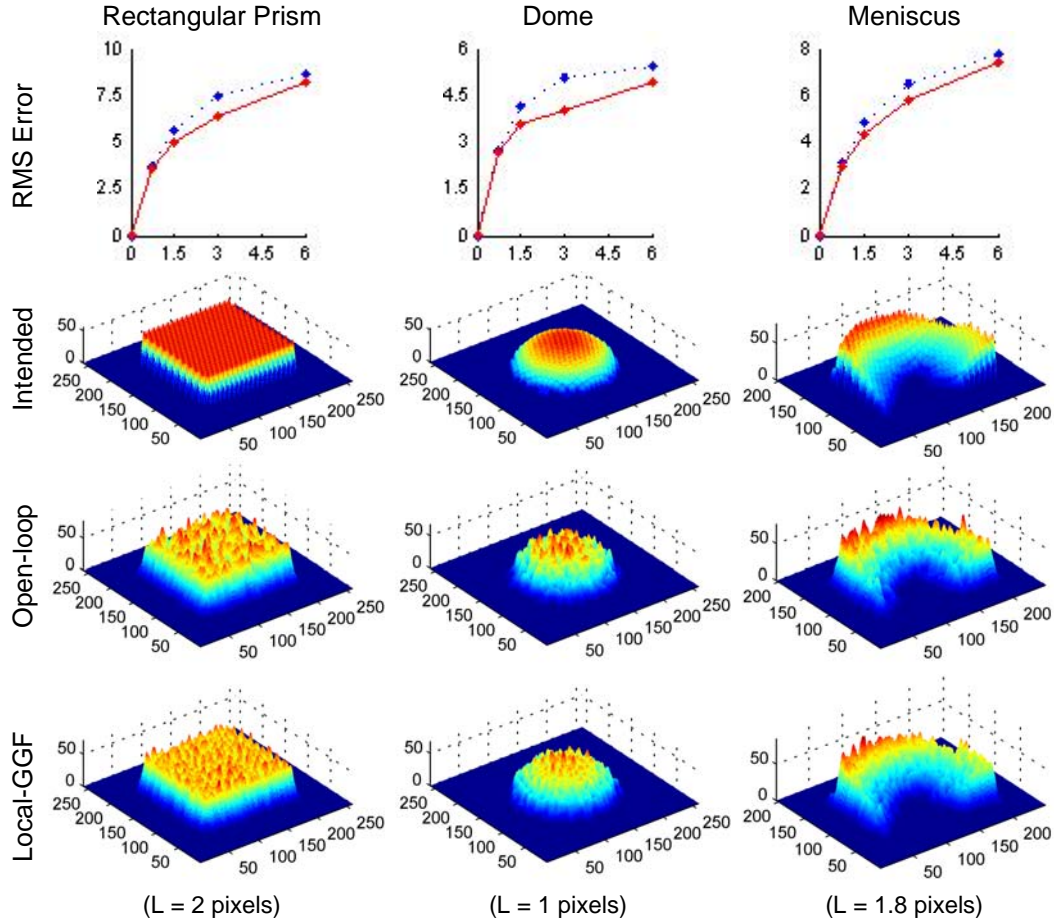
Figure 3.8. Performance comparison with uncertainty in droplet placement. (Row 1) RMS error of printed surface (mm) vs. standard deviation (i.e., SD) of placement distribution (mm) [Dotted Line = Open Loop; Solid Line = Local-GGF]. (Rows 2-4) Surface plots of intended and printed geometries (mm) with SD of placement uncertainty equal to 3 mm.

Case 3 – Varying Uncertainty in Droplet Placement

The RMS errors were smaller for Local-GGF than for open-loop control for all shapes and all degrees of uncertainty in X-Y droplet placement (Figure 3.8). Both GGF and open-loop RMS error grew with asymptotic behavior; however, the GGF error was less than that of the open-loop control. With a 2 mm standard deviation in

the droplet translation distribution (25% of the nominal droplet diameter), the Local-GGF RMS error was 14%, 20% and 11% less than the open-loop error for the rectangular prism, dome and meniscus, respectively.
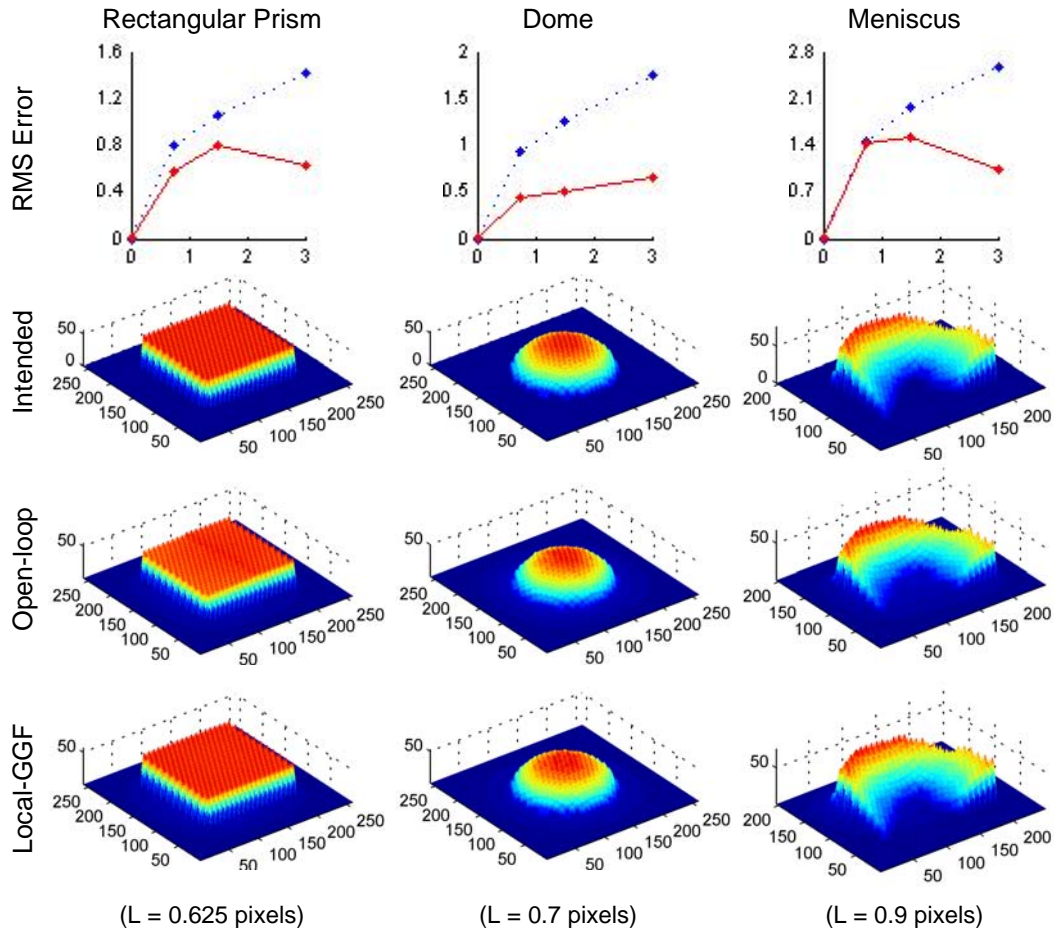
Figure 3.9. Performance comparison with during-print part deformation. (Row 1) RMS error of printed surface (mm) vs. radius of morphological filtering element (mm) [Dotted Line = Open Loop; Solid Line = Local-GGF]. (Rows 2-4) Surface plots of intended and printed geometries (mm) with filtering radius set at 3 mm.

The less pronounced disparity between open-loop and GGF is likely due to the noise averaging characteristics of a positional error centered about the intended droplet location. This disparity would be more pronounced in uni-directionally biased circumstances.

103

Case 4 – Time-Varying Deformation of Printed Objects

The RMS errors were smaller for Local-GGF than for open-loop control for all shapes and all degrees of during-print part deformation (Figure 3.9). With a 3 mm radius filter acting over the first $1/8^{th}$ of the nominal open-loop print duration, the Local-GGF RMS error was 48%, 50% and 52% less than the open-loop error for the rectangular prism, dome and meniscus, respectively.

The disparity between open-loop and GGF grew rapidly, and conceivable could grow to infinity; in an extreme case, a temporary melting effect could nearly annihilate the open-loop part, but be nearly fully restored by GGF.

The nature of this growth, and the specific shape of the error growth, is entirely dependent on the specific details of the type of time-varying deformation imposed. For example, melt would have an entirely different behavior from evaporation.

Case 5 – Investigation of Global-GGF, 4/6/8 Connectivity (Simulation of Droplet Misfiring)

A simulation experiment was conducted to gain basic insight into the performance of alternative implementations of GGF: Global-GGF versus Local-GGF, and 4/8 connectivity instead of 6-connectivity.

In this experiment, a 10mm (H) X 30mm (W) X 30mm (L) rectangular prism was printed with 1mm diameter, 0.1mm thick droplets. The droplet would fail to fire a certain percentage of instances in which it was commanded to fire.

As Figure 3.10 demonstrates, in terms of RMS error, Global-GGF appears to behave in a very similar nature to Local-GGF. In fact, in simulation, they were indistinguishable. Furthermore, in terms of RMS error, 4-connectivity versus 8-connectivity has no effect. The square lattice packings (4- and 8-connectivity) present slightly different results from hexagonal packing (6-connectivity), but this difference

is more a property of packing behavior of droplets than it is a reflection of the GGF algorithm.
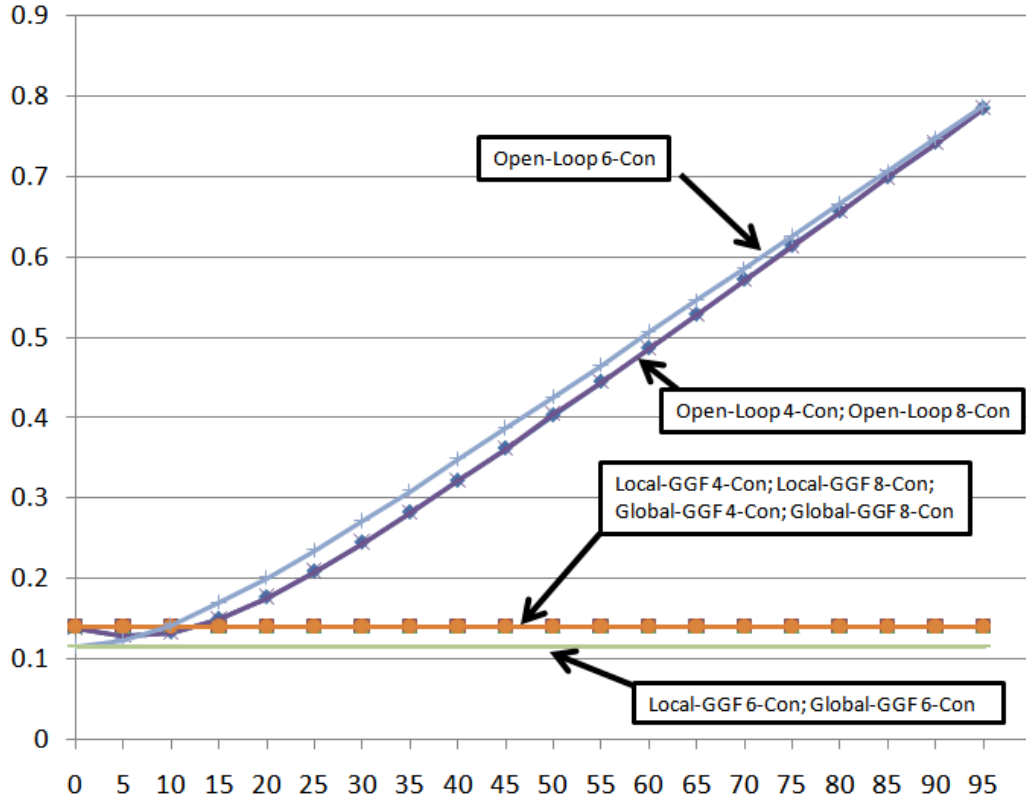
Figure 3.10. RMS error normalized to maximum part height vs. percentage of attempted droplet firings with no droplet fired. Error growth shown for all implementations of GGF and open-loop control schemes.

It is not surprising that there is not distinguishable difference in terms of geometric fidelity between Local-GGF and Global-GGF, as the latter is merely a parallelized version of the former.

Cost of Geometric Feedback Scanning

In simulation, we tracked the number of times a droplet was deposited (and hence the number of times the local selection space was scanned in Local-GGF), as well as the number of times a global selection space scan was conducted (during

Global-GGF or for the re-insertion point searches of Local-GGF). Some types of uncertainty create more of a scanning expense than others.

For example, in Case 5, when droplets fail to fire a certain percentages of the time, the GGF algorithm keeps working in an attempt to fight the error. Even in the extreme circumstance when droplets fail to fire with a 95% probability, GGF won't cease until it successfully combats the error. On the other hand, as a result of its incessant error fighting, the print continues much longer than in the open-loop case and the overall scanning cost and print duration rises accordingly. Of course, however, along with open-loop's shorter and less expensive run (since it ends as scheduled without ever detecting an error) comes the lowered geometric fidelity. To a certain extent, the increased duration of print and cost of scanning is the unavoidable price to pay for increased geometric fidelity (Figure 3.11).

At a certain point (above 60% or so) it becomes a question of how important geometric fidelity is to the user. The duration of Local-GGF scales with the number of droplets and the duration of Global-GGF scales with the number of global selection space scans: both grow exponentially and become substantially large above the 60% point (Figure 3.12).

However, contrary to the rising cost of scanning seen in Case 5, in Case 2 with a positive-biased uncertainty in droplet thickness, the cost of scanning reduces with increased uncertainty (Figure 3.13). Since the uncertainty adds more material than anticipated, the uncertainty only brings the part closer to its intended geometry faster. Again, open-loop is not aware of the additional build-material and continues its print longer than it should, as scheduled *a priori* (Figure 3.14).
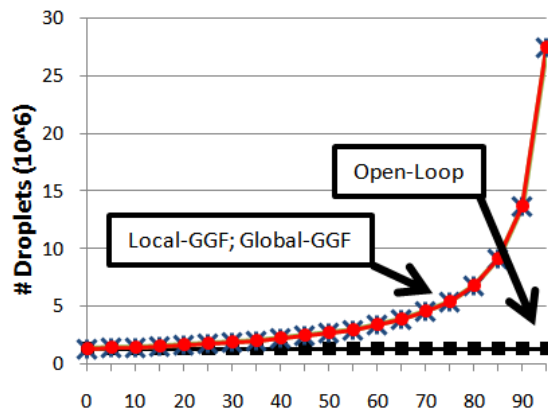
Figure 3.11. Number of droplets fired during "No-Fire" experiment. Number of droplets vs. probability of attempted droplet firing resulting in no droplet fired.
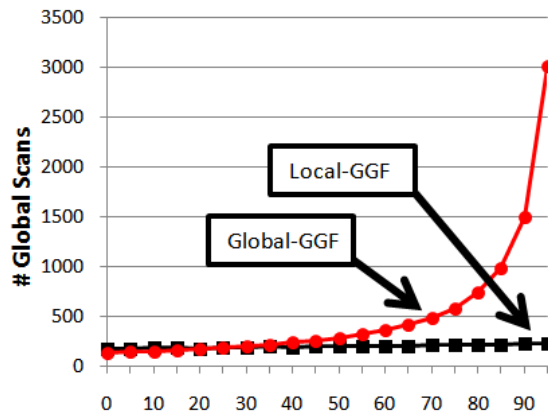
Figure 3.12. Number of global scans during "No-Fire" experiment. Number of global scans conducted vs. probability of attempted droplet firing resulting in no droplet fired.

107
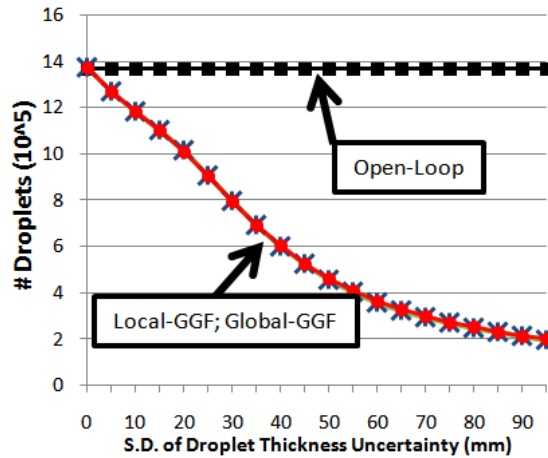
Figure 3.13. Number of droplets fired during "Positive-Biased Uncertainty in Droplet Thickness" experiment. Number of droplets vs. probability of attempted droplet firing resulting in no droplet fired.
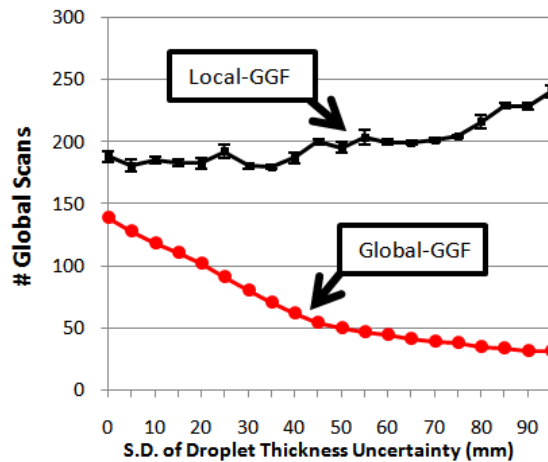
Figure 3.14. Number of global scans during "Positive-Biased Uncertainty in Droplet Thickness" experiment. Number of global scans conducted vs. probability of attempted droplet firing resulting in no droplet fired.

PHYSICAL EXPERIMENTATION RESULTS & DISCUSSION

Case 1 – No Induced Process Uncertainty

The baseline case was one in which both open- and closed-loop prints of a dome were performed. The GGF algorithm did not require the tuning of any control parameters (beyond droplet-to-droplet spacing which was identical to that used for the open-loop control). However, the open-loop algorithm required the determination of nominal layer thickness.

A 10 mm by 10 mm, 11-layer cube was printed to estimate the nominal layer thickness. By dividing the actual cube height by the number of layers, the resulting estimated layer thickness was 0.60 mm. However, the resulting printed dome was too tall; the surface exhibited an RMS error of 1.98 mm (Figure 3.15). Therefore, another round of layer thickness estimation was conducted on a printed dome (as opposed to the cubic test piece). Now, with complete *a priori* knowledge, the estimate of layer thickness obtained was more accurate (1.04 mm) and resulted in a printed dome that more closely resembled the target geometry. The open-loop print conducted with *a priori* knowledge exhibited an RMS surface error of 0.58 mm.

The Local-GGF print, *without a priori* knowledge of the layer thickness printed the dome with the same geometric fidelity (as determined by RMS surface error), 0.59 mm.

Case 2 – Variation in Valve Hold Time

When a positive random variable was added to the nominal hold time (standard deviation of 0.020 ms), this mimicked a native process uncertainty in the droplet volume (Figure 3.16). The open-loop printed dome exhibited an RMS surface error of 1.33 mm; the Local-GGF printed dome exhibited an RMS surface error of 0.69 mm.
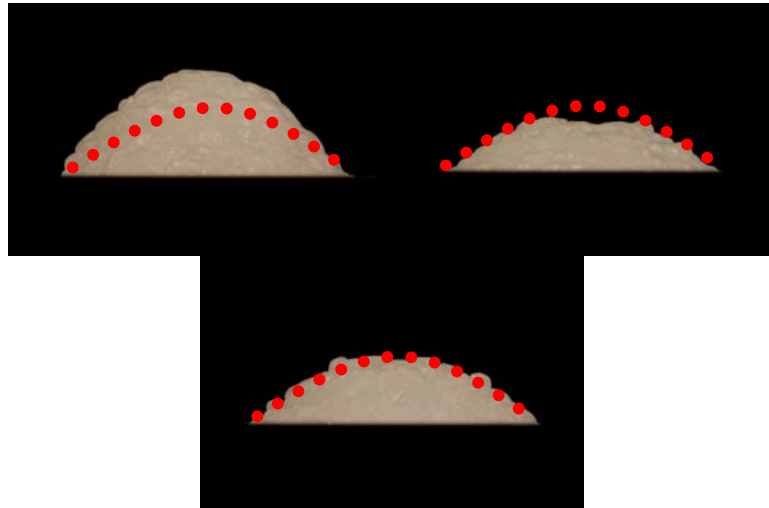
Figure 3.15. Photographs of printed dome constructs. (Top-Left) Open-Loop with partial *a priori* knowledge. (Top-Right) Open-loop with complete *a priori* knowledge. (Bottom-Center) Local-GGF printed construct.
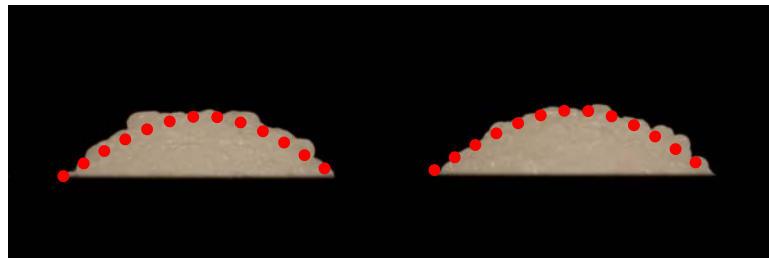
Figure 3.16. Photographs of printed dome constructs. (Left) Open-Loop. (Right) Local-GGF.

Case 3 – Non-Flat Substrate

When the dome was printed on top of an ABS spherical-lens substrate (1 mm H X 6 mm D), the open-loop print exhibited an RMS surface error of 1.16 mm; the Local-GGF dome had an error of 0.36 mm (Figure 3.17).
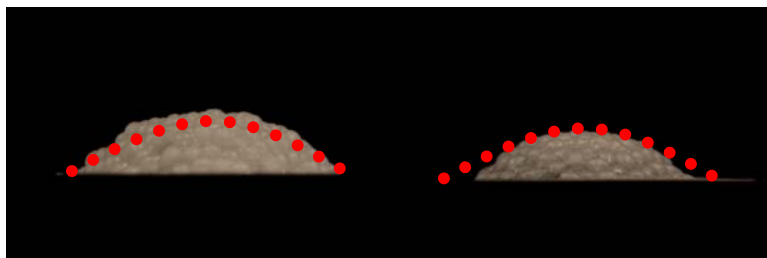
Figure 3.17. Photographs of printed dome constructs. (Left) Open-Loop. (Right) Local-GGF.

Case 4 – Reduced Deposition Tool Pressure

When the pressure of the deposition tool's reservoir was reduced to 8 psi while holding the droplet-to-droplet spacing constant (mimicking a natural variation in system conditions), the resultant droplets were smaller (Figure 3.18). The open-loop printed dome had an RMS surface error of 2.57 mm; the Local-GGF maintained an error of only 0.34 mm.
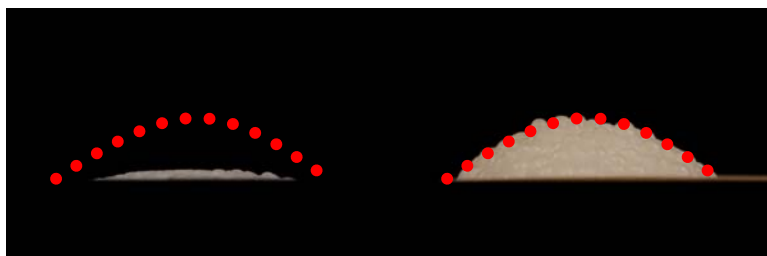
Figure 3.18. Photographs of printed dome constructs. (Left) Open-Loop. (Right) Local-GGF.

CONCLUSIONS

The results presented in this paper demonstrate that GGF consistently performs more effectively than open-loop control. The degree to which it improves performance depends on the type and the extent of process uncertainty.

In simulation, several conclusions can be reached about the nature of the proposed control scheme. While the disparity between GGF and open-loop control

keeps increasing as the uncertainties in radius of curvature and droplet thickness increase, the disparity is less pronounced with respect to uncertainty in droplet placement. For during-print part deformation, the disparity between GGF and open-loop can potentially be infinite; in order to determine the efficacy of GGF for correcting during-print part deformations, the particular nature and degree must be considered.

In physical experimentation, the increased geometric fidelity is clear for GGF under uncertainty in assumed layer thickness, valve hold time, substrate shape, and tool pressure (Table 3.2). Additionally, the GGF technique did not require tuning of assumed layer thickness, which turned-out to be a vulnerability of the open-loop method without complete *a priori* knowledge of the printed components' characteristics.

Of the types of process uncertainties studied in this paper, it is reasonable to presume that traditional closed-loop feedback techniques (as discussed in "Prior Work") could compensate to some extent for uncertainty in radius of curvature, droplet thickness and possibly droplet placement since these errors occur at the process-variable level. However, none of the techniques would be able to address during-print part deformations, such as those caused by melting, vibration or substrate shift since this occurs at the whole-part geometry level. GGF has an enhanced ability to detect high-level errors and is able to address all of these errors, in addition to others, because it "closes the loop" on a higher level. Instead of *monitoring* low-level process variables such as temperature or single droplet shape, GGF directly monitors the whole-part geometry.

Table 3.2. Summary of RMS surface error for physical experiments.

	Open-Loop RMS Surface Error (mm) ± Standard Error [n=3]	RMS Surface Error Normalized to Max. Part Height (%)	Local-GGF RMS Surface Error (mm) ± Standard Error [n=3]	RMS Surface Error Normalized to Max. Part Height (%)
No Induced Process Uncertainty (without complete a priori knowledge)	1.98 ± 0.26	40	0.59 ± 0.19	12
No Induced Process Uncertainty (with complete a priori knowledge)	0.58 ± 0.22	12	Not Applicable	
Variation in Valve Hold Time	1.33 ± 0.37	27	0.69 ± 0.26	14
Non-Flat Substrate	1.16 ± 0.24	23	0.36 ± 0.18	7
Reduced Deposition Tool Pressure	2.57 ± 0.83	51	0.34 ± 0.22	7

Another of GGF's advantages stems from the fact that it directly *manipulates* whole-part geometry. Unlike other techniques that manipulate low-level process variables, GGF directly manipulates overall part shape by iteratively determining locations of droplets. As a result of this direct manipulation, GGF is not reliant on particular models of the relationships between process variables and overall part shape. Also, there is an increased extent to which uncertainties can be handled due to the fact that the geometry is being directly manipulated on a higher, whole-part level. That is, if low-level process variables were being manipulated there is no guarantee that the overall part shape is controllable for all types of process errors (e.g., manipulation of envelope temperature will not necessarily be able to fix errors caused by vibration or evaporation, whereas manipulation of matter placement could).

While this approach has clear advantages in combating sources of uncertainty that operate on the whole-part level, it would require further investigation to determine whether this approach is more effective at handling low-level process uncertainties, as compared to existing feedback control techniques. While the proposed approach has a lesser dependence on modeling the underlying process physics (which is an important advantage), further investigation would still be required to analyze the specific cost/benefit landscape.

While a drop-on-demand approach was used in this paper because it is naturally suited to GGF's iterative decision making, continuous stream material deposition systems could also be used with GGF. However the material flow would have to be conceptually discretized; for example, a Fused Deposition Modeling (FDM) system's polymer stream could be virtually grouped into distinct *material packets*.

FUTURE WORK

Future work will focus on increasing the complexity of the scoring heuristics to improve GGF performance for specific types of errors. For example, height growth rate terms could be included in the scoring heuristic to give priority to regions of the printed part that are deforming the fastest. Also, surface gradient terms could be included to allow the GGF scheme to prevent the printing of features that are too steep to remain structurally stable.

Additionally, we wish to explore the possibility of creating hybrid control approaches in which the flexibility of GGF is enhanced by usage of some low-level process variable information. While some low-level process variables are related to geometry in very complex manners, other low-level process variables are very well understood. Using knowledge of these stable low-level process variables and their

114

relationships to overall part-geometry, perhaps the GGF control scheme could be further improved.

GGF is an approach to implementing robust geometric feedback control in SFF systems. The technique yields benefits over open-loop and existing closed-loop control schemes, for a wide range of process uncertainties. The technique can be specialized for specific types of uncertainties by using more complex scoring heuristics, or GGF can be generalized for implementation in nearly any SFF technique. GGF has the potential to enable SFF to be conducted in unpredictable environments with unreliable materials, and to be applied to novel applications for which the parametric landscape is not easily modeled or controlled.

REFERENCES

[1]   M. P. Bodiford, S. D. Gilley, R. W. Howard, J. P. Kennedy, and J. A. Ray, "Are we there yet?… developing in situ fabrication and repair (ISFR) technologies to explore and live on the Moon and Mars," *First Space Exploration Conference: Continuing the Voyage of Discovery*, Orlando, Florida, 2005, pp. 1-7.

[2]   H. Lipson, "Homemade: the future of functional rapid prototyping," *IEEE Spectrum*, May, 2005.

[3]   M. R. Boddu, R. G. Landers, and F. W. Liou, "Control of laser cladding processes for rapid prototyping–a review," *Twelfth Annual Solid Freeform Fabrication Symposium*, Austin, Texas, 2001, pp. 460–467.

[4]   K. Cooper, R. Crocket, and F. Roberts, "Free form fabrication in space," in *42nd AIAA Aerospace Sciences Meeting*, Reno, Nevada, 2004.

[5]   E. Malone and H. Lipson, "Functional freeform fabrication for physical artificial life," *Ninth International Conference on the Simulation and Synthesis of Living Systems*, Boston, Massachusetts, 2004, pp. 100-105.

[6]   E. Whitney, "Advances in rapid prototyping and manufacturing using laser-based solid free-form fabrication," in *The Handbook of Advanced Materials*, Oak Ridge, TN: John Wiley & Sons, 2004, pp. 611-631.

[7]   L. Sun, K. J. Jakubenas, J. E. Crocker, S. Harrison, L. L. Shaw, and H. L. Marcus, "In situ thermocouples in macro-components fabricated using SALD and SALDVI techniques," *Materials and Manufacturing Processes,* vol. 13, pp. 909-919, 1998.

[8]   F. Pérès and D. Noyes, "Envisioning e-logistics developments: Making spare parts in situ and on demand state-of-the-art and guidelines for future developments," *Computers in Industry,* vol. 57, pp. 490-503, 2006.

[9]   D. L. Cohen, E. Malone, H. Lipson, and L. J. Bonassar, "Direct freeform fabrication of seeded hydrogels in arbitrary geometries," *Tissue Engineering,* vol. 12, pp. 1325-1335, 2006.

[10]   K. R. Vaidyanathan, "Functional metal, ceramic, and composite prototypes by solid freeform fabrication," *JOM Journal of the Minerals, Metals and Materials Society,* vol. 52, pp. 30-40, 2000.

[11]   E. Malone, K. Rasa, D. L. Cohen, T. Issacson, H. Lashley, and H. Lipson, "Freeform fabrication of zinc-air batteries and electromechanical assemblies," *Rapid Prototyping Journal,* vol. 10, pp. 58-69, 2004.

[12] N. E. Fedorovich, J. Alblas, J. R. de Wijn, W. E. Hennink, A. J. Verbout, and W. J. A. Dhert, "Hydrogels as extracellular matrices for skeletal tissue engineering: state-of-the-art and novel application in organ printing," *Tissue Engineering,* vol. 13, pp. 1905-1925, 2007.

[13] K. M. B. Taminger, R. A. Hafley, and D. L. Dicus, "Solid freeform fabrication: An enabling technology for future space missions," *2002 International Conference on Metal Powder Deposition for Rapid Manufacturing*, San Antonio, Texas, 2002, pp. 51-60.

[14] D. Hu, H. Mei, and R. Kovacevic, "Improving solid freeform fabrication by laser-based additive manufacturing," *Proceedings of The Institution of Mechanical Engineers Part B: Journal of Engineering Manufacture,* vol. 216, pp. 1253-1264, 2002.

[15] H. Derouet, L. Sabatier, F. Coste, and R. Fabbro, "Process control applied to laser surface remelting," *ICALEO'97*, 1997, pp. 71-77.

[16] J. Mazumder, A. Schifferer, and J. Choi, "Direct materials deposition: designed macro and microstructure," *Materials Research Innovations,* vol. 3, pp. 118-131, 1999.

[17] C. Doumanidis and E. Skordeli, "Distributed-parameter modeling for geometry control of manufacturing processes with material deposition," *Journal of Dynamic Systems, Measurement, and Control,* vol. 122, pp. 71-77, 2000.

[18] C. Doumanidis and Y.-M. Kwak, "Geometry modeling and control by infrared and laser sensing in thermal manufacturing with material deposition," *Journal of Manufacturing Science and Engineering,* vol. 123, pp. 45-52, 2001.

[19] M. J. Lovelady and J. D. Watts, "Closed loop feedback for continuous mode materials jetting," *IEEE/CPMT International Electronic Manufacturing Technology Symposium*, Austin, Texas, 1999, pp. 189-195.

CHAPTER 4: ADDITIVE MANUFACTURING FOR *IN SITU* REPAIR OF OSTEOCHONDRAL DEFECTS[*]

ABSTRACT

Tissue engineering holds great promise for injury repair and replacement of defective body parts. While a number of techniques exist for creating living biological constructs *in vitro*, none have been demonstrated for *in situ* repair. Using novel geometric feedback-based approaches and through development of appropriate printing-material combinations, we demonstrate the *in situ* repair of both chondral and osteochondral defects that mimic naturally occurring pathologies. A calf femur was mounted in a custom jig and held within a robocasting-based AM system. Two defects were induced, one a cartilage-only representation of a grade IV chondral lesion and the other a two-material, bone and cartilage fracture of the femoral condyle. Alginate hydrogel was used for repair of cartilage; a novel formulation of Demineralized Bone Matrix (DBM) was used for bone repair. Repair prints for both defects had mean surface errors less than 0.1 mm. For the chondral defect, 42.8±2.6% of the surface errors were within a clinically acceptable error range, however, with 1 mm path planning shift, an estimated ~75% of surface points could likely fall within the benchmark-envelope. For the osteochondral defect, 83.6±2.7% of surface errors were within clinically acceptable limits. In addition to implications for minimally invasive additive manufacturing (AM)-based clinical treatments, these proof-of-concept prints are some of the only *in situ* demonstrations to date, wherein the substrate geometry was unknown *a priori*. The work presented herein demonstrates *in situ* AM, suggests potential biomedical applications, and also explores *in situ*-specific

[*] Daniel L. Cohen[1], Jeffrey I. Lipton[1], Lawrence J. Bonassar[1,2], Hod Lipson[1,3]; [1]Cornell University, Mechanical and Aerospace Engineering, Ithaca NY; [2]Cornell University, Biomedical Engineering, Ithaca NY; [3]Cornell University, Computing and Information Science, Ithaca NY.

issues, including geometric feedback, material selection, and novel path planning techniques.

INTRODUCTION

Tissue engineering (TE) has the potential to fundamentally change medical practice by addressing donor supply and organ rejection issues. In particular, TE has been demonstrated for creation of living cartilage[1-8] and bone[9-10] constructs in anatomical shapes. Various techniques for achieving geometric complexity have been employed, including: layering of cells[11], layering of cell-seeded hydrogels[12-13], casting of seeded hydrogels onto complex surfaces[14], seeding of molded porous scaffolds[15], and injection molding of seeded hydrogels[16]. None of these techniques, however, enables fabrication of constructs with multi-axial spatial heterogeneities, including different cell types or densities. Furthermore, these techniques require custom tooling, and consequently, achieving patient-specific shapes is non-trivial and sometimes prohibitively challenging. One approach that overcomes these limitations is additive manufacturing (AM) of cell-seeded hydrogels. Toward this end, a number of techniques have recently emerged, including AM of: photocrosslinkable hydrogels (PEG[17-19]), thermoreversible gels (gelatin[20-25], pluronic[26], collagen[21,26-27]), and post-deposition ionically crosslinked alginate hydrogel[24-25,28].

These AM techniques, however, have only been demonstrated for fabrication of tissue engineering constructs *in vitro*. That is, none of these techniques have been employed *in situ*[29-31] directly on a wound site. Moreover, these approaches are not amenable to *in situ* AM because they rely on external environmental cues, such as UV light, temperature, and calcium availability, to initiate phase change after deposition. For *in situ* applications, the environment cannot necessarily be controlled and introduction of precise external environmental cues within the body is likely

119

unfeasible. One technique, however, deposition of alginate hydrogel with ionic

crosslinking initiated prior to deposition[32], does not rely upon external cues for phase

change after deposition, and thus, is compatible with *in situ* applications. In addition

to finding compatible materials, other issues needed to be addressed to enable *in situ*

repair, such as imaging, registration, and path planning.

Even beyond the medical context, *in situ* AM has only rarely been

demonstrated, and never in a generalized fashion without *a priori* substrate-shape

information, as conducted herein. *In situ* AM of thermocouples and wire networks has

been demonstrated onto pre-existing objects of complex geometry, however, in both of

these cases the geometry was known, i.e. hard-coded into the planning sequence.

Generalized *in situ* AM, although potentially powerful, has likely been hampered by

the lack of pre-existing geometric feedback-based AM techniques/algorithms. Prior to

this work, geometric feedback has only been used in limited cases, such as stabilizing

AM process parameters[33-35] and individual droplet shapes[36]. However, geometric

feedback had never been used for ascertaining substrate geometry in order to print

onto pre-existing objects of unknown shape. Furthermore, no techniques had been

developed to handle *in situ*-specific challenges, including path planning, materials

formulation, image processing, and geometric fidelity characterization.

In the work presented herein, we demonstrated the *in situ* repair of a cylinder-

shaped cartilage (i.e. chondral) defect as well as a geometrically complex two-material

bone and cartilage (i.e. osteochondral) defect.   These defects were created on a calf

femur to mimic naturally occurring pathologies. The chondral defect approximated a

cylindrical core created by surgeons during the OATS (Osteoarticular Transfer

System) procedure in order to treat a Grade IV chondral lesion. The second defect

used herein, the osteochondral defect, approximated a severe complex freeform

fracture of the femoral condyle in which both bone and cartilage tissues were damaged.

In these cases, the defect-induced femur served as the printing substrate and was mounted in a custom jig within the AM machine. Alginate hydrogel, with ionic crosslinking initiated prior to deposition[32], was used for repair of cartilage; bone was repaired with a novel formulation of Demineralized Bone Matrix (DBM). AM planning was conducted by CT scanning the bone before and after defect creation, differencing of the two images, and subsequently raster pathing the resultant geometry. Feature-based image registration was conducted to align the printing substrate within the printer. Herein we demonstrate materials, hardware modifications, CT imaging, and registration for *in situ* repair of both chondral and osteochondral defects.

MATERIALS AND METHODS

Alginate Hydrogel Preparation

Alginate hydrogels were prepared for printing using techniques based on those described previously[32]. The alginate solution was created by mixing low-viscosity, high G-content non-medical grade LF10/60 alginate (FMC Biopolymer, Drammen, Norway) with PBS at a concentration of 20 mg/mL. The $CaSO_4$ crosslinker solution was created at a concentration of 10 mg/mL in PBS. The alginate and crosslinker solutions were combined in a 2:1 ratio and mixed 150 times through a stopcock at 1 Hz. The mixed alginate hydrogel was loaded into a ten milliliter syringe (EFD Inc., East Providence, RI) and allowed to cure for at least 10 minutes before use in any printing or experimentation.

Demineralized Bone Matrix (DBM) Paste Preparation

The basis of the printable bone paste was demineralized bone matrix (DBM) in a purified powdered gelatin carrier (BioSet™ DBM; Regeneration Technologies Inc., Alachua, FL). The manufacturer specifies 38% DBM-gelatin powder in water by weight. The paste is prepared by mixing the DBM-gelatin powder with water through a two-port Luer-lok connector by walking the syringes back-and-forth in unison ten times. Even though the largest standard diameter deposition tip of the AM machine (1.50 mm diameter × 12 mm long straight barrel) was used for initial material calibration, the DBM paste was still too viscous to be extruded. If the tip were any larger, even though it would reduce the associated extrusion force, the resultant print resolution would be inadequate for repair of millimeter scale defects.

We conducted a material tuning experiment in order to find an appropriate powder-water composition that was low-viscosity enough for extrusion but high-viscosity enough for the printed material to retain its shape post-deposition. Three formulations were tested: the manufacturer-specified formulation (38% DBM-gelatin powder in water by weight) and two others with higher concentrations of water (34% and 30% DBM-gelatin powder in water by weight). Three properties were measured for each tested formulation, including minimum extrusion force, sag and work life.

The minimum extrusion force was the amount of force required to induce material flow through the deposition tip. The AM machine's material bay (i.e. a disposable syringe, see "Additive Manufacturing System") was loaded with paste, held vertically on a digital scale and the force at which flow began was recorded. Sag was determined by manually extruding 10 mm tall, 6 mm diameter cylinders and measuring the height difference over the first 15 minutes. Work life was determined by measuring the elapsed time before the previously determined minimum extrusion force no longer induced paste flow.

Harvest and Preparation of the Femoral Printing Substrate

      The printing substrate for the experiments presented herein was the distal end of a bovine femur. The leg of a sacrificed 1-3 day old calf was dissected to isolate the femur. Muscular and connective tissues were removed while maintaining the geometric integrity of the femoral condyles. The isolated femur was placed in boiling water for 20 minutes in order to preserve the bone. The femur was then cut halfway down the shaft and vertically set in molding plaster (U.S. Gypsum Company, Chicago, IL) within of a PVC flange (Figure 4.1). The bone-flange assembly was mounted to a removable acrylic tray and inserted into the printer.
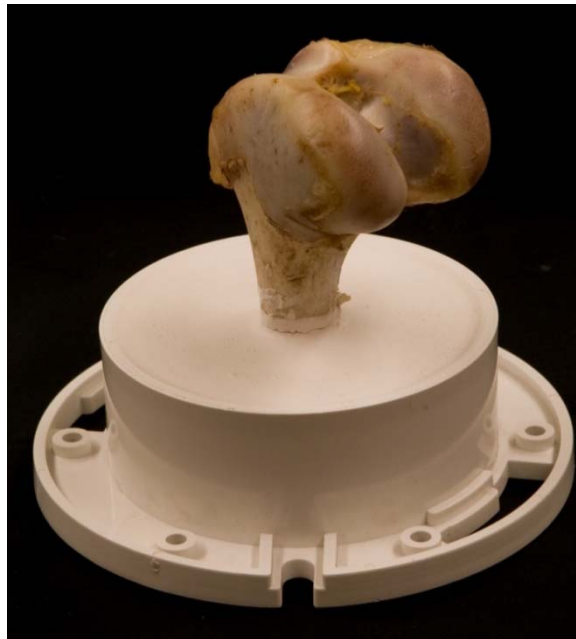
Figure 4.1. Femoral printing substrate. The femur was case vertically into a plastic pipe fitting. The pipe fitting screwed directly into the printer base plate.

CT Imaging of the Femoral Printing Substrate

      CT images were collected on a 16-slice Toshiba Aquilion LB. Volumetric data was collected in 0.5 mm segments, and reconstructed using standard Toshiba-unit bone and soft tissue algorithms (Figure 4.2).
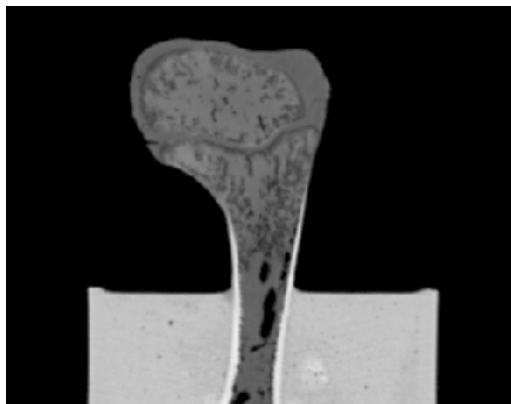
Figure 4.2. CT image of the femur and its mounting jig.

Creation of Defects in the Femoral Condyles

Defects were created on the surface of the femoral printing substrate by a veterinary orthopaedic surgeon to mimic pathological cases. Two of these defects were used for printing experimentation (Figure 4.3). The first induced defect, herein referred to as "Case One" or the "Chondral Defect," simulated a grade IV lesion of the articular cartilage on the medial femoral condyle (Figure 4.4). A grade IV lesion is one in which the tear of the cartilage goes all the way down to the underlying bone surface, but does not extend into the bone. In order to create this defect, a 16 mm diameter circular punch was used to core out the condyle ~4 mm downward to the bone surface.

The second defect, herein referred to as "Case Two" or the "Osteochondral Defect," was a first-order approximation of a fracture in which a portion of the lateral femoral condyle sheared off. In the severe fracture scenario, the cartilage cap breaks off as well as some of the underlying bone tissue. This two-tissue defect was created by using a scalpel to slice transversely to the condyle. The cut was made ~4 down from the distal end of the condyle and extended ~1 mm down into the underlying

bone. To increase the severity of the simulated injury, the bone tissue was further

resected with a curette by carving out a 4 mm deep dome-shaped cavity.
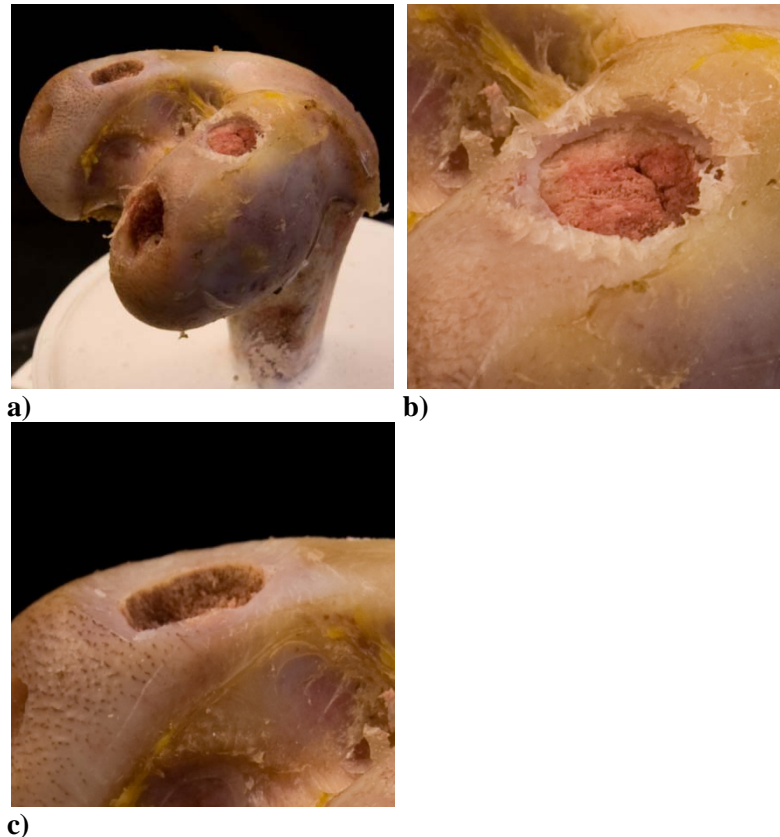
Figure 4.3. Femoral printing substrate with induced osteochondral defects. (a) Overview of four defect sites. Two of these sites were used for experimentation. (b) Close-up view of chondral defect site. A cartilage disc was removed exposing the underlying bone surface. (c) Close-up view of osteochondral defect site. A bone sliver was removed and the underlying bone was also cored-out.

Additive Manufacturing System

     A Fab@Home open-source, open-architecture additive manufacturing system

was used for the experiments presented herein[37] (Figure 4.4). This system, which was

designed and deployed by our lab, comprised a laser cut acrylic chassis with a three-

axis gantry motion system. Each axis was belt-driven and actuated by a stepper motor

(Haydon Switch & Instruments, Waterbury, CT). Communication and motion was

coordinated by a USB-interfaced electronic control board based on the Olimex LPC-H2148 microcontroller. The open-source control software was written by our lab, and along with the hardware design files, are freely available at www.fabathome.org.
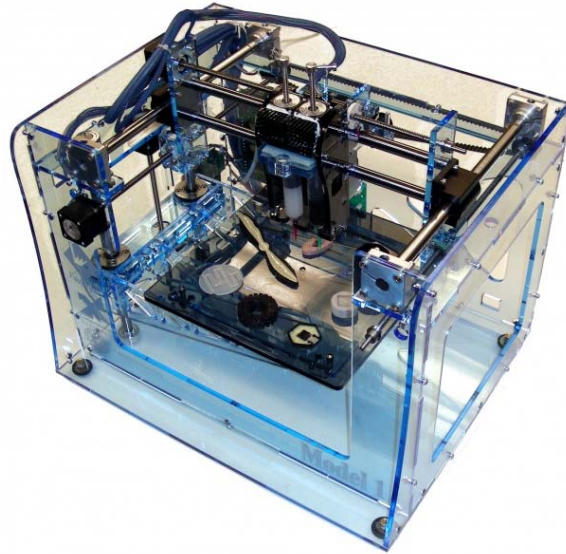
Figure 4.4. Fab@Home additive manufacturing system. The Fab@Home AM system is an open-source, open-architecture platform. The material-filled syringes insert into the deposition tool, and a stepper motor pushes upon the plunger to extrude material through the Luer-lok tip.

The standard Fab@Home design was modified in order to allow for easy swapping of the printing substrate. The Fab@Home's traditional base was upgraded to a custom hot-swappable cartridge-style base plate (Figure 4.5). Acrylic trays, 190 mm by 225 mm, were placed in the recess of the Fab@Home's modified base plate and secured with an interference fit. This feature is an important adaptation for *in situ* AM applications as it enables parts to be removed for inspection and replaced without the loss of spatial registration.
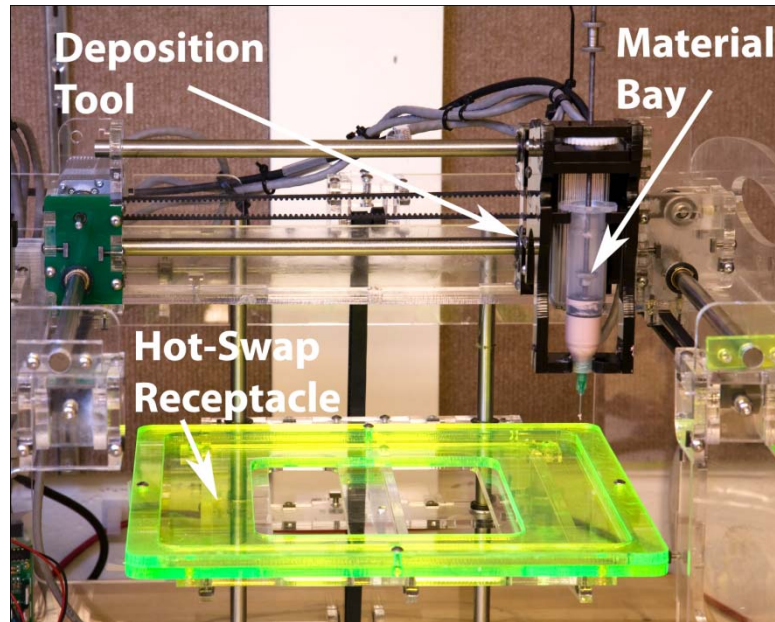
Figure 4.5. The standard base plate was modified to accommodate hot-swappable snap-in trays. The easy removal of printing parts is an important feature for enablement of *in situ* printing. Once the part is registered, if the machine needed to be serviced, the removable tray allowed for service without registration loss.
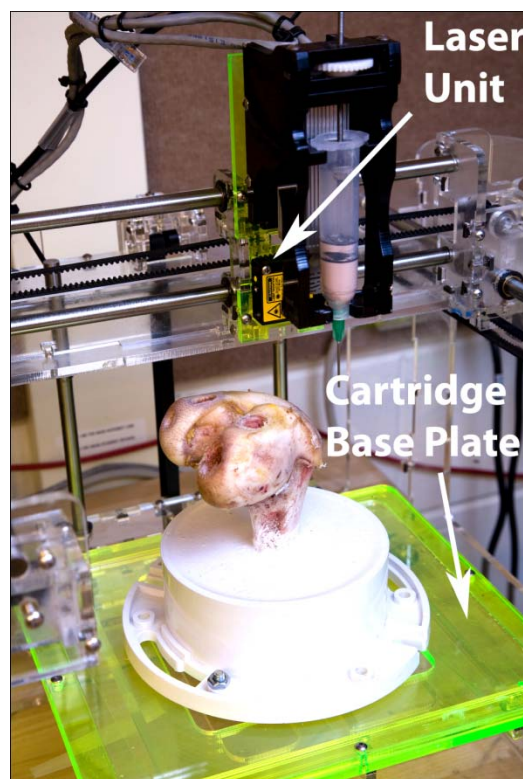
Figure 4.6. The laser distance sensor was mounted behind the deposition tool.

Another modification was made to accommodate a laser distance sensor (OADM12 Laser; Baumer Ltd., Southington, CT). The laser sensor was mounted in between the Y-axis carriage and the deposition tool (Figure 4.6). This sensor had a 104 mm range and a distance measurement resolution of 0.12 mm. The laser was used for measuring the geometric fidelity of printed constructs post-print by scanning the printer workspace.

Path Planning for *In Situ* AM

The CT images of the femoral printing substrate were used for AM path planning. One CT scan before the creation of the defects, and a second scan afterwards, were imported in Mimics V12 (Materialise Group, Leuven, Belgium) as DICOM files and converted into 3D solid models. More specifically, during this conversion, the bone and cartilage tissues were isolated by creating a mask that thresholded intensity values between -906 and 3071 Hounsfields, which corresponded to the tissues of interest. These values were determined by iteratively modifying the intensity thresholds and ensuring complete inclusion of the target constructs while exclusion of background noise, such as out-of-scope tissues and environmental features. To further remove image noise, a region growing algorithm was employed where the femur's centroid served as the seed location and neighboring voxels within the threshold intensity range were included in the data set. The thresholded, region-grown mask was then converted to a 3D mesh, which was exported as an STL file.

A model of the defect was created by applying a Boolean subtraction operator to the "before" and "after" STL files. This "differenced" STL file was imported into the Fab@Home's open-source control software in order to create the path plan of the target print geometry. A layer-wise raster path planning algorithm was employed. Registration of the femoral printing substrate within the printer was achieved by

128

setting the 3D model's X-Y origin to the center of a known feature, in this case, the (+X,+Y) flange mounting bolt. During each print, the laser beam was used to register the coordinate systems by aligning the beam with the known feature (i.e. the bolt) and adding the known offset X-Y between the laser and deposition tip.

Geometric Fidelity Characterization

Geometric fidelity was both qualitatively and quantitatively characterized. During visual inspections, key observed characteristics included surface texture, similarity of the overall shape compared to the intended geometry, and presence of point defects such as missing material. In addition to visually inspecting constructs, each printed object was laser scanned (0.3 mm X-Y resolution; 0.12 mm height resolution). The resultant height data was converted into a 3D solid in Studio V11 (Geomagic Inc., Research Triangle Park, NC) and exported as an STL file. The file was then imported into Qualify V11 (Geomagic Inc., Research Triangle Park, NC) which performed 3D geometric fidelity calculations, comparing the printed geometry to the intended target shape as specified by the CT image of the pre-damage femur. The error calculated was the 3-dimensional error between the surface of the actual geometry and the intended geometry (nearest point between the surfaces). Note that all values in this paper are reported as mean ± standard deviation.

Benchmarking – Determination of Clinically Allowable Geometric Errors

In order to place the measured geometric errors within a clinical context, the repair-print errors were compared to allowable surgical tolerances established in prior literature. Each defect's measured geometric error was compared to tolerances of the medical procedure that best matched the nature of that particular defect. To this end, repair-prints of the chondral defect, "Case One," were compared to tolerances

established for the OATS surgical procedure, in which cartilage graft-plugs are implanted into manufactured cylindrical defects. Repair-prints of the osteochondral defect, "Case Two," were compared to tolerances established for meniscal replacement procedures. Since the meniscus is in direct contact with the condyle (which was repaired in "Case Two"), established tolerances for the sizing of replacement menisci have relevance to benchmarking geometric fidelity for condyle repair.

Several studies have addressed the clinically acceptable geometric tolerances for implantation of cartilage graft-plugs in human OATS procedures on the knee[38-40] and ankle[41-42]. While some surgeons implant the grafts flush with the surface of the surrounding host tissue[39], others prefer to intentionally implant the graft approximately 1 mm above the height of the surrounding host cartilage surface[38,41-42]. Although there is no universally accepted graft height-offset, at least one study suggests that as long as the graft is between 0 mm and 2 mm above the surface of the host tissue, the graft is considered within "acceptable" geometric tolerances[41]. While "proud" grafts (i.e. above the host surface) are acceptable, many studies have concluded that grafts implanted beneath the surface of the host tissue are unacceptable as they lead to unfavorable contact forces within the joint[38-40,42]. Therefore, for the purposes of benchmarking the "Case One" repair-print errors, surface points between 0 mm and 2 mm above the host tissue are considered within an acceptable margin. In addition to reporting the mean geometric error for each sample, the percentage of surface points within the 0 mm to 2 mm envelope is calculated, as well as the percentage of surface points within the -1 mm to +1 mm envelope.

Separate criteria were used for benchmarking the geometric errors of the "Case Two" repair-prints. To date, no studies have determined acceptable geometric tolerances for freeform condyle repair. However, the condyle is in direct contact with

the meniscus, and data does exist for acceptability of geometric errors in the meniscus[43-44]. It is assumed herein that geometric tolerances of the meniscal surface are indicative of acceptable tolerances of the condyle since the two parts share the very same interface. That is, if an X mm error is allowable on the meniscal side of the meniscal-condyle interface, then similarly, an X mm error is allowable on the condyle side of the meniscal-condyle interface.

More specifically, Dienst *et al* determined that meniscal grafts placed within the human knee closely reproduce normal contact forces as long as the replaced meniscus is within ±10% of the original meniscus geometry[43]. In order to determine how much a 10% error translated to at the meniscal-condyle interface, basic geometric principles were employed. The cross-sectional geometry of the meniscus was assumed to be a triangle (Figure 4.7).

Average human meniscus medio-lateral width, Wn, is 11.9±2.7 mm[44]. Within the allowable 10% margin established by Dienst *et al*, the range of allowable meniscus width is 10.7 mm (Wu) to 13.1 mm (Wo). Similarly, average meniscus height, Hn, is 7.1±1.8 mm[44], yielding an allowable meniscus height of 6.4 mm (Hu) to 7.8 mm (Ho). In order to determine the allowable geometric deviation of the meniscal-condyle interface, one must calculate the difference in interface position, m, between the largest and smallest allowable menisci (Figure 4.7 and eq. 1).
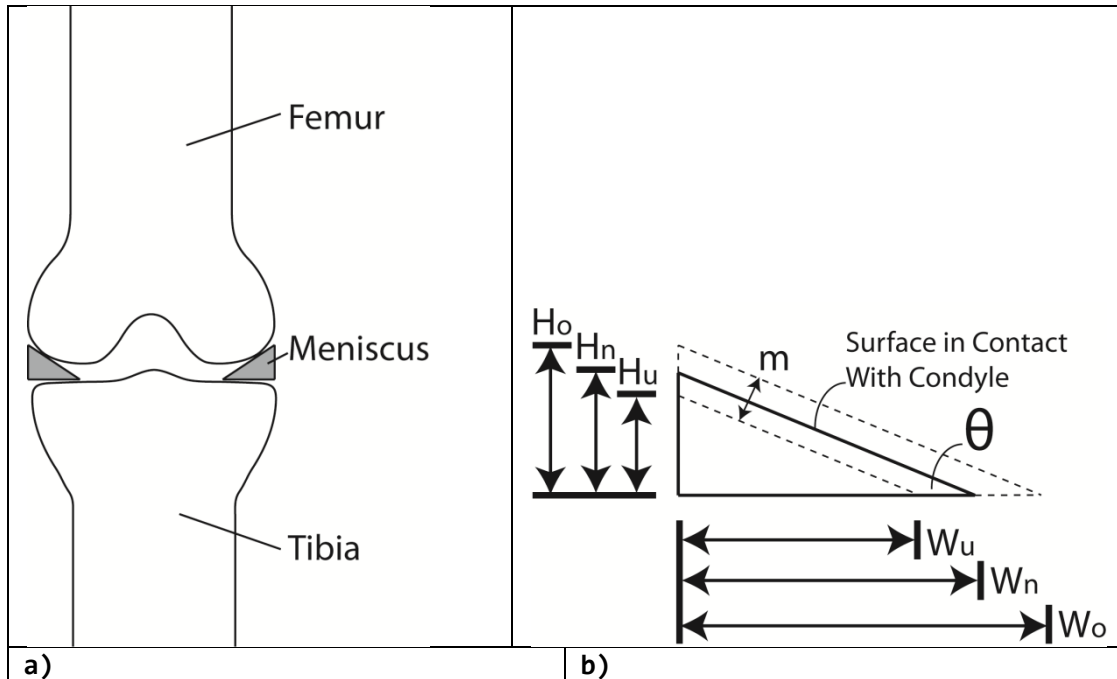
Figure 4.7. Drawings of femoral condyle and meniscus. (a) Femur and tibia with triangular approximation of meniscus in joint. (b) Normally sized meniscus [solid line] with over- and under-sized meniscus [dotted lines]. The allowable size variation in the width and height of the meniscus translates into the allowable meniscal-condyle interface deviation, *m*. Note that *Hn*, *Hu*, and *Ho*, are the normal height, under-sized height, and over-sized height, respectively. *Wn*, *Wu*, and *Wo*, are the normal cross-sectional mediolaterial width, under-sized width, and over-sized width, respectively.

Equation 4.1. Calculation of acceptable geometric deviation of the meniscal-condyle interface

$$Wn = 11.9 \pm 2.7 \ mm \quad Wo = 13.1 \ mm \quad Wu = 10.7 \ mm$$
$$Hn = 7.1 \pm 1.8 \ mm \quad \ \ Ho = 7.8 \ mm \quad \ \ Hu = 6.4 \ mm$$

$$m = \cos \emptyset \ (Ho - Hu) = \left(\frac{Wn}{\sqrt{Wn^2 + Hn^2}} \right) (Ho - Hu) = 1.2 \ mm$$

Based on the human meniscus dimensions above, the maximum allowable geometric deviation of the meniscal-condyle interface (i.e. the allowable surface error of the condyle), is an absolute range of 1.2 mm, or ±0.6 mm relative to the intended surface (eq. 1). Based on this reasoning, the geometric fidelity criterion for "Case Two," is ±0.6 mm relative to the intended surface.

RESULTS

Tuning of DBM Paste Formulation

Three different formulations of DBM paste were tested for their printing properties (n=5): 38%, 34% and 30% DBM-gelatin powder in water by weight. The 38% formulation had a minimum extrusion force of 3800±450 grams of force (note: values reported herein are mean ± standard deviation). The 34% and 30% formulations had substantially lower minimum extrusion forces of 1900±180 and 740±80 grams of force, respectively. Only the 34% and 30% formulations fell within the Fab@Home's deposition force limit of ~2500 grams of force.

The 38% and 34% formulations exhibited similar sag characteristics, of 3±2% and 2±2% of the initial part height, respectively. The 30% paste however, exhibited drastically greater sag at 25±8%. While the sag was recorded over 15 minutes, the majority of the sagging (most noticeably for the 30% formulation) occurred within the first 30 seconds after extrusion.

The work life of the 38% formulation was two minutes. The formulations with higher concentrations of water exhibited extended work lives. The 34% paste had a work life of 15 minutes and the 30% paste exhibited a work life of approximately 25 minutes.

Table 4.1. DBM paste characteristics. Printing characteristics of the DBM paste for three difference formulations with different concentrations of water, n=5. The pastes were assessed for minimum extrusion force, sag and work life.

Concentration of DBM-Gelatin Powder in Water by Weight (%)	Minimum Extrusion Force (grams)	Sag (% of initial height)	Work Life (minutes)
38	3800±450	3±2	2
34	1900±180	2±2	15
30	740±80	25±8	25

The 34% DBM-gelatin powder in water by weight formulation was selected for the subsequent experiments (Table 4.1). This composition yielded the only acceptable combination of minimum extrusion force and material sag. The 38% formulation exceeded the Fab@Home AM system's maximum deposition tool force, while the 30% formulation exhibited unacceptably poor sag characteristics.

Case 1: Chondral Defect

The CT scans from before and after the defect creation were processed and differenced in order to create a model of the defect (i.e., the target printing geometry). This geometry was a cylindrical plug that matched the void present in the femoral condyle (Figure 4.8). The 3D model was path-planned, and the print was conducted five times to collect sufficient geometric fidelity data.

Alginate hydrogel was used as the ink for the repair of this cartilage-only defect. The gel was printed through a 0.84 mm inner diameter × 31 mm long tapered syringe tip (EFD Inc., East Providence, RI). The printing parameters for alginate were determined through separate calibration experiments in prior work[32]. The key parameters were 0.8 mm path width, 0.71 mm path height, and 10 mm/s deposition tool traverse rate.

After each print, the construct was visual inspected to qualitatively assess geometric fidelity. The printed alginate hydrogel had a smooth surface texture. Furthermore, the printed geometry closely matched the intended geometry as specified by the CT scan before-after differencing process. The sides of the printed plug were congruent with the perimeter of the induced chondral defect. Also, the top surface of the printed construct matched the contour of the condyle (Figure 4.8).
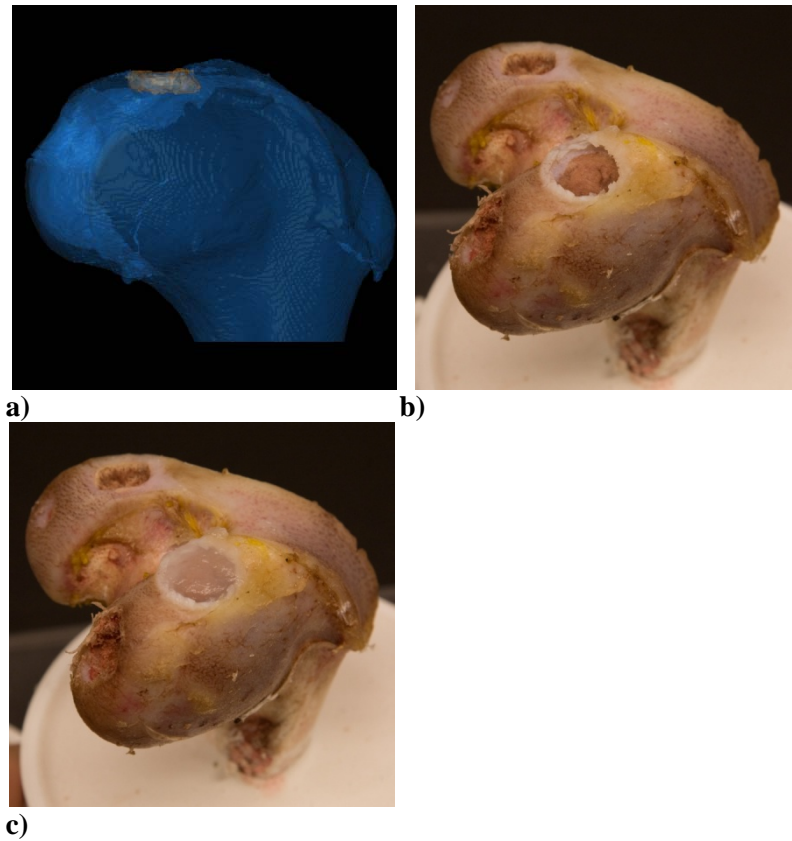
Figure 4.8. Repair of chondral defect. (a) CT scan of the femur with the chondral defect on the top surface. (b) Chondral defect before repair. (c) Chondral defect after repair.

The average of the mean error was 0.0±0.2 mm, n=5 (Figure 4.9). Across the five prints, 42.8±2.6% of the surface points were within the 0 mm to +2.0 mm error envelope. However, 75.6±7.6% of the surface points fell between -1.0 mm and +1.0 mm.
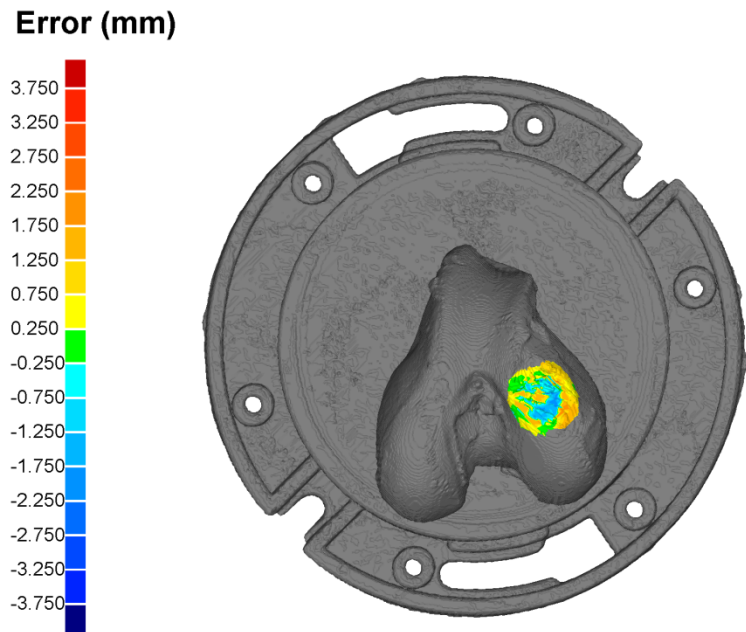
Figure 4.9. Top-view error plot of chondral defect. The laser scan of the printed surface was compared to the pre-damage CT scan reference geometry. Colors correspond to error magnitude.

Case 2: Osteochondral Defect

As in Case One, the CT scans from before and after the defect creation were processed and used for path planning. Unlike Case One, however, the Case Two defect comprised two materials: bone and cartilage. Alginate was again used for cartilage repair, however, the DBM paste was used for the bone portion of the defect.

During path planning, the 3D mesh of the target osteochondral construct was segmented into separate bone and cartilage geometric meshes through manual slicing. This manual slicing process was guided by the CT data which delineated between the two tissues according to the image intensities.
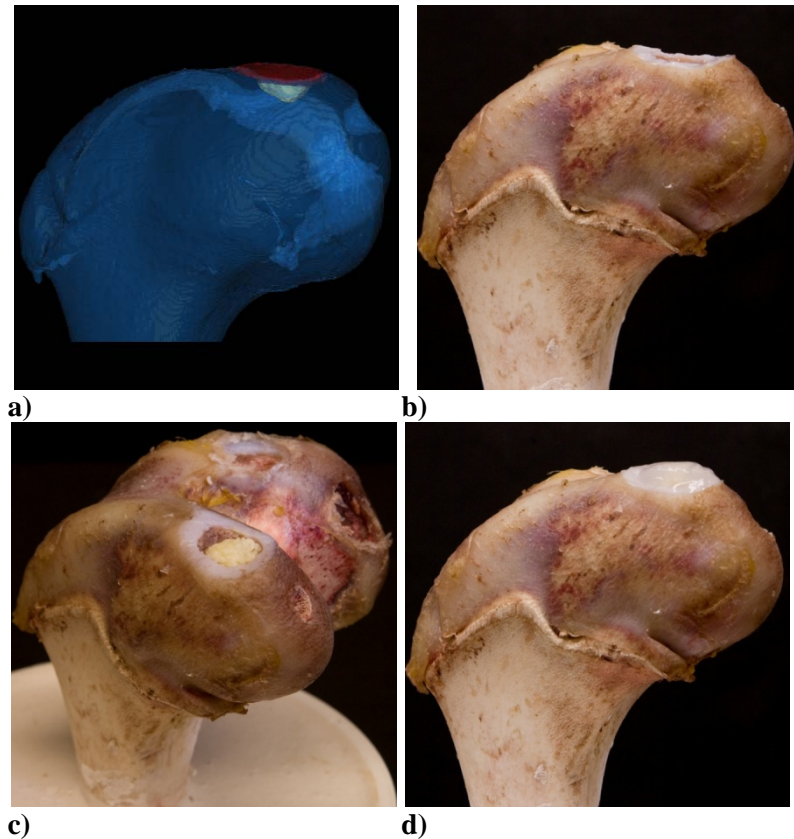
Figure 4.10. Repair of the osteochondral defect. (a) CT scan of the femur and the two-material osteochondral defect. The cartilage portion of the defect is highlighted in red and the bone portion in yellow. (b) Unrepaired osteochondral defect. (c) Partially repaired osteochondral defect where the bone portion has been printed. (d) Fully repaired osteochondral defect where the hydrogel is visible and the DBM lays beneath.

The resultant print geometry was a dome-shaped bone plug covered by a cylindrical cartilage cap (Figure 4.10). As before, the alginate hydrogel was printed through a 0.84 mm inner diameter × 31 mm long tapered syringe tip (EFD Inc., East Providence, RI). The same printer parameters were used as in Case 1. The DBM paste was printed through a 1.50 mm diameter × 12 mm long straight-barrel tip (EFD Inc., East Providence, RI), which as described above, was the largest tip that would still provide adequate print resolution. The key printer parameters for the DBM paste were 1.65 mm path width, 1.3 mm path height, and 10 mm/s deposition tool traverse

rate. These parameters were determined largely by the selected tip diameter. The

specific values were optimized iteratively by fixing the extrusion rate and sweeping

through a range of 1-25 mm/s tool traverse speed until continuous material streams

were produced. As in Case One, the print was conducted five times to collect

geometric fidelity data.

Since this print was an assembly of two constructs, the DBM portion of the

print was visually inspected mid-print (i.e., before the alginate deposition). The

printed bone construct had a rough surface texture. Its surface profile, however,

closely matched the intended surface contour of the substrate's bone tissue. The bone

construct was also laterally congruent with the walls of the bone cavity.
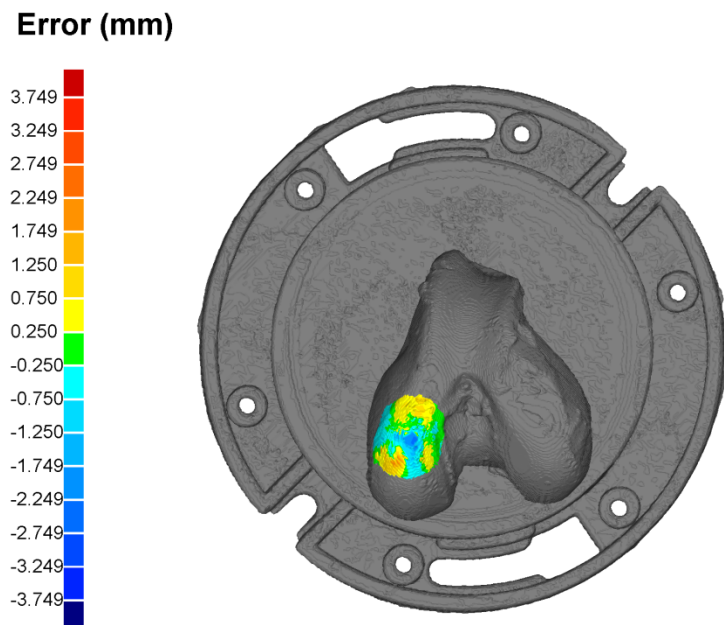
Figure 4.11. Top-view error plot of osteochondral defect. The laser scan of the printed surface was compared to the pre-damage CT scan reference geometry. Colors correspond to error magnitude.

The printed alginate hydrogel had a smooth surface texture and had a similar

geometric fidelity to the alginate prints in Case One. Again, the printed geometry

closely matched the intended geometry and the part was laterally congruent with the

defect boundaries. The contour of the 3D freeform alginate construct closely resembled the original pre-defect contour.

The average of the mean error was 0.1±0.1 mm, n=5 (Figure 4.11). Across the five prints, 83.6±2.7% of the surface points were within the -0.6 mm to +0.6 mm error envelope. Moreover, 92.8±3.1% of the points fell within ±1.25 mm of error.

DISCUSSION

The two repair-prints ("Case One" and "Case Two") both exhibited low geometric error in terms of the mean error. The chondral defect repair-prints ("Case One") and osteochondral defect prints ("Case Two") had mean errors of less than 0.1 mm. More specifically, the chondral defect had a mean error of 0.0±0.2 mm, and the osteochondral defect had a mean error of 0.1±0.1 mm. These mean errors both fell within the above-established clinical benchmarks of 0 mm to 2 mm for "Case One," and ±0.6 mm for "Case Two."

Upon comparing "Case One" chondral defects to clinical benchmarks, wherein grafts between 0.0 mm and +2.0 mm are considered acceptable[41], the mean errors fell within the acceptable envelope as noted above. However, in order to more completely analyze the potential efficacy of this technique, the spread of surface point errors must also be addressed. That is, 42.8±2.6% of the surface points were within the 0 mm to +2.0 mm error envelope. While this at first seems to be somewhat low benchmark-compliance, it should be noted that the print was not conducted with the benchmark in mind. In other words, the geometric path planning was executed with the intended geometry being the exact shape of the original cartilage. If the planning had artificially inserted additional layers to translate the parts upward 1 mm, the resulting printed constructs would have had mean errors of ~1 mm (still within the benchmark envelope), yet the spread of points would likely have remained the same. Given that

75.6±7.6% of the surface points fell between -1.0 mm and +1.0 mm, it can be assumed that if the geometry had been translated upward 1 mm prior to printing, a very similar portion of points would have fallen between the 0 to 2 mm benchmark. Under these assumptions, a benchmark compliance of approximately 75% can likely be achieved with proper pre-print planning.

Spread of the surface errors must also be assessed for "Case Two" osteochondral repair-prints. Based on the ±0.6 mm envelope[43], 83.6±2.7% of the surface errors fell within acceptable limits. Moreover, if the acceptable bounds were increased to ±1.2 mm, then 92.8±3.1% of the points were within range.

In addition to proposing a methodology for benchmarking *in situ* orthopaedic repair-printing, other *in situ*-specific issues were addressed. Perhaps the most critical consideration for *in situ* printing is what types of constraints the deposition techniques and/or materials require post-deposition. For example, stereolithography (SLA) and selective laser sintering (SLS) techniques are not amenable to *in situ* AM since it is not feasible to embed body parts within a liquid vat or powder bed, respectively. Even for techniques which are conceivably amenable, such as robo-casting and direct-writing, material selection must be made carefully. Materials that rely upon post-deposition external environmental cues for phase-change (e.g. temperature fluctuation[20-27], UV light [17-19], chemical exposure[24-25,28]) are not compatible with *in situ* AM since these cues cannot necessarily be reliably introduced within the body during a surgical procedure. For example, in-body AM cannot rely upon temperature change for phase-change of thermoreversible hydrogels[20-27] since the environmental temperature is dictated by the body and is uncontrollable. Instead, materials must be selected where the phase-change was initiated prior to deposition without the need for external cues, such as the pre-crosslinked-alginate[32] and DBM, used herein.

While alginate hydrogel has an established heritage for cartilage tissue engineering, we selected DBM for its relevance to bone repair. The novel formulation allows for successful extrusion through a syringe-based deposition tool, yet is geometrically stable after deposition. In order to better understand the efficacy of this approach from a biological perspective, further investigation must be conducted either in culture *in vitro* or perhaps *in vivo*; tissue integration, cell proliferation, and extracellular matrix production must all be studied since they have not yet been studied with these materials in this particular context.

Aside from biological considerations and implications of this work, the proof-of-concept work presented herein address pressing issues within the broader AM field; these prints are some of the only *in situ* AM demonstrations of any kind to date. *In situ* AM has been demonstrated for fabrication of thermocouples[30] and antennae on helmets[45]; these two examples fit the definition of "*in situ*" in that they were conducted on pre-existing parts of non-flat geometry. In these cases, however, there was no geometric feedback involved and the substrate geometry was hard-coded, and thus, known by the system *a priori*. More generalized *in situ* AM for unknown substrate shapes, based on geometric feedback, has only been conceptualized[29] but never demonstrated. Moreover, geometric feedback has only rarely been used for any purpose in AM. Several groups have employed geometric feedback for quality assurance[33-36,46], i.e., achieving high geometric fidelity despite process uncertainties, but in these cases they were not printing *in situ* nor accounting for unknown substrate shape. The bone repair-prints presented herein used CT-scan-based geometric feedback and novel differencing algorithms to conduct *in situ* prints wherein the complex substrate geometry was unknown *a priori*. Furthermore, we explored associated noise removal techniques, in particular, region growing, which was critical for successfully distilling useful geometric information from differenced medical

images. Another *in situ*-specific issue is registration of the printing substrate within the AM machine; we propose feature based registration assisted by a laser guide marker. Other possible techniques include automated feature extraction from a pre-print laser scan of the substrate which would be compared to unique features in the medical image data. We also demonstrated *in situ*-specific hardware modifications, such as a deposition-tool-mounted laser sensor and a hot-swappable cartridge-style base plate. These design features are important for both ascertaining geometric data and maintaining proper registration despite potential inspection-related part-removal.

As geometric feedback is harnessed for handling unknown substrate shapes and *in situ* printing is enabled, new paradigms will be created within AM[29]. Rather than replacing parts that have sustained geometrically complex damage, *in situ* AM could be used to salvage these parts. In the biomedical realm, as directly suggested by the proof-of-concept prints conducted herein, *in situ* AM could lead to less invasive clinical treatments. Small incisions could be made to insert a print-head, and in conjunction with CT/MR imaging, damaged body parts could be directly repaired.

It should be noted, that process uncertainty will also become more influential for *in situ* applications. That is, once the printer "comes to the part" and operates within the part's environment, it is now beyond the highly controlled environment of typical AM systems. In addition to unknown substrate geometry, other factors such as uncontrolled humidity, vibration and temperature could potentially lead to adverse effects on the geometric fidelity of the printed part. Thus, geometric feedback is not only important for ascertaining initial substrate geometry and directly enabling *in situ* AM, but also closed-loop techniques may prove critical for ensuring quality despite less controlled environments. The geometric feedback approaches for quality assurance[33-36,46], mentioned above, will likely become key enablers for the practical implementation of *in situ* AM. Also related to the notion of environmental

uncertainty, further investigation must be done to better understand the effect that loads that surrounding tissues would place on the repair-prints. Stronger materials and/or external patient fixation may be required for clinical implementation of the approach proposed herein.

Through careful selection of printing materials and techniques, novel AM planning sequences, and increasingly accessible imaging modalities, the stage is set for *in situ* to emerge as a new paradigm in AM. In-place repair of systems, ranging from complex machines to human bodies, will benefit from AM operating in the existing parts' own environments. Not only will complexly-damaged parts be able to be repaired instead of replaced, but new territories can be explored in toward less invasive repair.

REFERENCES

[1]   Y. Cao, J. P. Vacanti, K. T. Paige, J. Upton, and C. A. Vacanti, "Transplantation of chondrocytes utilizing a polymer-cell construct to produce tissue-engineered cartilage in the shape of a human ear," *Plastic and Reconstructive Surgery,* vol. 100, p. 297, 1997.

[2]   C. Ibarra, C. Jannetta, C. A. Vacanti, Y. Cao, T. H. Kim, J. Upton, and J. P. Vacanti, "Tissue engineered meniscus: a potential new alternative to allogeneic meniscus transplantation," *Transplantation Proceedings,* vol. 29, pp. 986-988, 1997.

[3]   S. H. Kamil, K. Kojima, M. P. Vacanti, L. J. Bonassar, C. A. Vacanti, and R. D. Eavey, "In vitro tissue engineering to generate a human-sized auricle and nasal tip," *Laryngoscope,* vol. 113, p. 90, 2003.

[4]   W. S. Kim, J. P. Vacanti, L. Cima, D. Mooney, J. Upton, W. C. Puelacher, and C. A. Vacanti, "Cartilage engineered in predetermined shapes employing cell transplantation on synthetic biodegradable polymers," *Plastic and Reconstructive Surgery,* vol. 94, p. 233, 1994.

[5]   K. Kojima, L. J. Bonassar, R. A. Ignotz, K. Syed, J. Cortiella, and C. A. Vacanti, "Comparison of tracheal and nasal chondrocytes for tissue engineering of the trachea," *The Annals of Thoracic Surgery,* vol. 76, p. 1884, 2003.

[6]   H. Mizuno, A. K. Roy, C. A. Vacanti, K. Kojima, M. Ueda, and L. J. Bonassar, "Tissue-engineered composites of anulus fibrosus and nucleus pulposus for intervertebral disc replacement," *Spine,* vol. 29, p. 1290, 2004.

[7]   W. C. Puelacher, D. Mooney, R. Langer, J. Upton, J. P. Vacanti, and C. A. Vacanti, "Design of nasoseptal cartilage replacements synthesized from biodegradable polymers and chondrocytes," *Biomaterials,* vol. 15, p. 774, 1994.

[8]   W. C. Puelacher, J. Wisser, C. A. Vacanti, N. F. Ferraro, D. Jaramillo, and J. P. Vacanti, "Temporomandibular joint disc replacement made by tissue-engineered growth of cartilage," *Journal of Oral and Maxillofacial Surgery,* vol. 52, pp. 1172-1177, 1994.

[9]   W. C. Puelacher, J. P. Vacanti, N. F. Ferraro, B. Schloo, and C. A. Vacanti, "Femoral shaft reconstruction using tissue-engineered growth of bone," *International Journal of Oral & Maxillofacial Surgery,* vol. 25, pp. 223-228, 1996.

[10]   Y. Weng, Y. Cao, C. Arevalo, M. P. Vacanti, and C. A. Vacanti, "Tissue-engineered composites of bone and cartilage for mandible condylar

reconstruction," *Journal of Oral and Maxillofacial Surgery,* vol. 59, pp. 185-190, 2001.

[11] T. J. Klein, B. L. Schumacher, T. A. Schmidt, K. W. Li, M. S. Voegtline, K. Masuda, E. Thonar, and R. L. Sah, "Tissue engineering of stratified articular cartilage from chondrocyte subpopulations," *Osteoarthritis and Cartilage,* vol. 11, pp. 595-602, 2003.

[12] T. K. Kim, B. Sharma, C. G. Williams, M. A. Ruffner, A. Malik, E. G. McFarland, and J. H. Elisseeff, "Experimental model for cartilage tissue engineering to regenerate the zonal organization of articular cartilage," *Osteoarthritis and Cartilage,* vol. 11, pp. 653-664, 2003.

[13] K. W. Ng, C. C. B. Wang, R. L. Mauck, T. A. N. Kelly, N. O. Chahine, K. D. Costa, G. A. Ateshian, and C. T. Hung, "A layered agarose approach to fabricate depth-dependent inhomogeneity in chondrocyte-seeded constructs," *Journal of Orthopaedic Research,* vol. 23, pp. 134-141, 2005.

[14] C. T. Hung, E. G. Lima, R. L. Mauck, E. Taki, M. A. LeRoux, H. H. Lu, R. G. Stark, X. E. Guo, and G. A. Ateshian, "Anatomically shaped osteochondral constructs for articular cartilage repair," *Journal of Biomechanics,* vol. 36, pp. 1853-1864, 2003.

[15] Y. Cao, A. Rodriguez, M. Vacanti, C. Ibarra, C. Arevalo, and C. A. Vacanti, "Comparative study of the use of poly (glycolic acid), calcium alginate and pluronics in the engineering of autologous porcine cartilage," *Journal of Biomaterials Science, Polymer Edition,* vol. 9, pp. 475-487, 1998.

[16] S. C. Chang, J. A. Rowley, G. Tobias, N. G. Genes, A. K. Roy, D. J. Mooney, C. A. Vacanti, and L. J. Bonassar, "Injection molding of chondrocyte/alginate constructs in the shape of facial implants," *Journal of Biomedical Materials Research,* vol. 55, pp. 503-511, 2001.

[17] D. R. Albrecht, V. L. Tsang, R. L. Sah, and S. N. Bhatia, "Photo- and electropatterning of hydrogel-encapsulated living cell arrays," *Lab On a Chip,* vol. 5, pp. 111-118, 2004.

[18] Y. Lu, G. Mapili, G. Suhali, S. Chen, and K. Roy, "A digital micro-mirror device-based system for the microfabrication of complex, spatially patterned tissue engineering scaffolds.," *Journal of Biomedical Materials Research Part A,* vol. 77, pp. 396-405, 2006.

[19] V. L. Tsang and S. N. Bhatia, "Three-dimensional tissue fabrication," *Advanced Drug Delivery Reviews,* vol. 56, pp. 1635-1647, 2004.

[20] R. Landers, U. Hübner, R. Schmelzeisen, and R. Mülhaupt, "Rapid prototyping of scaffolds derived from thermoreversible hydrogels and tailored for

applications in tissue engineering," *Biomaterials,* vol. 23, pp. 4437-4447, 2002.

[21] R. Landers, A. Pfister, U. Hübner, H. John, R. Schmelzeisen, and R. Mülhaupt, "Fabrication of soft tissue engineering scaffolds by means of rapid prototyping techniques," *Journal of Materials Science,* vol. 37, pp. 3107-3116, 2002.

[22] X. Wang, Y. Yan, Y. Pan, Z. Xiong, H. Liu, J. Cheng, L. Feng, L. Feng, R. Wu, R. Zhang, and Q. Lu, "Generation of three-dimensional hepatocyte/gelatin structures with rapid prototyping system," *Tissue Engineering,* vol. 12, pp. 83-90, 2006.

[23] X. Wei, W. Xiaohong, Y. Yongnian, Z. Wei, X. Zhuo, L. Feng, W. Rendong, and Z. Renji, "Rapid prototyping three-dimensional cell/gelatin/fibrinogen constructs for medical regeneration," *Journal of Bioactive and Compatible Polymers,* vol. 22, pp. 363-377, July 1, 2007 2007.

[24] Y. Yan, X. Wang, Y. Pan, H. Liu, J. Cheng, Z. Xiong, F. Lin, R. Wu, R. Zhang, and Q. Lu, "Fabrication of viable tissue-engineered constructs with 3D cell-assembly technique," *Biomaterials,* vol. 26, pp. 5864-5871, 2005.

[25] Y. Yan, X. Wang, Z. Xiong, H. Liu, F. Liu, F. Lin, R. Wu, R. Zhang, and Q. Lu, "Direct construction of a three-dimensional structure with cells and hydrogel," *Journal of Bioactive and Compatible Polymers,* vol. 20, pp. 259-269, 2005.

[26] C. M. Smith, A. L. Stone, R. L. Parkhill, R. L. Stewart, M. W. Simpkins, A. M. Kachurin, W. L. Warren, and S. K. Williams, "Three-dimensional BioAssembly tool for generating viable tissue-engineered constructs," *Tissue Engineering,* vol. 10, pp. 1566-1576, 2004.

[27] V. Mironov, T. Boland, T. Trusk, G. Forgacs, and R. R. Markwald, "Organ printing: computer-aided jet-based 3D tissue engineering," *Trends in Biotechnology,* vol. 21, pp. 157-161, 2003.

[28] S. Khalil and W. Sun, "Bioprinting endothelial cells with alginate for 3D tissue constructs," *Journal of Biomechanical Engineering,* vol. 131, pp. 1002-1008, 2009.

[29] F. Pérès and D. Noyes, "Envisioning e-logistics developments: Making spare parts in situ and on demand state-of-the-art and guidelines for future developments," *Computers in Industry,* vol. 57, pp. 490-503, 2006.

[30] L. Sun, K. J. Jakubenas, J. E. Crocker, S. Harrison, L. L. Shaw, and H. L. Marcus, "In situ thermocouples in macro-components fabricated using SALD and SALDVI techniques," *Materials and Manufacturing Processes,* vol. 13, pp. 909-919, 1998.

[31]   E. Whitney, "Advances in rapid prototyping and manufacturing using laser-based solid free-form fabrication," in *The Handbook of Advanced Materials*, Oak Ridge, TN: John Wiley & Sons, 2004, pp. 611-631.

[32]   D. L. Cohen, E. Malone, H. Lipson, and L. J. Bonassar, "Direct freeform fabrication of seeded hydrogels in arbitrary geometries," *Tissue Engineering,* vol. 12, pp. 1325-1335, 2006.

[33]   C. Doumanidis and Y.-M. Kwak, "Geometry modeling and control by infrared and laser sensing in thermal manufacturing with material deposition," *Journal of Manufacturing Science and Engineering,* vol. 123, pp. 45-52, 2001.

[34]   C. Doumanidis and E. Skordeli, "Distributed-parameter modeling for geometry control of manufacturing processes with material deposition," *Journal of Dynamic Systems, Measurement, and Control,* vol. 122, pp. 71-77, 2000.

[35]   J. Mazumder, A. Schifferer, and J. Choi, "Direct materials deposition: designed macro and microstructure," *Materials Research Innovations,* vol. 3, pp. 118-131, 1999.

[36]   M. J. Lovelady and J. D. Watts, "Closed loop feedback for continuous mode materials jetting," in *IEEE/CPMT International Electronic Manufacturing Technology Symposium*, Austin, Texas, 1999, pp. 189-195.

[37]   E. Malone and H. Lipson, "Fab@Home: the personal desktop fabricator kit," *Rapid Prototyping Journal,* vol. 13, pp. 245-255, 2007.

[38]   W. D. Bugbee and F. R. Convery, "Osteochondral allograft transplantation," *Complex Topics in Knee Surgery,* vol. 18, pp. 67-75, 1999.

[39]   S. J. Hospodar and J. M. Tokish, "Management of articular cartilage injuries in the knee," *Operative Techniques in Sports Medicine,* vol. 13, pp. 150-156, 2005.

[40]   G. Bentley, L. C. Biant, W. J. Carrington, M. Akmal, A. Goldberg, A. M. Williams, J. A. Skinner, and J. Pringle, "A prospective, randomised comparison of autologous chondrocyte implantation versus mosaicplasty for osteochondral defects in the knee," *Journal of Bone and Joint Surgery,* vol. 85, pp. 223-230, 2003.

[41]   R. E. Meehan and M. E. Brage, "Fresh osteochondral allografting for osteochondral defects of the talus: a case review," *Techniques in Foot & Ankle Surgery,* vol. 3, pp. 53-61, 2004.

[42]   M. E. Easley and P. E. Scranton, "Osteochondral autologous transfer system," *Foot and Ankle Clinics,* vol. 8, pp. 275-290, 2003.

[43]   M. Dienst, P. E. Greis, B. J. Ellis, K. N. Bachus, and R. T. Burks, "Effect of lateral meniscal allograft sizing on contact mechanics of the laterial tibial plateau: An experimental study in human cadaveric knee joints," *American Journal of Sports Medicine,* vol. 35, pp. 34-42, 2007.

[44]   T. L. Haut, M. L. Hull, and T. S. Howell, "Use of roentgenography and magnetic resonance imaging to predict meniscal geometry determined with a three-dimensional coordinate digitizing system," *Journal of Orthopaedic Research,* vol. 18, pp. 228-237, 2000.

[45]   S. Sampath, "Novel concepts in direct writing of electronics and sensors," *IEEE Sensors Journal,* vol. 4, 2004.

[46]   D. L. Cohen and H. Lipson, "Geometric feedback control of discrete-deposition SFF systems," *Rapid Prototyping Journal,* accepted.

CHAPTER 5: ADDITIVE MANUFACTURING FOR *IN SITU* REPAIR AND ADAPTATION OF ROBOTS[*]

ABSTRACT

Computational techniques, such as evolutionary computation, have enabled computer systems to autonomously design, repair and adapt robotic systems. These approaches, however, are limited to the virtual world. The output of these processes is a design or a robot controller, but not a physical manifestation of the result. Additive manufacturing (AM), however, has been used to extend autonomous design of robots into the physical world. After an evolutionary computation design process, AM machines were used to directly fabricate the resultant robots demonstrating an autonomous design-to-build cycle. These techniques however, fall short of repair and adaptation of existing robots due to a lack of geometric feedback-based AM techniques. In order for the AM system to effectively print on the target robot, it must understand both the current and intended geometries. With lower cost imaging modalities and new feedback-based planning AM algorithms, existing robots can be printed on and physical repair/adaptation can be enabled. In this paper, we propose a new planning algorithm based on geometric differencing, called Difference-Based Planning (DBP), and also demonstrate two proof-of-concept prints that highlight the potential of *in situ* AM repair and adaptation. The first print repairs a critically damaged leg of a four-legged robot with a mean absolute error of only 1.3 mm; the second adapts the design to enable the legs to traverse a mesh walking surface. In addition to demonstrating the capabilities of *in situ* AM, technical issues are explored and potential applications discussed.

[*] Daniel L. Cohen[1], Jeffrey I. Lipton[1], Hod Lipson[1,2]; [1]Cornell University, Mechanical and Aerospace Engineering, Ithaca NY; [2]Cornell University, Computing and Information Science, Ithaca NY.

INTRODUCTION

Autonomy of robotic systems has tremendous potential to transform the role that the machines play in society. Algorithms for autonomous operation of robots have been extensively explored throughout the last few decades[1-6]. More recently, advances in evolutionary computation have enabled computers to autonomously design robots[7-8]. These algorithms start with performance objectives and randomly generate designs while rewarding better-performing configurations. Furthermore, evolutionary computation has been employed for autonomous repair of robotic systems[9]. For example, with walking robots that have sustained severe damage to a limb, these algorithms can diagnose the error and create alternative walking patterns that overcome the damage. In addition to repair, similar approaches can be used to modify existing systems to create new functionality. These techniques are mostly computational and limited to the virtual realm, where the output is an abstract design or robot controller.

Additive manufacturing, however, has been used to extend autonomous robot design beyond just the virtual world. AM has been used to directly translate autonomously generated robot designs into the physical domain[8]. Upon completion of the evolutionary computation-based design cycle, AM machines were used to directly print out the resultant robot design[8]. While AM has been able to bridge the virtual and physical worlds for autonomous design and fabrication of robotic systems, there remains a barrier to repair of robots due to a lack of geometric feedback-based AM techniques. In order to effectively execute *in situ* AM on pre-existing objects, i.e. repair of broken robots, the AM system must employ geometric feedback. The system must understand both the intended and actual robot geometries, and subsequently, assess the damage and plan the repair. While geometric feedback has been harnessed in AM for the purposes of quality assurance, it has not been demonstrated for *in situ*

printing[10-14]. For example, build-material bead height was monitored in order to determine laser power[14] during direct metal deposition AM. Other direct metal deposition-based AM techniques used distributed parameter modeling to estimate printing parameters in real-time and adjust feed-rates accordingly[11-12]. Similar techniques were also used for drop-on-demand AM systems in which geometric data was collected and the system adjusted jetting pressures[13]. These techniques, however, were aimed at stabilizing material-related process uncertainty, not at addressing situational uncertainty related to an unknown substrate geometry. They were collecting geometric data of droplet shapes, not collecting higher-level geometric data of the overall build-envelope geometry. One technique, Greedy Geometric Feedback (GGF), is a closed-loop geometric feedback approach that is capable of handling situational uncertainty since it monitors whole-part shape[10] (Chapter 3). GGF, however, is overkill in the sense that it ascertains geometric data iteratively which is unnecessary for static substrates of which the geometry must only be determined once at the start of the print. Due to the lack of appropriate AM-path planning approaches, all examples of *in situ* printing to date, have not used any kind of geometric feedback and entirely relied upon hard-coded *a priori* knowledge of the substrate geometry[15-18]. One prior *in situ* example involved direct-writing of conductive ink onto dome-shaped helmets to fabricate functional antennae[18]. Another example demonstrated *in situ* fabrication of a thermocouple onto a complex assembly. In both of these cases prints were performed onto pre-existing objects, however, neither were examples of *generalized in situ* AM since the substrate geometries were hard-coded in the system *a priori*.

We propose herein a low-overhead AM-path planning approach, called Difference-Based Planning (DBP), which employs image differencing between the original and post-damage geometries (in a repair context) or between the current and

151

adapted-design geometries (in an adaptation context). The proposed difference-based scheme is lower cost in terms of data collection than GGF and, considering data collection expense, better suited for handling situational uncertainty associated with *in situ* printing. We also propose related image processing techniques including Boolean pixel-wise differencing and region growing to create and subsequently noise-wash the target-print geometry. By utilizing various imaging modalities, including CT and laser scanning, and harnessing geometric feedback, direct *in situ* AM for physical repair of robotic systems is feasible. Moreover, similar approaches can be used to make physical adaptations to robots in order to augment functionality. In the work presented herein, we demonstrate two proof-of-concept prints: 1) repair of a broken robot that has sustained critical damage to a limb, and 2) morphological adaptation of a robot to impart new functionality.

These proof-of-concept prints explore technical issues related to implementation of *in situ* printing approaches, as well as potential applications of the technology. Through *in situ* AM, the autonomy loop can be closed from design, through operation, to repair and adaptation of robotic systems. Powerful algorithms for autonomy can potentially be directly extended into the physical world and new paradigms within robotics could be enabled.

METHODS AND MATERIALS

Overall Approach

A novel AM-path planning, Difference-Based Planning (DBP) is proposed herein and serves as the underpinning of *in situ* AM.   Unlike the Greedy Geometric Feedback (GGF) approach, in which geometric data is iteratively collected, DBP only collects substrate-geometry data once before the print. In the cases of statically

shaped substrates, iterative data collection to address situational uncertainty is wasteful. While iterative geometric data collection could still be important for handling other types of process uncertainties, including materials uncertainty, for the purposes of printing in contexts that solely possess situational uncertainty related to substrate-shape, iterations are unnecessary and inefficient.

In the most generalized autonomous case, the substrate shape (i.e. the robot) is not known *a priori* and thus geometric feedback is necessary in order for the AM system to know what it is printing on. If in addition to the image of the actual substrate shape, there exists an image of the intended shape, the AM system can be used to physically modify the pre-existing substrate to a desired shape.

If a before-damage image of the robot is archived and injury is subsequently sustained, with one additional imaging step (i.e. a pre-print capture of the actual robot shape), robot repair can be achieved. The before- and after-damage images can be differenced and the missing piece or pieces can be replaced by the printer *in situ*. Besides *in situ* repair, a similar approach can also be used for *in situ* adaptation. If the actual robot shape is differenced against a desired augmented shape (such as a new design that extends additional functionality), the printer can print the adapted part *in situ* directly onto the robot.

Additive Manufacturing System

See "Additive Manufacturing System" in Chapter 4.

Imaging

Whether comparing before- and after-damage images (i.e. *in situ* repair), or original and adapted images (i.e. *in situ* adaptation), geometric data collection is at the core of these techniques. Depending on the nature of the repair or adaptation, various

imaging modalities can be used. If the geometry is rather simple, it is possible for 2.5D imaging techniques such as top-down laser scanning to suffice. If the geometry is more complex, however, full 3D modalities will be necessary. For describing the intended target geometry of desired adaptations, an innately-3D CAD system can be used.

For the repair print conducted herein, Case 1, the before- and after-damage images were both captured using a clinical grade CT scanner. CT images were collected on a 16-slice Toshiba Aquilion LB. Volumetric data was collected in 0.5 mm segments, and reconstructed using standard Toshiba-unit bone[19] algorithms. The Toshiba soft tissue algorithm was also tested for CT scaning the robot, however, relative to the bone algorithm it demonstrated poorer detail of metal parts and exhibited unacceptable adverse noise near the servos' metallic gearboxes. For the adaptation print, Case 2, the actual geometry image was captured on CT, as described above, and compared to a theoretical target geometry represented is SolidWorks CAD.

DPB – Image Differencing and Path Planning

Once the CT images were captured and the CAD model was created, both types of images were converted into STL files. While the CAD software could directly output STL files, the CT images had to be explicitly converted through a third-party software package. The CT files were imported in Mimics V12 (Materialise Group, Leuven, Belgium) as DICOM files and converted into 3D solid models. During this conversion, the robot structure was isolated by creating a mask that thresholded intensity values between 100 and 3000 Hounsfields, which corresponded to the epoxy of the robot. These values were determined by iteratively varying the threshold values within the preview mode of Mimics V12 and extracting values that removed background noise while not adversely eliminating points within the robot's

boundaries. To remove image noise and isolate the robot, a region growing algorithm was employed in Mimics V12 where the robot's centroid served as the seed location. Neighboring voxels within the threshold intensity range were included in the data set. The resultant mask was then converted to a 3D mesh, which was exported as an STL file.

STL files were differenced in Mimics V12, outputting the printable shape to achieve repair or adaptation, by applying a Boolean subtraction operator (the core operation of DBP) to the STL files. The "differenced" STL file was imported into the Fab@Home's open-source control software in order to create the path plan of the target print geometry, which employed a standard raster-planning algorithm.

Robot-in-Printer Registration

Once the differencing and planning algorithm created the geometry of the construct to be printed, the system had to understand the robot's exact position within the printer in order to complete the sequence autonomously. A laser unit with 0.12 mm height resolution was mounted behind the deposition tool of the AM system and used to collect height information at 0.3 mm X-Y increments (see "Chapter 4").

The controlling computer then compared the resultant heightmap to a 2D binary image which was extracted from the CT scan and CAD data. To convert the CT scan and CAD STLs into binary images (to match the format of the laser data), the 3D points clouds were projected top-down onto the X-Y plane through Mimics V12 and then grouped into 0.5 mm by 0.5 mm bins. Each pixel was then thresholded such that if the pixel contained the robot, it was set to 1, and if not, it was set to 0. In order to perform the registration operation, matrices of each heightmap were translated and rotated in the X-Y plane by test values, whose magnitudes were iteratively varied. The X-Y test offsets were iteratively varied in 0.5 mm increments over the entire

range of the heightmaps' X-Y indexes. The angular offset was varied by 1 degree increments initially, and after a close solution was found, the algorithm did a secondary iterative search with 0.1 degree increments ±10 degrees of the initially determined angular offset. The sum of the absolute value of the element-by-element difference was recorded for all of the test X-Y offsets. This brute force search returned an X-Y offset with a corresponding minimal error, which was the optimal registration. Once these 2D binary images were aligned, the system applied the extracted X-Y and angular offsets to the target print, shifted/rotated the target geometry, and the resultant print was then in the proper coordinate system of the actual robot within the printer.

Geometric Fidelity Characterization

See "Geometric Fidelity Characterization" in Chapter 4.

Substrate-Robot

The printing and adaptation experiments were performed on a 190 mm × 190 mm × 25 mm walking robot. This robot was human-designed in CAD. The robot body and the four robot legs were printed of a two-part epoxy (FabEpoxy™; Kraftmark Inc.; Spring City, Pennsylvania) on the Fab@Home AM system (Figure 5.1).

The robot had 4 legs, each with a 180 degree range of motion. The servos (Futaba Inc.; Champaign, Illinois) also acted as the body-to-leg hinges. Each servo was custom modified; free-spinning bearing-mounted idler arms were mounted to the non-output-shaft sides of the servo (Figure 5.2). Each arm was secured to the body through an interference fit with an adapter plate (printed on a commercial Objet™ printer), which was screwed directly into the epoxy robot frame.
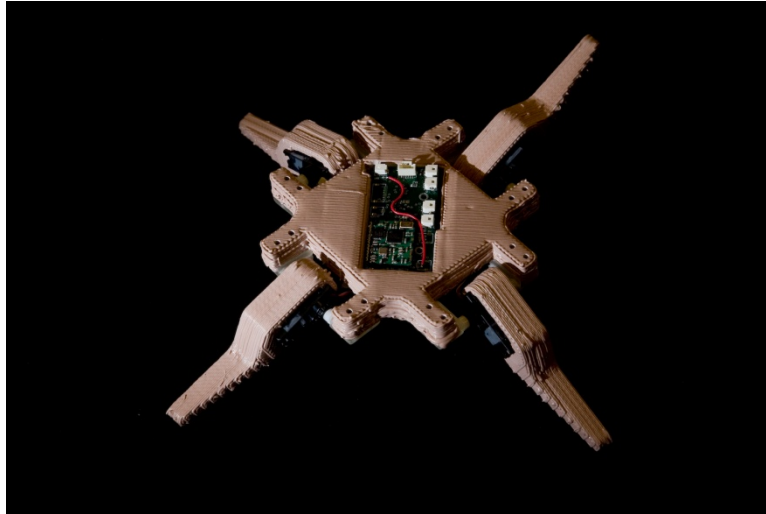
a)
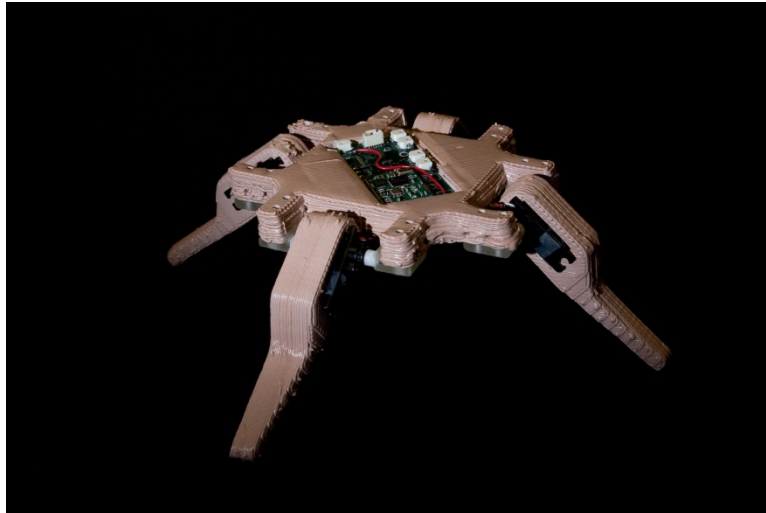
b)

Figure 5.1. Robotic printing substrate prior to damage or adaptation. The robot comprises four legs actuated by servos. (a) Top view. (b) Side view.
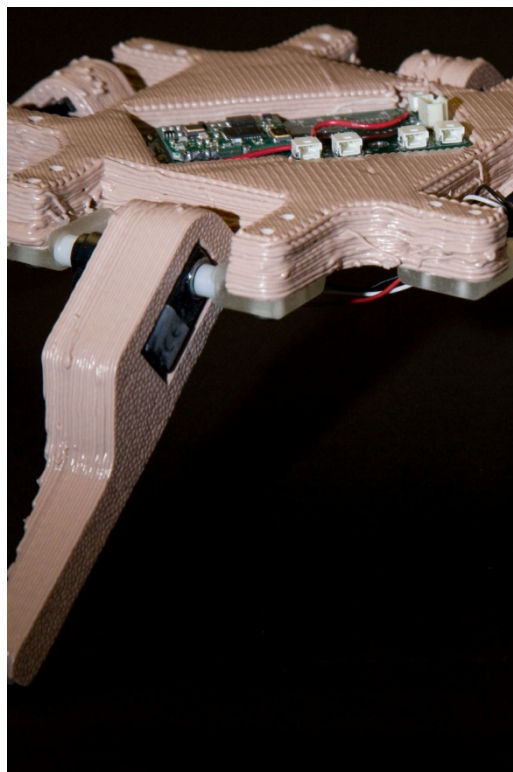
Figure 5.2. Close-up view of the robot leg. The leg attaches to the servo with an interference fit. The servo attaches to the robot body by attaching to the mounting plate through an interference fit, and the plate is screwed to the body.

The two output arms of each motor (one driven and one idling) were attached to the leg recess of the robot body. The legs were attached to the servos through interference fits.

Case 1 – *In Situ* Repair

The repair proof-of-concept experiment demonstrated the *in situ* repair of a severely damaged robot. The intact, undamaged robot was CT scanned and this before-damage image was archived. The leg was subsequently sliced-off at a 45 degree angle transverse to the leg axis directly below the servo housing. The robot was CT scanned again. The before- and after-damage images were compared, differenced and used for path planning (as described above). The laser heightmap was

captured and used for registration of the robot within the printer. The differenced part was printed back using the same epoxy that the robot was originally printed with (FabEpoxy™; Kraftmark Inc.; Spring City, Pennsylvania). The geometric fidelity of the printed part was assessed using above-described protocol.

Case 2 – *In Situ* Adaptation

The adaptation experiment demonstrated the physical modification of the structure of a robot in order to impart new functionality. The slender tip of the robot legs were approximately 9 mm wide. For certain terrains, for example 12 mm by 12 mm standard gauge wire mesh, this narrow robot leg would slip through crevices and prohibit effective traversing. A CAD model of an extension for the leg was created in SolidWorks 2007; the design was intended to increase the thickness of the leg and prevent the robot from slipping through the previously un-traversable wire mesh. The adaptation was path-planned, differenced, registered, and printed from silicone.

RESULTS

Case 1 – *In Situ* Repair

The before- and after-damage CT images were captured and converted to STL files (Figure 5.3). The damaged robot was placed in the AM machine and the laser scan was conducted.
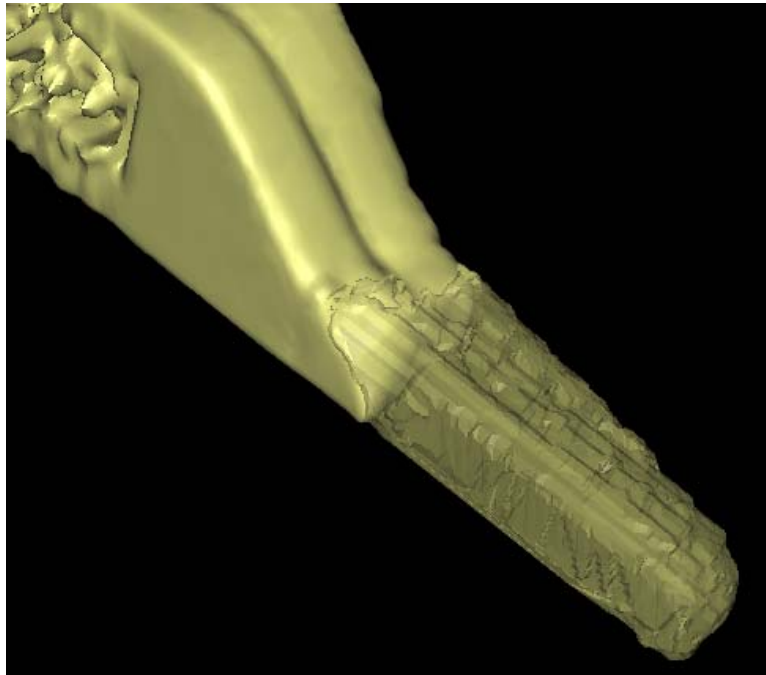
a)
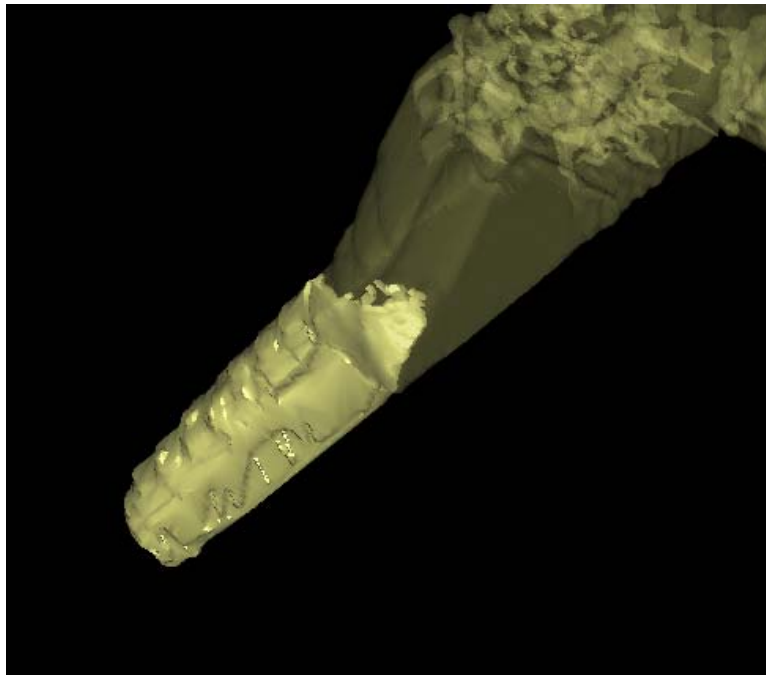
b)

Figure 5.3. Close-up views of damage to robot leg. (a) Top-down isometric view of robot leg. Original geometry, translucent, overlayed with post-damage geometry, opaque. (b) Bottom-up view of robot leg. Original and post-damage geometries overlayed.

The laser data was registered with the 2D binary image extracted from the CT scan in order to find the offsets between the CT and AM machine coordinate systems (Figure 5.4). The before- and after-damage CT images were differenced and the resultant geometry was path planned and rotated/translated according to the registration offsets.
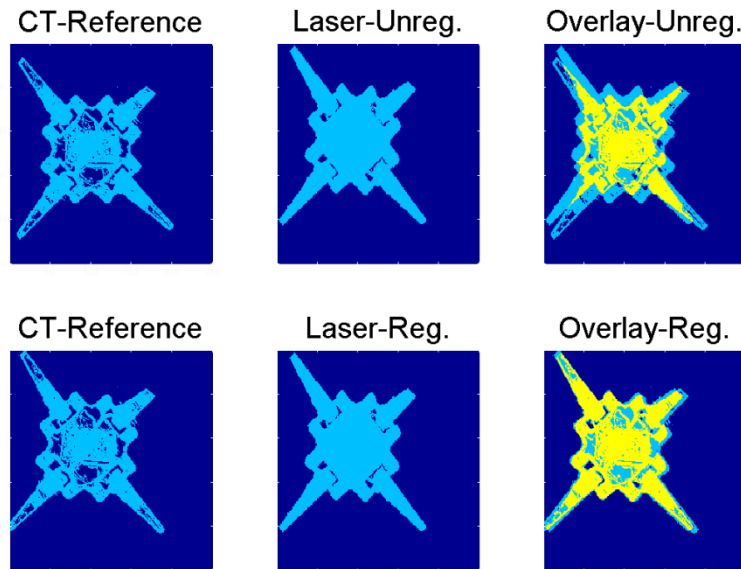
Figure 5.4. Registration of the laser data and CT scan to find relative transform between the two coordinate systems.

The print of the differenced geometry was executed directly onto the surface of the robot. During the print, visual inspection found that the deposition tip closely followed the shape of the robot's damage interface.

Upon completion of the print, 24 hours was allowed for curing of the epoxy, and then the robot was removed from the AM machine's base plate. The printed leg portion fused to the remainder of the leg and was structurally intact; the repaired portion was self-supporting (Figure 5.5).

161
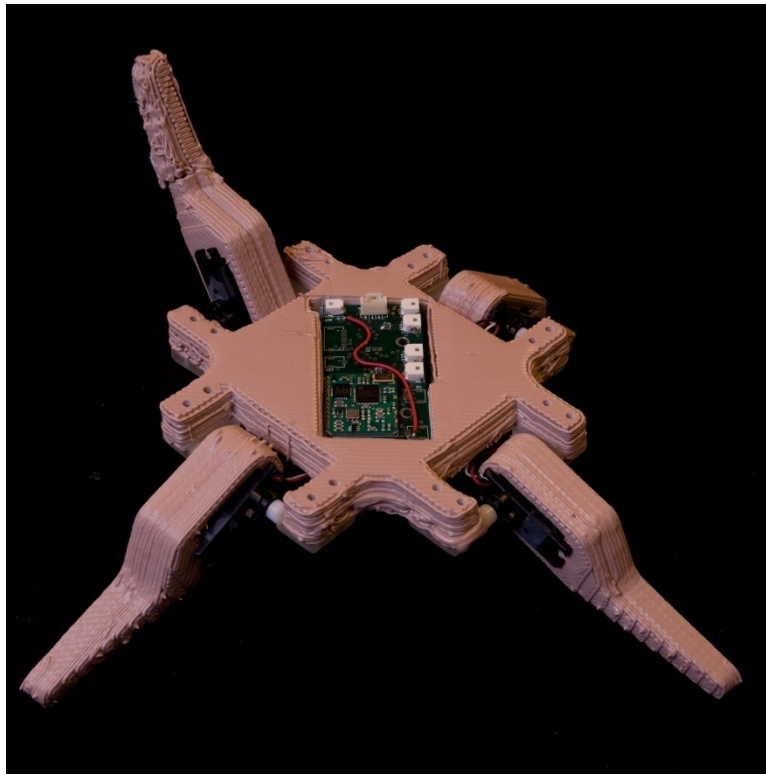
a)

b)

Figure 5.5. Robot after repair of its severed leg. (a) Top view. (b) Side view.

The mean absolute error for the repaired portion of the damaged leg was 1.3 mm with a standard deviation of 1.6 mm (Figure 5.6). Fifty four percent of the points exhibited less than 1.25 mm of error.
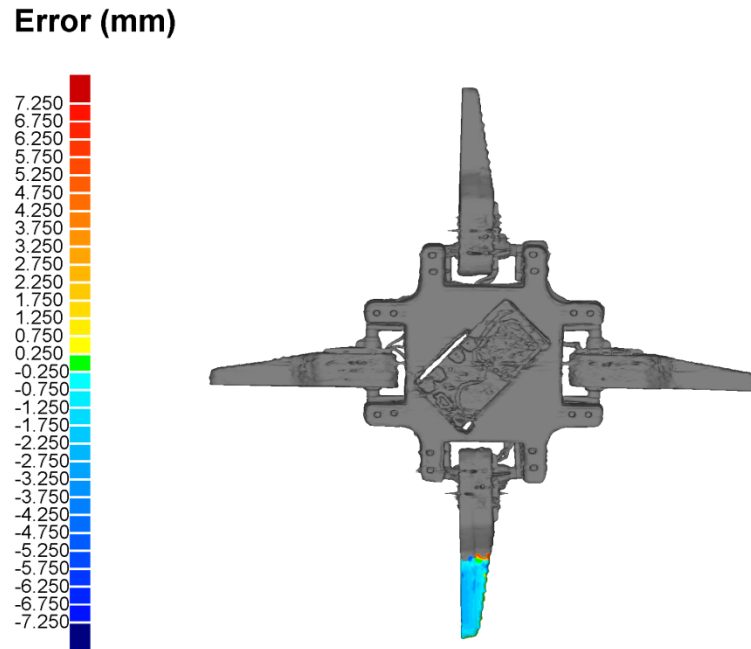
Error (mm)

Figure 5.6. Top-view error plot of the *in situ* repaired leg. The original CT scan of the undamaged robot was used as the reference geometry and computationally compared with the CT scan of the repaired leg. Error magnitude is signified by color as indicated on the associated scale.

Case 2 – *In Situ* Adaptation

The unmodified original robot's slender legs limit functionality to certain terrains. Surfaces with crevices, such as the mesh surface described above, were prohibitive for the robot since the legs would slip through (Figure 5.7).

Figure 5.7. Prior to adaptation, the slender end of the robot leg slips through the mesh surface making traversal impossible.
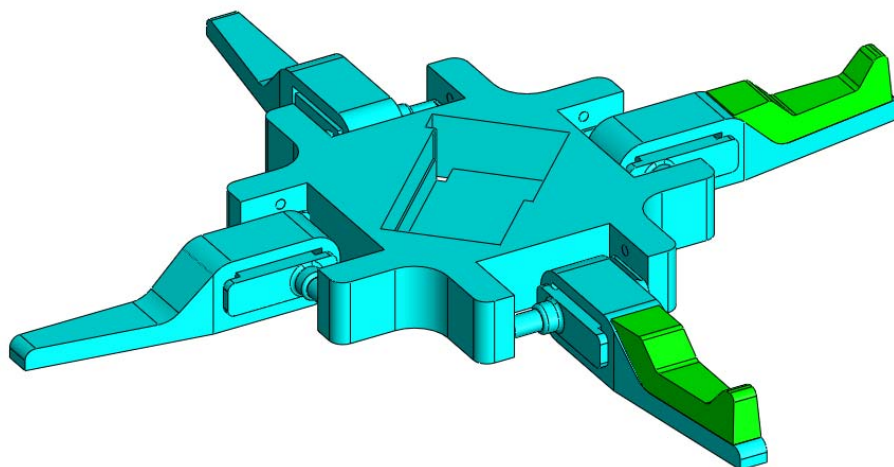
Figure 5.8. CAD model of intended leg adaptation. The adaptation was designed to change the leg-tip thickness and allow the robot to traverse a mesh surface. Original robot geometry, green, and adaptation overlayed, green.

a)
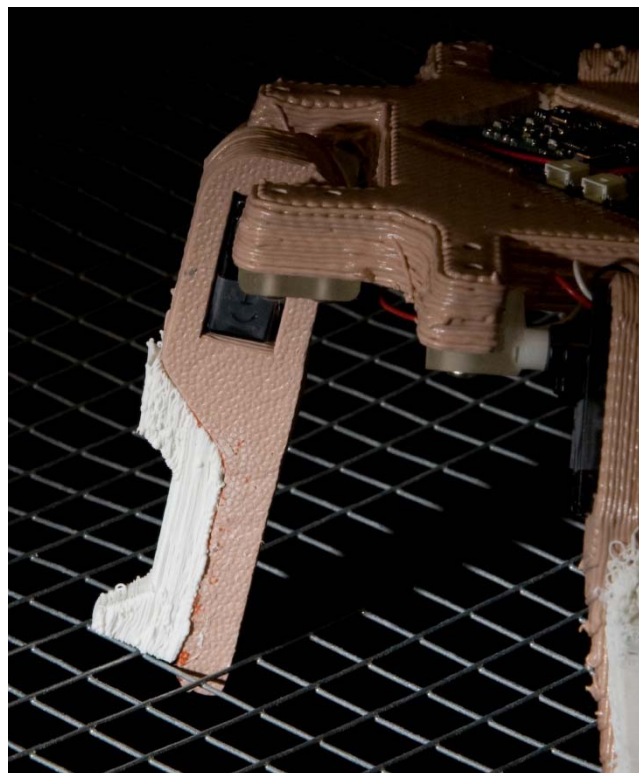
b)

Figure 5.9. Robot after adaptation of two legs. (a) Close-up view of leg with adaptation printed on top of pre-existing leg. The printed part thickened the leg and prevented slipping of the leg through the mesh. (b) Side view.

A CAD modification was designed that thickened the tip of the leg (Figure 5.8). This CAD model was converted to an STL file, differenced with the CT scan of the original model, and the differenced geometry was path planned. After registration, as described above, the print was executed using silicone as the build material.

The silicone adaptations bonded to the robot leg substrate. Two legs were adapted in the manner described herein. After adaptation, the robot legs no longer slipped through the mesh. The robot, post-adaptation, was able to stand on the mesh surface without getting stuck in the crevices of the walking surface (Figure 5.9).

DISCUSSION

The DBM approach successfully enabled the restoration of the damaged robot to its prior physical state within 1.3 mm or mean absolute error, as well as enabled morphological adaptation. The technique is generalized in that it does not require human-hard-coded heuristics or guidance, unlike prior demonstrations of *in situ* printing[16,18]. Instead, the differencing of the pre- and post-damage images provided sufficient geometric data for repair printing. When the current physical state was compared instead to an alternative new design, the same approach enabled autonomous physical adaptation of the robot.

The Boolean subtraction operation was the core of the DBP technique, however, equally important was the intensity thresholding selection and region growing operations. Together, these operations cleaned the result of the difference operation to a usable form and isolated the construct-of-interest. Another important *in situ*-specific AM operation was the robot-in-printer registration. This simple yet effective technique enabled autonomous *in situ* printing during repair and adaptation. While trivial constraints could have been imposed, such as a jig of known position and

shape or manually selected feature-based registration, the laser-based approach maintained the technique's autonomy and extends the approach's utility.

The technique is generalized and flexible enough to accommodate repair or adaptation, however, certain practical limitations of AM must be considered. Even though the CT imaging modality delivers 3D geometric information, it is not necessarily the case that the AM system can make all 3D repairs. In particular, when printing on a pre-existing object such as a damaged robot, the deposition head of the robot must have direct access to the printing surface and if the substrate interferes, certain prints will be prohibited. For example, if an overhang of the robot blocked access of the deposition tip to the surface, there would be unprintable regions during the repair operation. Due to the particular shapes involved in these two proof-of-concept experiments, interference was not a concern. A second consideration is the bonding of the material to previously deposited layers. The epoxy used herein bonded sufficiently to the fully cured epoxy of the robot body, however, other material combinations could lead to problems and must be carefully selected.

Physically repairing and adapting robots extends powerful computational techniques[1-6] to the physical realm. While AM has previously been used to directly connect virtual computational design techniques with physical implementation[7-8], a lack of geometric feedback prevented repair and adaptation of existing robots. These barriers have been overcome, as demonstrated herein, due to the lower cost of powerful imaging modalities and the development of *in situ* AM algorithms such as difference-based planning.

Some practical applications of these types of *in situ* AM operations include in-place repair of difficult to transport/disassemble machines[15]. Also, rather than replacing a damaged part, *in situ* AM has the potential to salvage it. One particularly affected field is space exploration[20]. In addition to repair of remotely located

machines and structures, physical adaptation allows for service lives of equipment to be extended and changed for new, previously unforeseen missions. Considering the non-trivial transport time between launch and the destination, it is likely that technologies could have progressed during transport or new missions emerge. With physical adaptation however, the launched systems could be remotely and autonomously updated with the latest technologies to fulfill newly appointed missions[20].

On a separate level, these techniques can be seen as the completion of the robot life cycle[21]. Robots previously had the ability to autonomously design and physically fabrication themselves through AM[21]. Now, they conceivably have the ability to repair and adapt: closing the loop. These developments are enables of autonomous robotic ecologies, or other types of complex autonomous robotic systems.

Whether for creating fully functional autonomous robotic ecologies[21], or more practical reasons such as repair and adaptation of complex machines[15,20], geometric feedback greatly empowers AM. Through additional developments in printing materials and more advanced planning algorithms, *in situ* AM has the potential to extend machines powerful new capabilities.

REFERENCES

[1]   M. Asada, K. F. MacDorman, H. Ishiguro, and Y. Kuniyoshi, "Cognitive developmental robotics as a new paradigm for the design of humanoid robots," *Robotics and Autonomous Systems,* vol. 37, pp. 185-193, 2001.

[2]   D. Cliff, P. Husbands, and I. Harvey, "Explorations in evolutionary robotics," *Adaptive Behavior,* vol. 2, pp. 73-110, June 1, 1993 1993.

[3]   I. J. Cox and G. T. Wilfong, *Autonomous robot vehicles*. New York: Springer-Verlag, 1990.

[4]   F. Hoffmann and G. Pfister, "Evolutionary design of a fuzzy knowledge base for a mobile robot," *International Journal of Approximate Reasoning,* vol. 17, pp. 447-469, 1997.

[5]   A. Saffioti, "The uses of fuzzy logic in autonomous robot navigation," *Soft Computing,* vol. 1, pp. 180-197, 1997.

[6]   G. Schoner, M. Dose, and C. Engels, "Dynamics of behavior: theory and applications for autonomous robotic architectures," *Robotics and Autonomous Systems,* vol. 16, pp. 213-244, 1995.

[7]   P. Funes and J. Pollack, "Evolutionary body building: Adaptive physical designs for robots," *Artificial Life,* vol. 4, pp. 337-357, 1998.

[8]   H. Lipson and J. Pollack, "Automatic design and manufacture of robotic lifeforms," *Nature,* vol. 406, pp. 974-978, 2000.

[9]   J. Bongard, V. Zykov, and H. Lipson, "Resilient machines through continuous self-modeling," *Science,* vol. 314, pp. 1118-1121, November 17, 2006 2006.

[10]   D. L. Cohen and H. Lipson, "Geometric feedback control of discrete-deposition SFF systems," *Rapid Prototyping Journal,* accepted.

[11]   C. Doumanidis and Y.-M. Kwak, "Geometry modeling and control by infrared and laser sensing in thermal manufacturing with material deposition," *Journal of Manufacturing Science and Engineering,* vol. 123, pp. 45-52, 2001.

[12]   C. Doumanidis and E. Skordeli, "Distributed-parameter modeling for geometry control of manufacturing processes with material deposition," *Journal of Dynamic Systems, Measurement, and Control,* vol. 122, pp. 71-77, 2000.

[13]   M. J. Lovelady and J. D. Watts, "Closed loop feedback for continuous mode materials jetting," in *IEEE/CPMT International Electronic Manufacturing Technology Symposium*, Austin, Texas, 1999, pp. 189-195.

[14]   J. Mazumder, A. Schifferer, and J. Choi, "Direct materials deposition: designed macro and microstructure," *Materials Research Innovations,* vol. 3, pp. 118-131, 1999.

[15]   F. Pérès and D. Noyes, "Envisioning e-logistics developments: Making spare parts in situ and on demand state-of-the-art and guidelines for future developments," *Computers in Industry,* vol. 57, pp. 490-503, 2006.

[16]   L. Sun, K. J. Jakubenas, J. E. Crocker, S. Harrison, L. L. Shaw, and H. L. Marcus, "In situ thermocouples in macro-components fabricated using SALD and SALDVI techniques," *Materials and Manufacturing Processes,* vol. 13, pp. 909-919, 1998.

[17]   E. Whitney, "Advances in rapid prototyping and manufacturing using laser-based solid free-form fabrication," in *The Handbook of Advanced Materials*, Oak Ridge, TN: John Wiley & Sons, 2004, pp. 611-631.

[18]   S. Sampath, "Novel concepts in direct writing of electronics and sensors," *IEEE Sensors Journal,* vol. 4, 2004.

[19]   C. V. Zwirewich, B. Terriff, and N. L. Muller, "High-spatial-frequency (bone) algorithm improves quality of standard CT of the thorax," *American Journal of Roentgenology,* vol. 153, pp. 1169-1173, 1989.

[20]   M. P. Bodiford, S. D. Gilley, R. W. Howard, J. P. Kennedy, and J. A. Ray, "Are we there yet?… developing in situ fabrication and repair (ISFR) technologies to explore and live on the Moon and Mars," in *First Space Exploration Conference: Continuing the Voyage of Discovery*, Orlando, Florida, 2005, pp. 1-7.

[21]   E. Malone and H. Lipson, "Functional freeform fabrication for physical artificial life," in *Ninth International Conference on the Simulation and Synthesis of Living Systems*, Boston, Massachusetts, 2004, pp. 100-105.

APPENDIX A:

HYDROCOLLOID PRINTING – A NOVEL PLATFORM FOR CUSTOMIZED

FOOD PRODUCTION[*]

ABSTRACT

Solid Freeform Fabrication (SFF) of food has the potential to drastically impact both culinary professionals and laypeople; the technology will fundamentally change the ways we produce and experience food. Several imposing barriers to food-SFF have been overcome by recent open-source printing projects. Now, materials issues present the greatest challenge. While the culinary field of molecular gastronomy can solve many of these challenges, careful attention must be given to contain materials-set bloat. Using a novel combination of hydrocolloids (xanthium gum and gelatin) and flavor agents, texture and flavor can be independently tuned to produce printing materials that simulate a broad range of foods, with only a minimal number of materials. In addition to extensively exploring future applications of food-SFF, we also present a rigorous proof-of-concept investigation of hydrocolloids for food-SFF. A two-dimensional mouthfeel rating system was created (stiffness vs. granularity) and various hydrocolloid mixtures were characterized via an expert panel of taste testers.

INTRODUCTION

Few things are as natively intertwined with humanity as food, which is essential to biological and social life[1]. Not only does food support life and underpin social relations, but it also accounts for a substantial part of our economy. As of 2008,

---

[*] Daniel L. Cohen[1], Jeffrey I. Lipton[1], Meredith Cutler[2], Deborah Coulter[2], Anthony Vesco[2], Hod Lipson[1,3]; [1]Cornell University, Mechanical and Aerospace Engineering, Ithaca NY; [2]Cornell University, School of Hotel Administration, Ithaca NY; [3]Cornell University, Computing and Information Science, Ithaca NY.

Americans spent $1.02 trillion annually on food, i.e., 9.6% of the nation's combined disposable personal incomes[2]. Solid Freeform Fabrication (SFF) has the potential to leverage its core strengths (e.g., geometric complexity, automated fabrication) and make its mark on the culinary realm by transforming the way we produce and experience food. We foresee SFF extending new capabilities both to culinary professionals and to laymen, as well as having global social implications by directly extending Web 2.0 phenomena to food.

Technological innovations are necessary, however, before these visions can be realized. In addition to lowering barriers to SFF, such as cost of the machine, materials must be developed to feasibly enable a wide range of foods to be produced on SFF platforms. While many raw foods are natively printable, other foods can only be printed if novel materials are developed. Advancements in the field of molecular gastronomy will likely influence the development of these novel food-SFF materials, especially with respect to the use of hydrocolloids. Food-SFF material platforms must be developed in such a way, however, that enables the printing of a very wide range of foods without bloating the size of the required materials-set. A potential solution to the issue of materials-set bloat is the use of novel combinations of hydrocolloids and flavor additives; this platform delivers many degrees of freedom in texture and flavor, while comprising a minimal number of required materials.

In this paper, we conceptually explore the broader future implications of food-SFF, as well as present rigorous scientific experiments that tackle materials issues that are central to its feasibility.

BACKGROUND

There are several barriers that have been standing in the way of food-SFF. One of the most imposing barriers is that most SFF machines have very limited

material-sets. For example, machines typically only support a handful of materials and nearly none incorporate food-safe printing materials into their repertoire. Moreover, most machines exclusively use proprietary materials and tools, and therefore leave no room for experimentation with food-related printing materials. Thus, it remains that a materials-flexible, open-source printing platform is critical for enabling the growth of the food-SFF paradigm.

There are indeed several open-source printing projects that lend the necessary freedom for innovators to experiment with novel, non-proprietary printing materials. One such project is RepRap; however, this open-source printing platform does not offer the deposition tools required to print edible food[3]. CandyFab, is another open-source printing project. This platform uses a bed of sugar and a sintering tool to build 3D prototypes[4]. Even so, the primary use is not for producing edible food. Rather than being used for its potentially edible nature, sugar is mainly used because it is a cheap, available and safe printing material. Only one open-source printing platform offers a flexible enough materials-set to enable printing of a wide range of edible products, that is, the Fab@Home. The Fab@Home printing platform is not only open-source, but its syringe-based deposition tool allows for the printing of any material that can be loaded into a syringe[5]. This non-propriety, flexible-printing-material system overcomes some of the most imposing barriers to food-SFF.

Another barrier has traditionally been printing system cost. While large industrial enterprises may be able to afford $100,000+ SFF systems, many culinary community members and especially individual homeowners cannot get into the food-SFF game with such high equipment costs. In the last decade, we have seen SFF machine costs drop nearly an order of magnitude (with several open-source printers running under $1,500). It is only now, with the reduced SFF cost landscape, that food-SFF is feasible from a financial perspective.

To this point, the volume of work published on food printing has been rather limited. Daniel Periard *et al* investigated SFF of traditional food items that were printable in their raw form (e.g., chocolate, cake frosting). This food printing work was limited to those edible printing materials that were natively extrudable through a syringe and inherently held their shape under gravity[6]. As a result of relying upon unmodified foods, this work did not fully explore the potential of food printing that could be realized with the development of novel material-sets.

Now that the proprietary restrictions, materials-set inflexibilities and cost barriers have been lifted, the stage is set to explore food-SFF's full potential by inventing new food-related printing applications and by developing the necessary novel materials.

POTENTIAL IMPACT OF FOOD-SFF

Impact on Culinary Professionals – Overview

Food-SFF would benefit the professional culinary domain primarily in two respects: by lending new artistic capabilities to the fine dining domain, and also by extending mass-customization capabilities to the industrial culinary sector.

Impact on Culinary Professionals – Fine Dining

Fine dining chefs are continually developing new, innovative techniques and seeking the enabling technologies that will help them push the boundaries of culinary art. In particular, chefs pioneering the cooking style known as "molecular gastronomy" (i.e., the scientific study of physical and chemical processes related to cooking) are at the forefront of this expanding frontier. They innovate by harnessing non-traditional ingredients, such as hydrocolloids, and by employing new tools pulled straight from the scientific community; the result is "culinary magic" including

174

flavored gelatin spheres with liquid centers, sauce foams, hot liquid deserts with flash frozen shells, syringe-extrudable meats, and much more[7]. One of the most notable molecular gastronomists is Chef Ferran Adrià, whose restaurant in Spain, *elBulli*, is considered to be among the finest in the world; the restaurant receives about 2 million applications for a chance at grabbing one of only 8,000 annual slots[8]. Other notable molecular gastronomists include David Arnold and Nils Noren, of the French Culinary Institute in New York City[7].

These pioneers are driving a new trend, in which a growing number of chefs are recognizing the important role that science and technology play in the culinary arts, a notion highlighted by Adrià's closing of *elBulli* for 6 months each year to purely focus on R&D[8]. During these closings, Adrià searches the world for the newest enabling technologies that will allow him to push the limits of the culinary arts even further.

SFF promises to be the next important enabling technology in the fine dining realm. SFF delivers new possibilities by lending this faction of culinary artists one of SFF's core capabilities: fabrication of multi-material objects with high geometric complexity. SFF's culinary potential has already been recognized by one of the most prominent molecular gastronomists; in a 2008 interview with *Popular Science*, Chef David Arnold mentioned that he "particularly dreams of getting a deal on a 3D rapid prototyping machine"[7]. As the barriers fall (e.g., SFF machine prices have reduced nearly an order of magnitude in the last decade) and non-traditional ingredients gain credibility in the fine dining world (e.g., hydrocolloids), the question is not whether SFF will play an important role in the future of food, but rather, in what ways will it do so.

Examples of potential future applications include cakes with complex, embedded 3D letters, such that upon slicing the cake, a message is revealed. Or, even

a prime rib with a hidden message. Perhaps an on-demand, customizable menu in which the dish is prepared in any 3D shape that the diner desires: the diner can co-create with the culinary artist in real-time.

Impact on Culinary Professionals – Industrial Production

The second way in which SFF could benefit the professional culinary community is by enabling mass-customization in the industrial culinary sector. Today, industrial food producers rely heavily on high-throughput processes such as molding, extrusion and die-cutting[9]. These processes, however, are not amenable to mass-customization (i.e., the use of flexible manufacturing techniques to produce custom output in a low-unit-cost fashion). Molding, extrusion and die-cutting each require substantial custom-tooling, and consequently, producing custom output for low-quantity runs is simply unfeasible[10]. This is precisely where SFF's inherent strengths can be leveraged: producing food with *custom*, complex geometries while maintaining cost-effectiveness. The cost-effectiveness is enabled by the fact that SFF does not require custom-tooling or extensive manual labor.

One potential future application is *custom* production of edible giveaways, for example, as marketing collateral for small corporate events. Currently, the cost of custom tooling prohibits low-quantity *custom* production runs, but with a flexible culinary production platform like SFF, such production runs would be feasible.

Impact on Non-Professionals – Overview

Culinary professionals are more primed to adopt SFF than are homeowners, however, the implications for laypeople are even more profound. The effect on laypeople is essentially twofold: increasing productivity and injecting knowledge.

Impact on Non-Professionals – Productivity

Since the late 19th century, a number of machines have been introduced to the home that perform routine tasks more efficiently and ultimately offload work from individuals. Several examples include washing machines, dryers, dishwashers and vacuum cleaners. Perhaps the most profound domestic technology was the sewing machine. Although sewing machines were developed for factory use in the 1850's, it was not until the late 1870's that the devices entered homes ubiquitously. Prior to the sewing machine, an average middle-class woman would spend several days per month making and mending her family's clothing[11]. More specifically, it would take 14 hours to make a man's dress shirt and 10 hours to make a simple dress. With a sewing machine, dress shirts could be made in 1.25 hours and dresses in 1 hour. Women of the 1870's and 1880's used this saved time to branch out: taking in sewing work for extra money and becoming sales representatives for sewing machines. The reduction in housework ultimately transformed women's roles as household managers and contributed to women seeking employment outside of the home[11]. Domestic technologies have had a tremendous effect on society over the last 150 years by offloading housework, and in turn, creating capacity for people to extend themselves beyond the home in new ways. SFF has the potential to join this portfolio of important domestic technologies by *end-to-end* offloading of food preparation.

Currently, the average American spends more than 30 minutes per day preparing food, according to USDA economists[12]. This amount changes drastically depending on a number of factors, including: marital status, working status, gender and income level. Single, working people spend 15 – 35 minutes per day cooking, while married, non-working women spend an average of 70 – 85 minutes per day[12]. Clearly there is potential to offload culinary housework for people of all genders, marital statuses, working statuses and income levels. If food-SFF were brought to the

"set-and-forget" state, requiring minimal human labor, the average person could possibly realize time savings of 150+ hours per year (3.8 workweeks per year), with certain, large groups (e.g., married, non-working women) saving in excess of 500 hours per year (12.5 workweeks per year). Of course, operating the SFF system will still take some finite amount of time and, moreover, families will certainly choose to spend some of the mealtime either with a traditionally cooked meal or out-of-home dining. Regardless of how much time savings SFF could afford, and even whether it has potential adverse social effects, it is clear that food-SFF is something that warrants further contemplation and investigation.

Impact on Non-Professionals – Injecting Knowledge

The second way that food-SFF could impact laypeople is by abstracting culinary knowledge and injecting it directly into the home. The idea of abstracting knowledge is nothing new. When it comes to playing a popular song, amateur musicians do not have to learn how to play it from scratch. Rather, they obtain sheet music that prescribes the actions (e.g., valve, key or fret manipulations) necessary to reproduce the song. The composer's artistic skill and knowledge have been abstracted and captured in the sheet music, which somebody lacking the artistic skill and knowledge can use to reproduce the original work. Of course, the end-user (i.e., the musician) still needs a non-trivial skill set to properly interpret and execute the prescription (i.e., the sheet music).

Abstracting knowledge for the purpose of having less skilled practitioners reproduce the original work is also found in the realm of culinary arts. When chefs create new dishes and then write recipes, they are effectively abstracting their knowledge and distilling it into a prescription for others to reproduce their work.

Nevertheless, just like the skills a musician needs to effectively play a song from sheet music, a recipe follower still needs non-trivial skills to execute a recipe.

It is not only in the abstraction of knowledge, but also in the execution of the prescription that SFF could have tremendous impact. Just as MIDI software can offload musical skill by taking in digital sheet music and directly creating sound, the SFF system could directly inject the skills necessary to follow a recipe end-to-end. Laypeople don't have to know the first thing about musical notation, valve/key/fret fingering, or tonal theory to be able to utilize a stereo system to deliver a distilled version of a live musical performance directly into their home. Likewise, a layperson would not necessarily need to possess even basic culinary skills to employ an SFF system to create geometrically complex, multi-material food items.

Culinary knowledge and artistic skill of world renowned chefs can be abstracted to a 3D fabrication file and then used by laypeople to reproduce famous chefs' work in the home. Also, expert knowledge of the world's leading nutritionists can be abstracted and encoded in 3D fabrication files to help laypeople eat more healthily, without necessarily having to learn healthy cooking techniques or even understand nutritional principles such as caloric intake and protein balance. SFF systems could even go one step further, and deliver customized solutions (SFF's core strength) to each user that incorporate the individualized nature of nutritional needs. For example, a layperson may soon be able to upload a report of their daily activity from a pedometer and digital food log, and the SFF system could use expert knowledge to print them a meal that fulfills their particular nutritional needs for the day. While experts can currently offer advice on how to balance a nutritional program, their influence falls short of delivering the end-to-end solution that only SFF system can provide: from personalized design through fabrication.

179

Food-SFF and Web 2.0

Whether professionals use SFF for cutting-edge capability or laypeople use it to borrow more basic skills, the abstraction and subsequent direct-execution of culinary knowledge has profound social effects. Once culinary knowledge can be abstracted, it can also be easily shared. It wasn't until music and photographs were represented in digital abstracts (i.e., MP3s and JPEGs) that sharing became easy enough for entire web communities to develop around them.

Some online Web 2.0 social networks have grown to more than 200,000,000 community members[13]. In particular, networks established around sharing and communally experiencing photographs (e.g., Flickr) and music (e.g., Last.fm) boast tens of millions of users, each. Now that SFF will potentially enable the feasible sharing of food (via trading 3D fabrication files), we can start thinking of what the future could look like. After all, few things are more essential to social relationships than food. Through food, people share tastes, ideas, values and generosity[1]. Imagine amateurs and professionals alike, sharing their latest ideas and helping others solve culinary challenges. Not only would new types of social bonds form across the world, but people will harness principles of "wikinomics" and begin to "mass-collaborate" seamlessly from all corners of the globe[14]. A *truly* global cuisine could emerge. Through mass-collaboration, people could even attempt to solve major challenges such as creating fundamentally new types of healthful foods.

Furthermore, we could see democratization of innovation and a major revision of the current business models of the culinary profession. No longer would only those with access to distribution channels be privileged with sharing their food with the world, but rather, any amateur or professional chef could see their work gain prominence as long as their ideas have merit. A more democratic business landscape will emerge, and the lines between amateur and professional will be blurred.

MATERIALS CHALLENGES

In order to unlock food-SFF's potential, we need to think about the specific technical challenges standing in the way. As mentioned earlier, SFF systems' materials inflexibility, prohibitive cost and proprietary restrictions were barriers that have largely been overcome by recent open-source printing efforts, such as Fab@Home. Now, the printing materials themselves are the bottleneck. Some foods, such as cake frosting, processed cheese, hummus and chocolate are natively printable; they are extrudable through a syringe tip and hold their shape under gravity[6]. Other foods, such as fruits, vegetables and meats are not natively printable. In order to be able to print these important food-types, we would have to undertake substantial reformulation efforts. These types of challenges have already been tackled by molecular gastronomists. In this avant-garde culinary field, it is becoming typical to make solids (e.g., meats) extrudable by adding hydrocolloids[7]. With the appropriate molecular gastronomic tricks, we can realize both printable solid foods and printable semi-solid liquids; the possibilities are nearly limitless.

However, as we attempt to target foods one-by-one in an effort to make them printable, the number of custom, one-off material combinations greatly expands. This leads to the challenge of containing the bloat of the materials-set. The question becomes: how do we enable the printing of a wide range of foods with only a limited, fundamental set of materials?

FLEXIBLE MATERIALS PLATFORM –
A MOLECULAR GASTRONOMIC APPROACH

Overview

One potential solution to containing materials-set bloat is to use a small group of ingredients to create a platform with many degrees of freedom in terms of texture

and flavor. By fine tuning hydrocolloids' concentrations, and focusing on the ratios between combinations of different hydrocolloids, a very wide range of textures (i.e., mouthfeels) can be achieved. Furthermore, given the generally neutral flavors of hydrocolloids, the flavor can be independently tuned by using concentrated flavoring additives. By independently controlling these two parameters, texture and flavor, we suggest that a wide range of food experiences can be simulated.

Appendix Table A.1. Mouthfeel matrix with common foods placed as reference items.

Chocolate				Fried fish	Carrots	Biscotti
	Mushroom			Apple	Cooked chicken	Saltine
	Banana	Cooked spaghetti	Fresh mozzarella	Tomato		Hard-boiled egg yolk
Creamy peanut butter	Marshmallow fluff	Meringue				Ground beef
Jell-O						
Gravy	Mashed potato	Cake icing			Refried beans	
Self-supporting gel				White bread	Polenta	
Non-self-supporting gel	Pudding	Cake batter	Raspberry coulis	Apple sauce	Risotto	
Milk	Ice cream			Sorbet		Coffee grinds

(Vertical axis: Most Firm → Weakest. Horizontal axis: Smoothest → Most Granular.)

The two hydrocolloids focused on in this paper are xanthan gum and gelatin. Various combinations of the two were tested for mouthfeel. In order to rigorously describe the mouthfeel of each resultant material, we devised a rating system in which the material was rated along two orthogonal axes: 1) weak to firm, and 2) smooth to

granular. This "mouthfeel matrix" was developed in cooperation with expert chefs from the Cornell University School of Hotel Administration (Appendix Table A.1).

There are 7 discrete buckets on the smooth-to-granular axis and 9 buckets on the weak-to-firm axis. Common foods were placed within this framework for the taste testers' reference, and the testers were asked to place a particular hydrocolloid concoction within the matrix relative to these references.

Methods – Materials Preparation

Xanthan gum and gelatin were prepared in water at various concentrations, ranging from 0.5% gelatin in water (by weight) to 4% gelatin in water, and from 2% xanthan in water to 16% xanthan in water. After preparation, the hydrocolloid concoctions were loaded into 10 mL syringes (Appendix Figure A.1).

Appendix Figure A.1. Various hydrocolloid formulations loaded into 10 mL Luer-Lok syringes.

To test the flexibility afforded by flavoring additives, various food grade flavor concentrates were infused with the hydrocolloids, including raspberry, strawberry, banana and chocolate.

Methods – Printing

After the materials were loaded into 10 mL Luer-Lok syringes, the syringes were loaded into the displacement deposition tool of the Fab@Home printer (Appendix Figure A.2). Using the custom, open-source Fab@Home control software, 3 centimeter cubes were printed.

We printed each sample to properly account for any effect the extrusion process had on the texture. There is gel-ripping upon extrusion that creates a specific microstructure and texture.

a)   b)
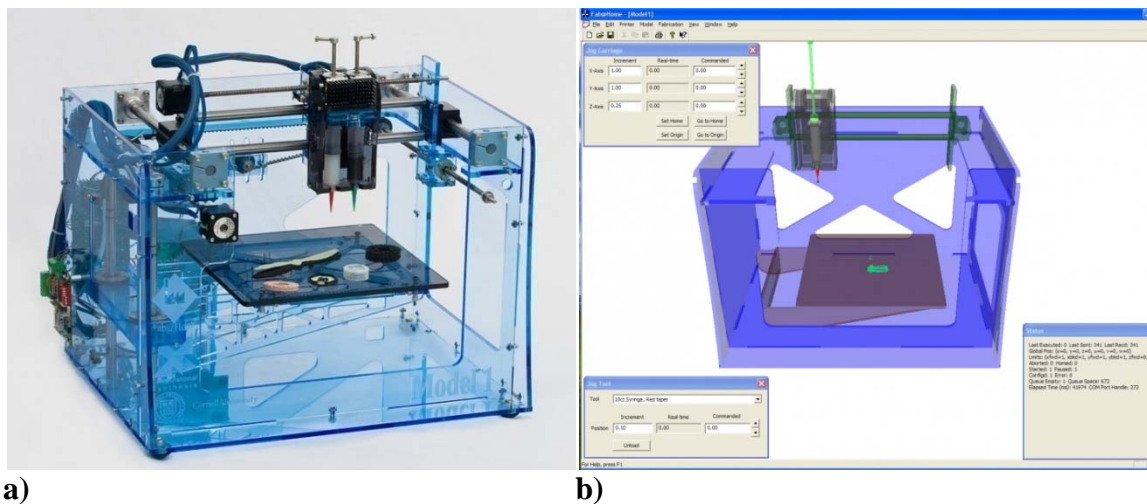
Appendix Figure A.2. Fab@Home printing platform. (a) Fab@Home hardware comprising 3-axis gantry motion system and deposition tool. (b) Screenshot of control software.

Methods – Materials Evaluation

Various combinations of xanthan gum and gelatin were prepared and presented to a panel of seven taste testers, including two professional culinary instructors. Each rated the hydrocolloids within the "mouthfeel matrix" by comparing the texture to the matrix's reference foods.

Results – Platform Flexibility Described Through Mouthfeel Matrix

The mouthfeels for xanthan gum and gelatin hydrocolloid concoctions were individually tested and pinned on the mouthfeel matrix (Appendix Table A.2).

Appendix Table A.2. Mouthfeel matrix of hydrocolloid mixture showing the formulations in the appropriate locations relative to common foods (see Table A.1 for more detail) with the closest common foods are listed below the hydrocolloid concentrations in bold.

(Smoothest)						(Most Granular)
Most Firm 4% gelatin *CLOSE TO* **CHOCOLATE/ MUSHROOM**						
		16% xanthan **COOKED SPAGHETTI**				
				1% gelatin 8% xanthan *CLOSE TO* **TOMATO**		
2% gelatin **JELL-O**		2% gelatin 8% xanthan *CLOSE TO* **CAKE ICING/ MERINGUE**	0.5% gelatin 8% xanthan *CLOSE TO* **CAKE ICING/ MERINGUE**			
	4% xanthan **MASHED POTATO**					
1% gelatin **SELF-SUPPORTING LOOSE GEL**						
2% xanthan **NON-SELF-SUPPORTING LOOSE GEL**				0.5% gelatin 4% xanthan **APPLE SAUCE**	1% gelatin 4% xanthan **RISOTTO**	
Weakest 0.5% gelatin **MILK**						

Smoothest — Most Granular

Mouthfeels were achieved that simulated a broad range of common foods. These simulated mouthfeels ranged from milk to mushroom to tomato to risotto. The hydrocolloids spanned a range from liquids to solid vegetables. The mouthfeels followed a rather identifiable pattern. Pure xanthan and gelatin tracks directly up the weak to firm axis, but does not shift in granularity. However, as xanthan and gelatin are combined, the resultant hydrocolloids begin to possess some amount of granularity. Generally, the higher the concentration of xanthan and gelatin, the firmer and more granular the gels become.

The printability of the hydrocolloids reached a limit as the stiffness and granularity of the resultant materials prevented reliable extrusion of the materials through a 3 mm syringe orifice.

DISCUSSION AND CONCLUSIONS

Using only two ingredients, xanthan and gelatin, a very broad range of mouthfeels can be simulated. This type of approach addresses the issue of materials-set bloat that would be faced as end-users attempt to feasibly implement SFF for culinary applications with a small, practical materials-set.

While the work herein serves as a proof-of-concept, further materials development is required to progress food-SFF. Not only does the mouthfeel range need to be expanded, but the flavors also need to be refined by tuning the flavor additives. To truly demonstrate the capability of hydrocolloid-based printing, ideally a double-blind tasting should be performed and it would be seen whether the taster can distinguish between the natural food and the hydrocolloid version. It should be noted, however, that even if subtle differences are perceptible, it is not necessary in all cases to perfectly *reproduce* the original food; there is still great value in *simulating* the original food.

Regardless of whether a hydrocolloid approach is taken to food-SFF, or some other molecular gastronomic platform is employed, the potential future applications of food-SFF remain the same. From culinary professionals to laypeople, individuals from all walks of life will be drastically affected by food-SFF. Artistic boundaries will be pushed in fine dining and industrial producers will explore mass-customization. Laypeople will have housework time reduced and benefit from direct culinary skill injections. Web 2.0 will tackle the next great frontier as people from all over the world experience food in new ways, while forming social bonds and mass-collaborating.

Now that major barriers have been broken, such as high printer cost and proprietary restrictions, the stage is finally set for tremendous growth of food-SFF. Few things are more central to humanity than food, and therefore is should come as no surprise when food-SFF gains prominence as one of the 21st century's important domestic technologies.

REFERENCES

[1]   C. Counihan, *The anthropology of food and body: gender, meaning, and power*. New York: Routledge, 1999.

[2]   USDA Economic Research Service, "Economic Research Service Database (Table 7)," Retrieved August 12, 2009, from United States Department of Agriculture, http://www.ers.usda.gov/briefing/CPIFoodandExpenditures/Data/table7.htm, 2009.

[3]   C. Biever, "3D printer to churn out copies of itself," *New Scientist Magazine*, March 18, 2005.

[4]   M. Irwin, "Caramel-pumping 3D fabricator has couple on a sugar high," *Wired Magazine*, July 24, 2007.

[5]   E. Malone and H. Lipson, "Fab@Home: the personal desktop fabricator kit," *Rapid Prototyping Journal,* vol. 13, pp. 245-255, 2007.

[6]   D. Periard, N. Schaal, M. Schaal, E. Malone, and H. Lipson, "Printing Food," *Eighteenth Solid Freeform Fabrication Symposium*, Austin, Texas, 2007, pp. 564-574.

[7]   T. Allen, "Doctor delicious," *Popular Science*, July 28, 2008.

[8]   E. Callaway, "Science is vital ingredient at world's best restaurant," *New Scientist Magazine*, March 20, 2009.

[9]   J. S. Smith and Y. H. Hui, *Food processing: principles and applications*. Oxford: Blackwell Publishing, 2004.

[10]   B. J. Pine and S. Davis, *Mass customization: The new frontier in business competition*. Boston: Harvard Business School Press, 1999.

[11]   Museum of American Heritage, "Stitches in Time: 100 Years of Machines and Sewing," Retrieved July 5, 2009, from Museum of American Heritage Website, http://www.moah.org/exhibits/archives/stitches/impact.html, 2005.

[12]   L. Mancino and C. Newman, "Who's cooking? Time spent preparing food by gender, income and household composition," in *2006 Annual Meeting of the American Agricultural Economics Association*, Long Beach, California, 2006.

[13]   J. Powell, *33 Million People in the Room*. Upper Saddle River, NJ: Pearson Education, 2009.

[14]   D. Tapscott and A. D. Williams, *Wikinomics: How mass collaboration changes everything*. New York: Penguin Group, 2008.

APPENDIX B:

LIST OF PUBLICATIONS

JOURNAL ARTICLES

1. **D. L. Cohen** and H. Lipson, "Geometric feedback control of discrete-deposition SFF systems," *Rapid Prototyping Journal,* accepted. (CHAPTER 3)

2. J. J. Ballyns, **D. L. Cohen**, E. Malone, S. A. Maher, H. G. Potter, T. M. Wright, H. Lipson, and L. J. Bonassar, "An optical method for evaluation of geometric fidelity for anatomically shaped tissue engineered constructs," *Tissue Engineering Part C: Methods,* accepted.

3. **D. L. Cohen**, E. Malone, H. Lipson, and L. J. Bonassar, "Direct freeform fabrication of seeded hydrogels in arbitrary geometries," *Tissue Engineering,* vol. 12, pp. 1325-1335, 2006. (CHAPTER 1)

4. E. Malone, K. Rasa, **D. L. Cohen**, T. Issacson, H. Lashley, and H. Lipson, "Freeform fabrication of zinc-air batteries and electromechanical assemblies," *Rapid Prototyping Journal,* vol. 10, pp. 58-69, 2004.

JOURNAL MANUSCRIPTS "IN REVIEW" OR "IN PREPARATION"

5. **D.L. Cohen**, W. Lo, A. Tsavaris, D. Peng, H. Lipson, and L.J. Bonassar, "Increased mixing improves hydrogel homogeneity and quality of 3D printed constructs." (CHAPTER 2)

6. **D.L. Cohen**, J.I. Lipton, L.J. Bonassar, and Hod Lipson, "Solid freeform fabrication for *in situ* repair of chondral and osteochondral defects." (CHAPTER 4)

7. **D. L. Cohen**, J.I. Lipton, and Hod Lipson, "Solid freeform fabrication for *in situ* repair and adaptation of robots." (CHAPTER 5)

8. **D.L. Cohen**, J.I. Lipton, K.W. Gluck, J. Granstein, R. Masanoff, E. Ellis, and H. Lipson, "Information platform for mass-collaborative, ubiquitous 3D printing."

9. U. Krotscheck, **D.L. Cohen**, and M. Thompson, "Utilization of 3-dimensional rapid prototyping for correction of angular limb deformities in dogs."

PATENTS

10. H. Lipson, L. J. Bonassar, **D. L. Cohen**, and E. Malone, inventors; Cornell Research Foundation, Inc., assignee. "Modular fabrication systems and methods." United States of America Patent No. US 7,625,198. 2009.

11. T. A. Staab, **D. L. Cohen**, and S. Feller, inventors; Los Alamos National Security, LLC, assignee. "Apparatus and method for mapping an area of interest." United States of America Patent No. 7,627,448. 2009.

12. L. J. Bonassar, H. Lipson, **D. L. Cohen**, and E. Malone, inventors; Cornell Research Foundation, Inc., assignee. "Modular fabrication systems and methods." United States of America Patent Application No. 11/201,057. 2005.

REFEREED CONFERENCE PAPERS

13. **D. L. Cohen**, J. I. Lipton, M. Cutler, D. Coulter, A. Vesco, and H. Lipson, "Hydrocolloid printing: A novel platform for customized food production," *Twentieth Annual International Solid Freeform Fabrication Symposium*, Austin, Texas, 2009, pp. 807-818. (APPENDIX A)

14. J. I. Lipton, **D. L. Cohen**, M. Heinz, M. Lobovsky, W. Parad, G. Bernstein, T. Li, J. Quartiere, K. Washington, A.-A. Umaur, R. Masanoff, J. Granstein, J. Whitney, and H. Lipson, "Fab@Home Model 2: Towards ubiquitous personal fabrication devices," *Twentieth Annual International Solid Freeform Fabrication Symposium*, Austin, Texas, 2009, pp. 70-81.

15. J. I. Lipton, **D. L. Cohen**, and H. Lipson, "Brick printing: Freeform fabrication of modular architectural elements with embedded systems," *Twentieth Annual International Solid Freeform Fabrication Symposium*, Austin, Texas, 2009, pp. 711-723.

16. A. Mookerjee, **D. L. Cohen**, D. H. Peng, L. J. Bonassar, and H. Lipson, "A study of variable stiffness alginate printing for medical applications," *Twentieth Annual International Solid Freeform Fabrication Symposium*, Austin, Texas, 2009, pp. 584-594.

17. **D. L. Cohen**, A. M. Tsavaris, W. M. Lo, L. J. Bonassar, and H. Lipson, "Improved quality of 3D-printed tissue constructs through enhanced mixing of algiante hydrogels," *Nineteenth Annual International Solid Freeform Fabrication Symposium*, Austin, Texas, 2008, pp. 676-685.

18. **D. L. Cohen**, E. Malone, H. Lipson, and L. J. Bonassar, "Direct freeform fabrication of spatially heterogeneous living cell-impregnated implants," *Fifteenth Solid Freeform Fabrication Symposium*, Austin, Texas, 2004, pp. 720-731.

19. E. Malone, K. Rasa, **D. L. Cohen**, T. Issacson, H. Lashley, and H. Lipson, "Freeform fabrication of 3D zinc-air batteries and functional electromechanical assemblies," *Fourteenth Solid Freeform Fabrication Symposium*, Austin, Texas, 2003, pp. 363-374.

REFEREED CONFERENCE ABSTRACTS AND POSTERS

20. J. J. Ballyns, **D. L. Cohen**, E. Malone, S. A. Maher, H. Potter, T. M. Wright, H. Lipson, and L. J. Bonassar, "Evaluation of geometric fidelity for anatomically shaped tissue engineered constructs," in *55th Annual Meeting of the Orthopaedic Research Society*, Las Vegas, Nevada, 2009.

21. **D. L. Cohen**, W. M. Lo, A. M. Tsavaris, L. J. Bonassar, and H. Lipson, "Improved quality of 3D-printed tissue engineering constructs through

enhanced mixing," in *55th Annual Meeting of the Orthopaedic Research Society*, Las Vegas, Nevada, 2009.

22. J. J. Ballyns, **D. L. Cohen**, E. Malone, H. Lipson, and L. J. Bonassar, "Evaluation of geometric fidelity for anatomically shaped tissue engineered constructs," in *2008 BMES Annual Fall Meeting*, St. Louis, Missouri, 2008.

23. **D. L. Cohen**, W. M. Lo, A. M. Tsavaris, L. J. Bonassar, and H. Lipson, "Improved quality of 3D-printed tissue constructs through enhanced mixing of alginate hydrogels," in *TERMIS North American 2008 Annual Conference & Exposition*, San Diego, California, 2008.

24. C. Blackhart, T. Staab, **D. L. Cohen**, and S. Feller, "Automation of forensics sample collection using real-time 3-D laser tracking and playback system," in *LabAutomation 2007*, Palm Springs, California, 2007.

25. **D. L. Cohen**, J. J. Ballyns, E. Malone, H. Potter, S. A. Maher, T. M. Wright, H. Lipson, and L. J. Bonassar, "Geometric fidelity of SFF-based methods for tissue engineering of anatomically shaped constructs," in *2006 BMES Annual Fall Meeting*, Chicago, Illinois, 2006.

26. **D. L. Cohen**, H. Lipson, and L. J. Bonassar, "Freeform fabrication of living tissue constructs using alginate hydrogel," in *2005 BMES Annual Fall Meeting*, Baltimore, Maryland, 2005.

27. **D. L. Cohen**, S. A. Maher, J. Rawlinson, H. Lipson, and L. J. Bonassar, "Direct freeform fabrication of living cell-seeded alginate hydrogel implants in anatomical shapes," in *51st Annual Meeting of the Orthopaedic Research Society*, Washington, D.C., 2005.

28. **D. L. Cohen**, E. Malone, L. J. Bonassar, and H. Lipson, "Direct freeform fabrication technique for bio-manufacturing of pre-seeded, spatially heterogeneous, anatomically shaped alginate hydrogel implants," in *2005 International Mechanical Engineering Congress and Exposition*, Orlando, Florida, 2005.

29. **D. L. Cohen**, L. J. Bonassar, and H. Lipson, "3-D printing of spatially heterogeneous pre-seeded living-cell implants using alginate hydrogel," in *2004 BMES Annual Fall Meeting*, Philadelphia, Pennsylvania, 2004.

APPENDIX C:

CONTRIBUTIONS

CONTRIBUTIONS OF THIS DISSERTATION

1.   Developed novel alginate hydrogel tissue printing material (Chapter 1). Validated geometric fidelity, cell viability, and biological function of constructs printed with this material. At the time this work was conducted, it was one of the earliest tissue printing techniques. It was the only additive manufacturing techniques capable of producing geometrically complex tissue engineering constructs with multi-axial spatial heterogeneities. Compared to existing techniques, it had a high cell viability and elastic modulus. This material platform was, and still is, one of the only approaches that is amenable to *in situ* fabrication, a topic explored in later work. The material platform's unique compatibility with *in situ* AM is related to the fact that the material's phase change is initiated chemically prior to deposition. One patent was awarded related to the modular substrate design, and another is pending related to the material formulation.

2.   Discovered new insights into the effects of mixing on alginate hydrogel-based tissue engineering techniques (Chapter 2). Found optimal mixing quantity to be more than 20 times higher than previously established protocol. Quantified the effect of mixing on alginate homogeneity and consequently enabled significant improvement of geometric fidelity of printed constructs. Also proposed the first quantitative methodology for characterizing the homogeneity of printing inks, which is a critical process variable for achievement of adequate geometric fidelity.

3.   Conceptualized and tested first geometric feedback control scheme (Greedy Geometric Feedback) for additive manufacturing that monitored and manipulated overall part geometry (Chapter 3). This approach enables handling of more extensive and higher level process uncertainties than other techniques. Very few existing techniques used geometric feedback of any kind. The few existing geometric feedback techniques all performed feedback on low-level process variables, not on the whole-part level. Consequently, the technique proposed herein is more generalized and capable of handling higher-level error types. This approach also used a novel greedy algorithmic approach to conserve system resources and minimize geometry scanning time.

4.   Developed first technique for generalized *in situ* additive manufacturing (Chapters 4 and 5) and demonstrated first ever *generalized in situ* AM prints. In prior examples of *in situ* printing, substrate-geometry was manually hard-coded *a priori*. The approach presented herein utilized a novel AM-path planning approach (Differed-Based Planning) to ascertain part-shape information, and physically repair or adapt a pre-existing part without *a priori* knowledge of the substrate geometry.

5.   Demonstrated first case of *in situ* repair of bone and cartilage defects using tissue engineering inks. This work has potential implications for future clinical treatment of orthopaedic injuries, and also demonstrates the strengths of the alginate material platform related to *in situ* compatibility. Also developed geometric fidelity benchmarking standards based upon prior clinical studies of acceptable surgical tolerances.

6.   Demonstrated first case of *in situ* repair and adaptation of a 4-legged robot. Prior advances had enabled robots to autonomously design and fabricate themselves. This work closes the autonomous robotic "lifecycle" by adding the abilities to repair and adapt themselves. This work has future implications for self-sustaining robot ecologies, but also has practical near-term uses for *in situ* repair of complex machinery.

7.   Developed a novel printing material set for additive manufacturing of food (Appendix A). While there had been a few prior efforts that investigated food printing, the material platform we proposed was one of the first that explored creating wide ranges of mouthfeels with a minimal set of materials. Minimization of material set bloat is essential if the technology is to be adopted in everyday home usage.

CONTRIBUTIONS OF OTHERS TOWARD THIS WORK

1.   Chapter 1 – "Tissue Printing"

   a. Collaborated with Evan Malone on execution of prints using custom additive manufacturing system he had previously developed.

   b. Provided ovine meniscus CT images by Suzanne Maher.

2.   Chapter 2 – "Increased Mixing Improves Hydrogel Homogeneity and Quality of 3D Printed Constructs"

   a. Collaborated with Winifred Lo and Andrew Tsavaris on collection and analysis, of mechanical noise and viability data.

   b. Collaborated with David Peng on collection and analysis of elastic modulus data.

3.   Chapter 3 – "Geometric Feedback Control of Discrete-Deposition SFF Systems"

   a. Utilized gantry robot system that Evan Malone had previously developed while he was a member of the research group.

4.   Chapter 4 – "Additive Manufacturing for *In Situ* Repair of Osteochondral Defects"

   a. Collaborated with Ursula Krotscheck on creation of defects in femoral printing substrate.

   b. Collaborated with Meg Thompson on CT imaging of femoral substrate.

c. Collaborated with Jeff Lipton on formulation of DBM printing material and on execution of prints.

5.   Chapter 5 – "Additive Manufacturing for *In Situ* Repair and Adaptation of Robots"

a. Collaborated with Jeff Lipton on image registration and on execution of prints.

6.   Appendix A – "Hydrocolloid Printing"

a. Collaborated with Meredith Cutler, Deborah Coulter, and Jeff Lipton on formulation of hydrocolloid printing inks.

b. Collaborated with Anthony Vesco, Meredith Cutler, Deborah Coulter, and Jeff Lipton on design of "mouthfeel matrix."

c. Collaborated with Jeff Lipton on execution of food prints.